

Particulate fouling of dry and liquid coated surfaces

Citation for published version (APA):

Sathyanarayanan Subbarao, K. K. (2012). *Particulate fouling of dry and liquid coated surfaces*. [Phd Thesis 1 (Research TU/e / Graduation TU/e), Mechanical Engineering]. Technische Universiteit Eindhoven.
<https://doi.org/10.6100/IR724551>

DOI:

[10.6100/IR724551](https://doi.org/10.6100/IR724551)

Document status and date:

Published: 01/01/2012

Document Version:

Publisher's PDF, also known as Version of Record (includes final page, issue and volume numbers)

Please check the document version of this publication:

- A submitted manuscript is the version of the article upon submission and before peer-review. There can be important differences between the submitted version and the official published version of record. People interested in the research are advised to contact the author for the final version of the publication, or visit the DOI to the publisher's website.
- The final author version and the galley proof are versions of the publication after peer review.
- The final published version features the final layout of the paper including the volume, issue and page numbers.

[Link to publication](#)

General rights

Copyright and moral rights for the publications made accessible in the public portal are retained by the authors and/or other copyright owners and it is a condition of accessing publications that users recognise and abide by the legal requirements associated with these rights.

- Users may download and print one copy of any publication from the public portal for the purpose of private study or research.
- You may not further distribute the material or use it for any profit-making activity or commercial gain
- You may freely distribute the URL identifying the publication in the public portal.

If the publication is distributed under the terms of Article 25fa of the Dutch Copyright Act, indicated by the "Taverne" license above, please follow below link for the End User Agreement:

www.tue.nl/taverne

Take down policy

If you believe that this document breaches copyright please contact us at:

openaccess@tue.nl

providing details and we will investigate your claim.

Particulate Fouling of Dry and Liquid Coated Surfaces

PROEFSCHRIFT

ter verkrijging van de graad van doctor aan de Technische Universiteit Eindhoven, op gezag van de rector magnificus, prof.dr.ir. C.J. van Duijn, voor een commissie aangewezen door het College voor Promoties in het openbaar te verdedigen op donderdag 16 februari 2012 om 16.00 uur

door

Kiran Kumar Sathyanarayanarao Subbarao

geboren te Bangalore, Karnataka, India

Dit proefschrift is goedgekeurd door de promotor:

prof.dr.ir. A.A. van Steenhoven

Copromotor:

dr. ir. C.C.M. Rindt

Het project is uitgevoerd met subsidie van het Ministerie van Economische Zaken, Landbouw en Innovatie, regeling EOS: Lange Termijn uitgevoerd door Agentschap NL

Copyright © 2011 by K. K. Sathyanarayanan Subbarao

All rights reserved. No part of this publication may be reproduced, stored in a retrieval system, or transmitted, in any form, or by any means, electronic, mechanical, photocopying, recording, or otherwise, without the prior permission of the author.

Printed by Proefschriftmaken.nl.

A catalogue record is available from the Eindhoven University of Technology Library

ISBN: 978-90-386-3088-5

Contents

1	Introduction	1
1.1	Fouling and slagging in heat transfer equipment	1
1.2	Fouling layer growth and morphology	2
1.3	Modeling slagging and fouling	3
1.4	Objective and outline of the thesis	9
2	Literature review of particle deposition models	11
2.1	Critical Stokes number for inertial impaction	11
2.2	Approaches to evaluate sticking probability	13
2.2.1	Melt phase approach	13
2.2.2	Critical viscosity approach	14
2.2.3	Critical velocity approach	16
2.2.4	Applicability and limitations of the models	17
2.3	Particle impaction over a dry surface	18
2.4	Particle impaction over a liquid coated surface	20
2.4.1	Model 1	21
2.4.2	Model 2	24
2.4.3	Comparison of models	28
2.4.4	Modifications to model 2	30
2.5	Conclusions	32
3	Experiments on particle impaction over liquid coated substrates	35
3.1	Experimental methods	35
3.2	Physical description of the wet impaction process	39
3.3	Comparison of models with experimental data	41
3.4	Energy balance for impaction involving elastic-plastic deformations	47
3.4.1	Energy dissipation in plastic deformation	48
3.4.2	Wet elastic collisions	49
3.4.3	Elastic-plastic collisions	51
3.4.4	Comparison of elastic and elastic-plastic collisions	53
3.5	Conclusions	55

4	Controlled fouling experimental facility	57
4.1	Background	57
4.2	Design considerations	58
4.3	Experimental facility design	60
4.4	Instrumentation	65
4.5	Measurement technique for particle deposition	65
4.6	Operation and testing	68
4.7	Experimental procedure	70
5	Controlled fouling experiments	75
5.1	Background	75
5.2	Initiation and layer growth dynamics	78
5.3	Influence of flow parameters	81
5.3.1	Effect of gas phase velocity	81
5.3.2	Effect of particle concentration	83
5.3.3	Effect of gas phase temperature	83
5.4	Effect of particle type and size distribution	85
5.5	Influence of target geometry and orientation	87
5.5.1	Effect of tube size	87
5.6	Effect of tube shape and orientation to the flow	89
5.6.1	Three tubes in a row	91
5.7	Effect of liquid layer	92
5.8	Conclusions	96
6	Numerical simulations	99
6.1	Flow field and particle trajectory calculations	99
6.1.1	Flow equations	100
6.1.2	Particle dispersion and transport in a turbulent flow field	101
6.1.3	Validation of flow model	103
6.1.4	Validation of particle transport model	105
6.2	Removal model for dry particulate fouling	106
6.3	Particle deposition based on Roger and Reed model	110
6.3.1	Influence of gas phase velocity	112
6.3.2	Dry deposition over a square cylinder	115
6.3.3	Tubes in a row	116
6.3.4	Evolution of fouling layer	119
6.3.5	Particle deposition on a liquid layer	121
6.4	Conclusions	123
7	Conclusions and recommendations for future work	127
	Bibliography	131

A Gasification and gas phase contaminants in biomass gasifiers	137
A.1 Biomass gasification	137
A.2 Gas phase contaminants	138
B Cyclone design and pressure drop in the system	141
B.1 Cyclone and its design	141
B.2 Pressure drop due to different parts of the system	145
B.2.1 Pressure drop for flow through duct	146
B.2.2 Pressure drop for bends	146
B.2.3 Pressure drop across heat exchanger/test section	147
B.2.4 Pressure drop across heater	147
Summary	149
Samenvatting	151
Curriculum Vitae	153
Acknowledgements	155

Introduction

1.1 Fouling and slagging in heat transfer equipment

Particle deposition on a surface can be either desirable or undesirable depending on the specific application. In either case, understanding how particles interact with each other or with a surface is of utmost importance. In most of the natural and industrial applications, the process of unwanted particle deposition is termed as fouling. Fouling can be of different types, like: biological fouling, precipitation fouling, particulate fouling, chemical reaction fouling and sedimentation fouling. Non-particulate contaminants like dissolved carbonates, bacteria and salts may be controlled by adding chemicals and bactericides. However, particles are very difficult to prevent from forming or entering into the system and this is a major concern related to fouling of heat exchanger surfaces in process industries and power generation units. The thermal conductivity of the fouling layer is very low and the formation of deposits on the heat transfer surfaces reduces thermal and hydrodynamic performance over time. In power generation units involving combustion, slagging is defined as the deposition of fly ash on heat transfer and refractory surfaces which are primarily subjected to radiant heat transfer [16]. Fouling and slagging leads to extra capital expenditure, increased fuel costs, production loss and maintenance problems. Due to the enormous costs associated with fouling, many studies have been conducted to investigate the physics involved in fouling and slagging. Owing to its complexity, fouling still persists to be a troublesome aspect and has been an interesting subject of study for many researchers.

1.2 Fouling layer growth and morphology

Deposition and retention of gas contaminants occur on almost all major gas-side equipments. This is especially a major cause of concern in many coal and biomass based systems. A brief overview of biomass gasification and the gas phase contaminants generated during gasification process is discussed in appendix A. The process of contaminant deposition occurs over a wide range of temperatures and in different regions of a plant. Slagging, which refers to the deposition in high temperature regions is affected by different parameters as compared to that of fouling deposits found in the gas cooling sections like reheater or economizer. Based on the location, the fundamental mechanisms governing particle deposition and removal differ drastically. Due to the complexities involved with thermal conversion, chemical reaction, fluid-particle interaction, sintering etc., describing fouling and slagging has been a difficult task.

Experiments and analysis of the structure of the deposited layers provide insight into the deposit forming dynamics and have been studied by various researchers in the past. Early experiments were carried out mostly as on-site measurements by inserting deposition probes and by taking temperature measurements. These experiments provided important information which were used to classify different types of fouling and to develop fouling indices. Later experiments were mostly carried out in pilot-plants and the analysis of fouling was done using advanced techniques like X-ray diffraction, electron probe X-ray micro analysis and Scanning Electron Microscopy (SEM) [25, 62]. The measure of the resistance offered by the fouling layer to the heat transfer is aptly termed as fouling resistance and is expressed as the ratio of thermal conductivity of the fouling layer to that of the fouling layer thickness. The build up of a fouling layer can be visualized in steps of initiation, growth and asymptotic behavior as shown in figure 1.1 (a). Although fouling resistance curves do not always display an asymptotic behavior, it is said to be a typical characteristic for particulate fouling in most of the systems. The asymptote indicates a balance between particle deposition and removal rates.

In a study of biomass fouling in an entrained gas reactor, Drift [25] observed two distinct layers: an inner layer and an outer layer as shown in figure 1.1 (b). The inner layer was found to be hard, thick and compact, while the outer layer was coarser, with loosely bound particles. The detected distribution of elements over the local structure in the sample of the deposit indicated the formation of a melt in the deposit due to the presence of alkali substances.

In an earlier study, Van Beek [62] reported different structures of deposited layers for different sections in the heat exchanger. The economizer section was characterized by a thin powdery layer, while the superheater involved a two layered structure indicating strong influence of melt, temperature and boiler geometry. Figure 1.2 shows the deposits found in the economizer and superheater sections in a

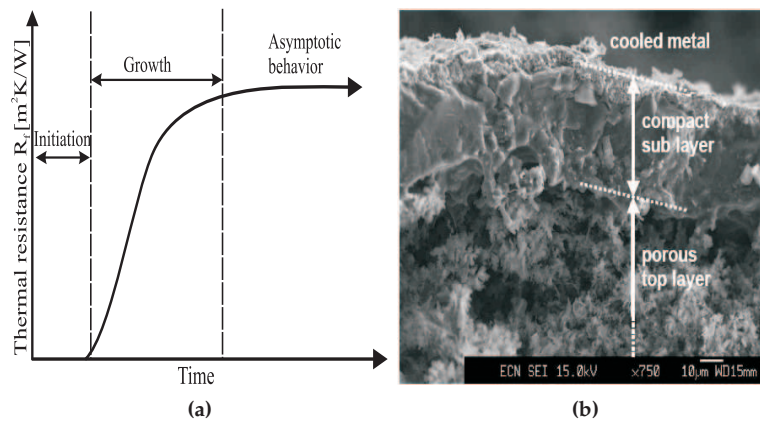


Figure 1.1: (a) Stages of particulate fouling, (b) Deposit structure [25].

Dutch waste incinerator plant. The two layered structure with an inner strong layer with a melt phase indicates the condensation of inorganic volatile species. The outer coarser layer corresponds to the deposition of coarse particulate matter. Experimental results obtained from on-site and pilot plants suggested that fouling is a highly coupled process where the global transport and chemical reaction mechanisms are coupled to the particle-surface interaction mechanisms. This results in a dynamic process of particle deposition, removal, sintering, chemical bonding etc., all of which occur simultaneously and affect each other. Thus, the complexity in completely understanding and modeling the process can be readily observed. In order to design new heat exchanger systems, to decide cleaning schedules, to design cleaning equipment, modification of existing systems etc., predictive numerical models are necessary.

1.3 Modeling slugging and fouling

A historical review of fouling of heat transfer surfaces until 1980 is covered by Somerscales [49]. The modeling approaches can be classified into empirical and mechanistic models. The traditional method or empirical approach used fouling and slugging indices, which were based on field and pilot plant data on chemical composition and fusion temperature of ash particles. One of the main problems with the indices and fouling factors was that they did not include boiler operating and design parameters. Extrapolation of this data to other fuel sources often resulted in errors. Consequently, these gave misleading results and were often unreliable [16, 65]. The inaccuracies in traditional methods prompted researchers to focus more on the fundamental aspects of fouling and slugging. Mechanistic models attempt to describe

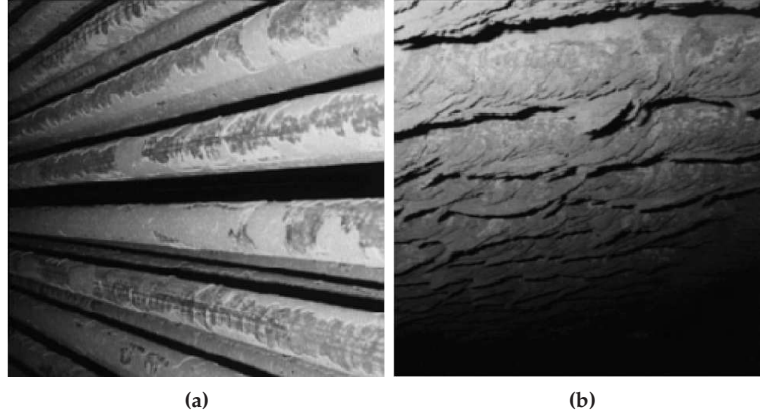


Figure 1.2: Examples of fouling layers on heat exchanger tubes. (a) Deposit of a powdery layer in economizer section and (b) Sintered deposit layer in superheater section.

processes in mineral matter transformations, ash formation process, particle adhesion, deposit growth rates, strength development etc. Several advancements have been done in this direction and the basic approach was provided by Kern and Seaton [38]. The 'fouling factors' and other indices which were used, did not take into account the effects of time dependent nature of fouling. To introduce the effect of time, Kern and Seaton proposed that fouling was due to two competing processes: the growth process and the removal process. The idea of dividing the fouling process into two subsidiary processes gave better understanding and flexibility for mathematical modeling. The rate of deposition of the fouling layer was expressed as:

$$\frac{dm_f}{dt} = \dot{m}_d - \dot{m}_r \quad (1.1)$$

where $\frac{dm_f}{dt}$ represents the net rate of accumulation of mass m_f of the fouling deposit on a unit surface area, \dot{m}_d is the rate of growth and \dot{m}_r is the rate of removal. This formulation provided a better explanation for the asymptotic behavior of fouling layer growth. If the rate of growth of the deposit \dot{m}_d was assumed to be constant and the rate of removal \dot{m}_r was taken as directly proportional to the mass m_f of the fouling deposit on a unit area of the heat transfer surface then,

$$R_f = R_{f,\infty} \left[1 - \exp\left(\frac{-t}{\tau}\right) \right] \quad (1.2)$$

where $R_{f,\infty}$ is the asymptotic value of the fouling resistance and τ is the characteristic time constant of fouling which is expressed as:

$$\tau = \frac{R_{f,\infty}}{\left. \frac{dR_{f,\infty}}{dt} \right|_{t=0}} \quad (1.3)$$

Though such a description provided a good mathematical basis, a reliable description for the deposition and removal was lacking. Modeling of deposition and removal has been a subject matter of research owing to the several complexities involved. The deposition mechanisms involved are highly dependent on the gas constituents and the properties of these constituents at different sections in the gas flow path. To put things in a simple perspective, the hot flue gases consist of solid particles of different sizes and condensible species (mainly alkali species) some of which may eventually deposit on the heat transfer surfaces. To effectively describe the process of fouling layer build up, individual mechanisms of deposition and removal must be treated properly. Observations by many researchers suggest that the particle deposition rate is a function of several parameters as described in the following section.

Particle type and concentration

Deposition of particles on to surfaces highly depends on factors like: particle size, temperature, composition, type of condensible species present, behavior of condensible species, chemical reaction. In order to develop a comprehensive mathematical model that can simulate ash deposition and its impact on overall efficiency, information of these factors must be specified. Advanced mineral ash transformation models have been developed which can describe the type of particles that will be produced along with relevant particle properties. Mechanistic modeling approach involves obtaining information of fuel composition as a first step and this information is used as an input to the mineral to ash transformation models. The mineral to ash transformation models provide considerable information regarding the type of species that would be present in the flue gases along with their properties.

Flow dynamics and particle transport mechanisms

Deposition of particles on to surfaces by flowing fluid medium can be considered as a two step process: transport of particles to the surface and adhesion of the particles to the surface. Small particles that are colloidal in nature up to the size of few sub-micrometer in diameter are mainly transported and deposited by diffusion mechanisms. The migration of particles is basically due to thermal, gravitational, magnetic and electric force fields. In a system where the fluid medium is moving, particle transport is mainly due to convective diffusion. The effectiveness of convective diffusion depends mainly on the velocity and external force fields. The fluid flow dynamics determines the way in which the particles are transported in the bulk of the fluid medium. Turbulence intensities, velocity fields and thermal gradients of the gas phase affect the particle dynamics. Also, the fluid can be affected by the particulate phase creating a two way coupling between the two phases.

Deposition mechanisms

- **Thermophoresis:** Thermophoresis is an important mechanism of micro-particle transport due to a temperature gradient in the surrounding medium. The particles experience a force in the direction of the cooler surface. Extensive studies, both theoretical and experimental, have been done to understand the nature of this phenomenon. The theory is well developed for spherical particles but for non-spherical particles, the theories are yet to be developed. Thermophoresis acts on smaller sub micrometer range particles.
- **Electrophoresis:** Similar to thermophoresis, a particle with a certain charge can experience an electrostatic force and this is termed as electrophoresis. Generally, electrophoresis is the motion of dispersed particles relative to a fluid under the influence of an electric field that is space uniform. Electrophoresis occurs because particles dispersed in a fluid almost always carry an electric surface charge. An electric field exerts electrostatic Coulomb force on the particles through these charges. The subject is quite developed in its own domain. However, the effect of electrophoresis is seldom used in heat transfer problems.
- **Brownian/Eddy diffusion:** The transport of sub-micrometer particles in the boundary layer region is greatly influenced by the mechanisms of Brownian and Eddy diffusion. The sub micrometer particles have lower inertia and follow the fluid path around the obstacles. The deposition of these particles are mainly governed by the friction velocity and the particle relaxation time.
- **Inertial impaction:** Inertial impaction is often reported to be the major transport mechanism contributing significantly to deposit formation. Particles of larger size ($> 10 \mu m$) and higher density do not follow the fluid path exactly as the motion of these particles is dominated by inertial forces. The rate of inertial impaction depends on target geometry, particle size, shape and density, impact angle, velocity and gas flow properties. If expressed in terms of characteristic length scales, inertial impaction occurs when the stopping distance of the particle exceeds the characteristic dimension of the target geometry and this can be expressed in terms of Stokes number.
- **Condensation and chemical reactions:** Condensation is a mechanism by which vapors are collected on the cooler heat transfer surfaces. Vapors that enter the thermal boundary layer around a heat transfer surface are subsequently deposited on the surface. Condensation can occur in three variations [10]:
 1. vapors may traverse the boundary layer and condense on heat transfer surface;
 2. vapors may nucleate to form a fume and subsequently deposit by thermophoresis on the surface;

3. vapors may heterogeneously condense on other particles and arrive at the surface.

Condensation deposits have no granularity and are more uniformly deposited on the tube than thermophoresis or inertially deposited material. These deposits have a strong influence on the capture efficiency and also play a vital role as a liquid bridge between particles with strong bonding forces. Along with condensation, chemical reactions, especially those of alkali species are important but are often not considered owing to many complex reactions.

A closer look at the particle deposition and removal process

Figure 1.3 shows a simplified schematic representation of particulate fouling process. The hot gases are primarily composed of particulates of different sizes along with various chemicals in vapor form. Smaller particles which are transported by diffusion can adhere to the heat exchanger surface due to electrostatic forces. However, larger particles which arrive at the surface with higher inertia impact the surface. The kinetic energy associated with the particle and physical conditions (dry, semi-molten, presence of liquid) of the particle and the surface basically determine the outcome of an impact.

Depending on the heat exchanger section, the surface of the heat exchanger and the particles may be either dry or can be coated with a liquid film due to condensation of alkali vapors as mentioned earlier. The impaction of a particle in the absence of a liquid can be broadly termed as 'dry' impaction and the impaction in the presence of a liquid can be termed as 'wet' impaction. When a particle reaches a surface, it is important to know whether the particle will stick to the surface or not. A parameter used to quantify the probability of a particle to adhere to a surface is termed as 'Sticking probability'. Thus, the process of particle deposition can be visualized in two modes: dry and wet interactions.

Particles which are deposited on the surface can be removed either by the flowing gas due to shear or when a particle of higher inertia strikes the particle layer. Figure 1.3 (a) indicates wet impaction, (b), (c) and (d) indicate sticking, rebound and removal due to dry impaction and (e) describes particle removal due to flow induced shear. Van Beek [62] performed impaction experiments for micrometer sized particles under vacuum condition. A two-body collision theory was used which is based on contact mechanics to describe the impaction process. The impaction model was based on the work of Rogers and Reed [44] which provided a means to evaluate the sticking criteria and the rebound characteristics for dry impacts. Abd-Elhady [1] performed similar experiments on particle impaction on powdery layers and evaluated the removal of particles by an impacting particle. A DEM model was also developed to study the bed dynamics for a particle impaction over a bed of particles. Particle when heated usually undergoes a sintering process where a bond develops between

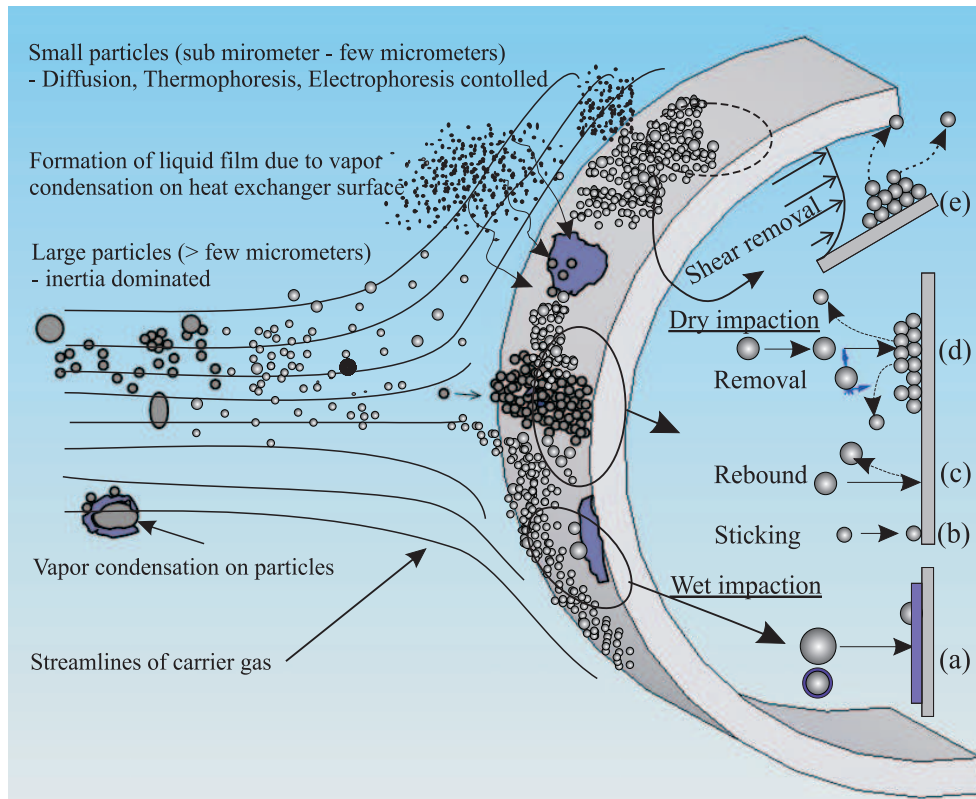


Figure 1.3: Schematic description of particulate fouling.

the particles. Abd-Elhady [1] experimentally studied the dynamics of a particle impacting a sintered layer of particles and the removal of particles from a powdery layer due to the shear induced by the flowing gas. The impaction and removal of particles under dry conditions are fairly well established.

Particles when impacting a liquid coated surface are usually treated as being stuck to the surface (i.e., their sticking probability is assumed to be 100%). While the condensation of tar components results in the formation of a highly viscous liquid film on heat exchangers, condensation of alkali species can result in a thin film of comparatively lower viscosity. Particles striking a high viscosity liquid film usually get stuck but the impact behavior over a liquid film of lower viscosity is not understood well. It has been reported that by using bigger and denser particles in the flow, particulate fouling can be reduced to some extent [2]. But these particles are associated with higher inertia and can cause erosion problems. A certain part of the particle kinetic energy will be lost in the liquid layer during impact and a clear understanding of the energy dissipated in the viscous layer is important to evaluate

sticking criteria and to analyze erosion in detail. Detailed models that describe particle impaction over liquid coated surfaces are meager and will be discussed later on.

1.4 Objective and outline of the thesis

As fouling is highly coupled to various process parameters and deposition mechanisms, the present study is mostly aimed at understanding the inertial deposition of particles on a single cylinder. A simple geometry which consists of a cylinder in a rectangular channel is considered for most part of the study. Other parameters like ash generation and transformation, chemical analysis of ash constituents and detailed flow analyses are not considered. The objective of this study is diversified in to four focus areas:

1. Evaluation of sticking conditions for a particle impacting dry and liquid coated surfaces: Different methodologies are adopted to evaluate particle sticking criteria in the literature. A brief overview of the methodologies are discussed and a literature review of particle impaction on dry and liquid coated surfaces are introduced in chapter 2. Further, particle drop experiments were carried out to compare and evaluate the available models for a particle impacting a liquid coated surface. A new methodology is used to evaluate the amount of energy lost in the liquid layer which can also be used to understand the sticking criteria and erosion of heat exchanger tubes. Chapter 3 provides the experimental method used to evaluate the impact behavior of a particle over a liquid coated surface.
2. Design and construction of an experimental facility to perform controlled fouling experiments: An experimental setup was designed and constructed which can be used to evaluate the effects of process conditions on particulate fouling. Chapter 4 describes the construction and features of the experimental facility with which experiments can be performed under controlled parameters at elevated temperatures (up to 500 °C).
3. Evaluating the effect of process conditions on particulate fouling: Several experiments were performed under controlled conditions to evaluate the effect of process parameters. The experimental results are discussed in chapter 5.
4. Devising a numerical model which is able to capture the physics of particle impaction over a surface to form a deposit layer: The information gained from the impaction experiments and a model accounting for particle removal due to shear were implemented in a commercial CFD software to simulate particle deposition under dry and wet conditions. Chapter 6 discusses the implementation and preliminary results of this implementation.

Literature review of particle deposition models

The parameter used to quantify whether or not a particle adheres to a surface is termed as 'sticking probability'. The presence of a liquid layer between the incoming particle and the surface due to vapor condensation usually promotes sticking. In some cases, larger and heavier particles are introduced in the flow to minimize fouling. However, this might lead to erosion of the heat exchanger surface. It is important to study the dry and wet impaction process to gain better understanding and to provide inputs to the numerical deposition models. A brief overview of the dry deposition process, which is quite well established is discussed. For a particle impacting a liquid coated surface, two types of modeling approaches were found in the literature. The models are analyzed in detail and are compared with each other to evaluate their limitations and applicability.

2.1 Critical Stokes number for inertial impaction

The onset of inertial effects is quantified by the Stokes number which describes the flow characteristics of a particle in a given fluid medium. It is usually viewed as the ratio of particle relaxation time to a characteristic time scale for the flow around the obstacle. Thus,

$$Stk_f = \frac{\tau_p}{\tau_{flow}} \quad (2.1)$$

The particle relaxation (or response) time is the characteristic time scale for a particle to respond to the changes in fluid flow and is given by the relation

$$\tau_p = \frac{\rho_p d_p^2}{18\mu_f} \quad (2.2)$$

where ρ_p is the particle density, d_p is the particle diameter and μ_f is the dynamic viscosity of the fluid.

The characteristic time scale for the flow is the ratio of the characteristic dimension of the obstacle to the free stream velocity of the flow and thus, the Stokes number can be written as:

$$Stk_f = \frac{\rho_p d_p^2 U_{f\infty}}{18\mu_f R_{cyl}} \quad (2.3)$$

where R_{cyl} is the radius of the cylinder.

By analyzing the motion of particles in the stagnation region of an inviscid flow, it has been shown that particle impaction does not occur until a critical Stokes number is reached [28]. A critical Stokes number of $1/8$ is defined for cylindrical obstacles. For flat plates and spheres, the critical Stokes numbers are 0.25 and 1.2119 respectively. In these analyses, the effect of the presence of a boundary layer is neglected, but is said to be important when the particle size is in the same order as that of the boundary layer thickness. Further, the changes in the drag force as the particle approaches the wall is neglected in the analytical derivation of critical Stokes number and usually a numerical scheme is adopted to resolve the same. The analysis however provides a good indication of the limiting condition for the onset of inertial effects and can be found in Ingham et al. [32]. Figure 2.1 (b) schematically shows the

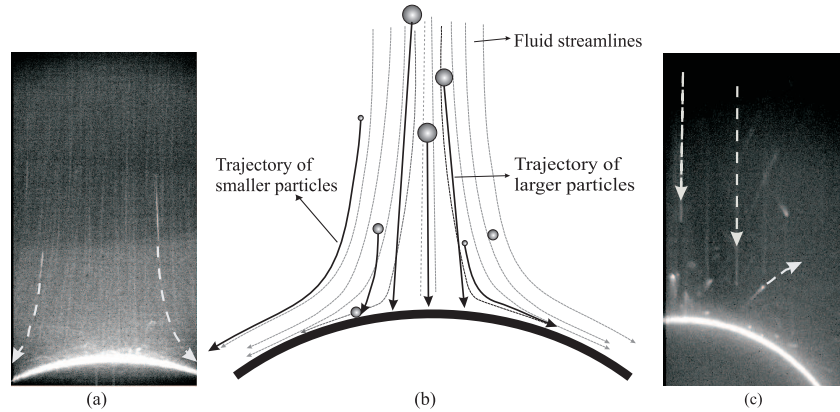


Figure 2.1: (a) Image of a high speed recording for $Stk_f = 0.18$ (mean $d_p = 20 \mu\text{m}$), (b) Description of trajectory of large and small particles and its relation to Stokes number and (c) Image of a high speed recording for $Stk_f = 9$ (mean $d_p = 143 \mu\text{m}$).

results of an experimental observation of the trajectories of the particles. Figures 2.1 (a) and (c) show the trajectories of particles with a mean diameter of 20 and 143 μm , respectively. The images were recorded with a high speed camera for the particles dispersed in a downward flowing air around a cylindrical tube of 51 mm diameter with a free stream velocity of 1.5 m/s. The corresponding free stream particle Stokes numbers are approximately 0.18 and 9 respectively. Particles with a Stokes number larger than the critical value impact the surface. At this juncture, it is important to evaluate the sticking probability of the particle with the surface which is discussed in the rest of this chapter. A particle can impact a clean surface or a surface with a pre deposited layer of particles. For simplicity, in the following sections, the term "surface" is used for both cases and a clear distinction is made wherever necessary.

2.2 Approaches to evaluate sticking probability

The sticking probability of a particle that reaches a surface mainly depends on two groups of parameters: the first relates to the properties of the particles itself (temperature, composition, angle of approach, velocity of approach) and the second one is related to the surface properties such as: roughness, temperature, composition and structure of any previously deposited layer. It is difficult to give an exact mathematical description for each and every parameter which governs the probability of a particle to stick to a surface. Hence, in order to simplify, the concept of sticking probability is often used. There are three different approaches to evaluate the sticking probability: the melt phase approach, the critical viscosity approach and the critical velocity approach. These are described and evaluated in the following sections.

2.2.1 Melt phase approach

The process of deposit initiation and growth is usually thought to involve either liquids formed on the tube from condensed alkalis or low viscosity supercooled impinging fly ash particles [68]. The growth of a deposit layer in the presence of condensed material has been studied by several authors [41, 45]. Alkali compounds are invariably present in biomass feedstock and these are usually present as vapors (or submicron mists) in the flue gas. Alkali vapors condense in the boundary layer, on ash particles and on heat transfer surfaces. This acts like a 'glue' and aids in the capture of particles. It has been proposed by Rosner and Nagarajan [45], that the sticking probability depends on the amount of 'glue' available for particle capture. The properties of deposits are dependent of the melting behavior of the material in the deposit. The temperature where the first melt forms is termed as T_0 and the temperature where the last solid phase disappears is termed as T_{100} . The range over which these two characteristic temperatures occurs can be several hundreds of centigrade depending on the composition. The other interesting temperatures within this

range is that of sticking temperature, T_s and flow temperature, T_f . The sticking temperature T_s is defined as the temperature above which the material sticks to a metal surface when it strikes it. This happens when the amount of liquid phase in the material exceeds a certain value. It is reported that for alkali and alkali mixtures, a deposit becomes sticky when it contains 15% melt [33, 60]. The other important temperature is the flow temperature and is defined as the temperature where the amount of liquid is large enough for the deposit to flow down along a vertical superheater tube. For alkali rich deposits this occurs when about 70% of the deposit is molten. Thus,

$< 15\%$ mass of molten phase \implies non-sticky
 15 to 70% mass of molten phase \implies sticky
 $> 70\%$ mass of molten phase \implies flowing

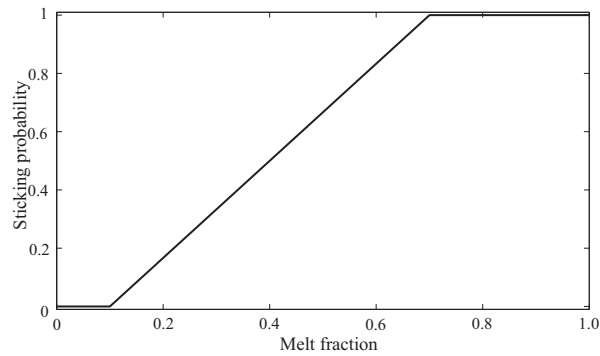


Figure 2.2: Sticking probability as a function of melt fraction for Potassium salts [31].

The mass of molten phase can be evaluated either by using chemical equilibrium calculations at a given surface temperature (along with certain chemical composition) or by using experimentally determined melting curves. Hansen [31] reported melting curves with varying temperatures for different slag deposits. The sticking probability of Potassium salts with varying melt fraction as adopted from Kær [35] is shown in figure 2.2. For a melt fraction of 0.7 and greater, particles are taken as perfectly sticky.

2.2.2 Critical viscosity approach

This modeling approach is widely used for deposition under high temperatures (>1000 °C) and especially for slagging in coal fired and co-fired boilers with silica rich particles. The basis of this model lies in the rheological aspects of ash. The mineral particulates are generally heated to very high temperatures during which they

melt to form spherical particles of low viscosity [16]. As these particles flow through the furnace, they cool down and their viscosity increases. Some particles will strike the tube surface and may initially be retained by weak forces. If the particles are at a high enough temperature, their viscosity will be sufficiently low and will fuse together to form a strong bond. Ash viscosity is highly dependent on temperature and is hence the determining factor. A detailed treatment of the subject matter in terms of ash viscosity measurements, viscosity-temperature relationships, ash crystallization concepts and critical viscosity concepts can be found in Vargas et al. [63].

Molten ash particles when cooled, precipitates a solid phase due to rapid crystallization and this will have a vast effect on the rheological behavior of the sample and has been a major subject of importance. Figure 2.3 (a) shows the relationship between temperature and viscosity. The critical point, T_{cv} indicates a point of abrupt change in the viscosity-temperature relationship.

$T < T_{cv}$: viscosity varies strongly with temperature
 $T > T_{cv}$: viscosity varies weakly with temperature.

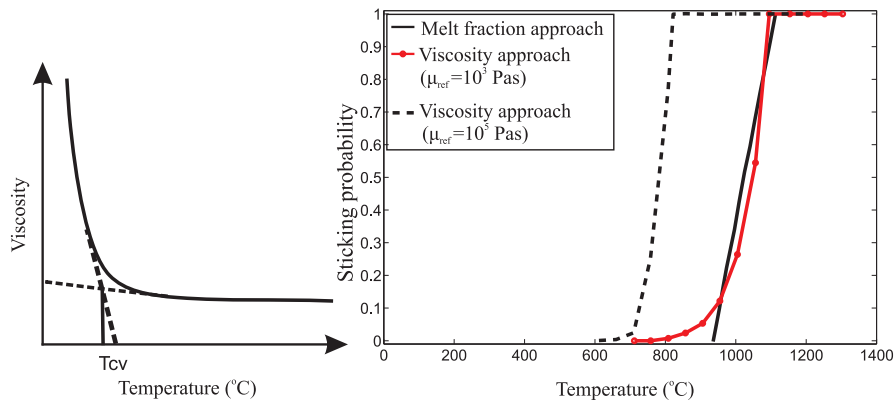


Figure 2.3: (a) Typical temperature-viscosity relationship for ash particles [63] (b) Comparison between melt phase and viscosity approach [35].

The sticking probability is taken to be inversely proportional to the viscosity. A reference viscosity value is defined and viscosities lower than this value imply that the particles are perfectly sticky. For values greater than the reference viscosity, the particles are treated as non-sticky.

$$P(T, \psi) = \frac{\mu_{ref}}{\mu} \quad \text{if } \mu > \mu_{ref} \quad (2.4)$$

$$P(T, \psi) = 1, \quad \text{if } \mu \leq \mu_{ref} \quad (2.5)$$

where, P is the sticking probability as a function of temperature and particle composition, T is the temperature of the particle at which the viscosity is determined, ψ is the particle chemical composition, μ_{ref} is the particle reference viscosity and μ is the particle viscosity. The reference viscosity is the maximum viscosity of a particle which has a 100% sticking probability which is determined using the viscosity models of Urbain et al. [61] or Senior and Srinivasachar [47]. Based on the chemical composition of the fly ash, either the viscosity of the particle can be calculated or the amount for melt fraction can be evaluated. In a work related to modeling deposit formation in straw fired grate boilers, Kær [35] compares the critical viscosity and melt phase approach for high silica ashes which is shown in figure 2.3 (b). It can be observed that the melt fraction has a similar sticking probability trend as that of critical viscosity with a reference value of 10^5 . However, for a different reference value the sticking probability changes with temperature and thus, the choice of the reference value for viscosity has a major effect on sticking probability.

2.2.3 Critical velocity approach

This approach is based on the concept of particle kinetics and the energy interactions involved in particle-wall and inter-particle collisions. The concept of critical velocity stems from the theories of contact mechanics. The outcome of an impaction process depends upon the physical, chemical and thermal properties of the interacting surfaces. A particle traveling with a certain velocity possesses a certain amount of kinetic energy associated with it and based on the principles of contact mechanics, the outcome of the impaction can be accurately described. Based on a 2D-Discrete Element Method (DEM), Werner [66] proposed that the interaction of an incident particle with a bed of particles can be described as a binary collision using an effective mass for the target. Van Beek [62] used the two body approach of Werner based on a particle undergoing elastic-plastic deformations for particle deposition. Rosner and Nagarajan [45] considered the sticking probability of a single impact event which is taken as either 1 or 0 and is mainly dependent on specific contact physics. They proposed that the abrupt transition from 1 to 0 occurs whenever some parameter, say impact velocity, reaches a critical value if all other parameters are held constant. In general, all the particles of a given size are assumed to be captured if the impact normal velocity is below a critical value (v_{cr}), beyond which a particle begins to rebound. Figure 2.4 shows the rebound characteristic of a Potassium sulphate particle impacting another particle of the same material of the same size ($50 \mu\text{m}$). Detailed information on the material properties and the model can be found in Van Beek [62]. A limiting velocity (v_{lim}) is defined which indicates the onset of plastic deformation during the impact. The plot indicates three distinct regions: a sticking region where the particle impact velocity is less than the critical rebound velocity, a region of pure elastic rebound in between the critical rebound velocity and the limiting velocity. The model provides an accurate description of the conditions

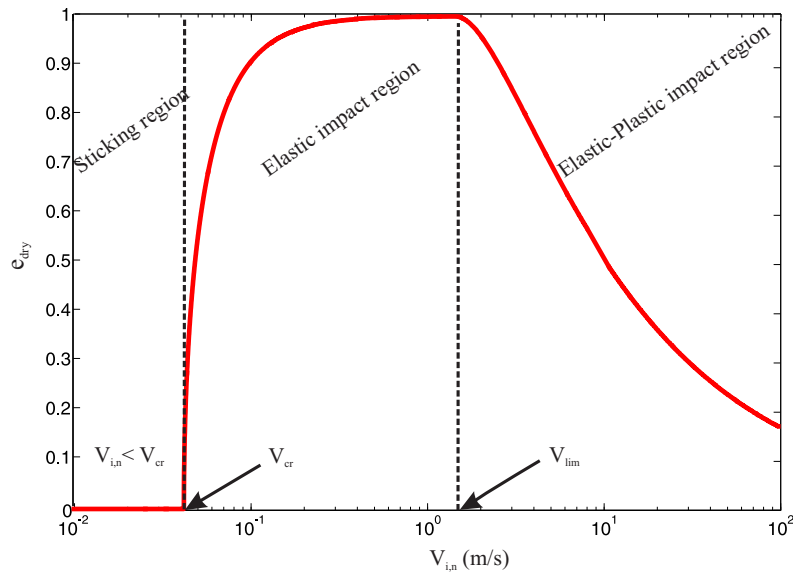


Figure 2.4: Rebound characteristics of a $50 \mu\text{m}$ K_2SO_4 particle impacting an equal sized particle of the same material [62].

under which a particle sticks and if it rebounds, the momentum loss over the impact process can be evaluated.

2.2.4 Applicability and limitations of the models

Alkali species have a dominant effect on the deposition of particles. However, the melt fraction approach does not predict any deposition for temperatures less than 600°C . A clear description as to why the particles stick to surfaces within a certain range of molten phase and not otherwise is not dealt with explicitly in the literature. It is known that solid particles, interacting with a dry surface or another particle coated with a thin liquid film or even without any 'melt phase' shows fouling behavior. This modeling approach is said to be suitable for high alkali content ashes and for modeling slagging behavior.

The critical viscosity approach is mainly used to model slagging in coal fired boilers. The criteria for selecting the critical viscosity is not deterministic and rather the use of viscosities differing as much as four orders of magnitude have been reported in the literature [35]. Thus, the melt phase and viscosity approach are applicable to special cases and for certain sections of a heat exchanger.

The critical velocity approach can be viewed as a generalized formulation which can be used to describe particle deposition and also removal, provided that the required particle properties are known. Based on the particle properties, deposition

can be quantified addressing both sticking and removal. The critical velocity approach is computationally demanding, but it is foreseen that a detailed modeling will aid in better understanding of the fouling process.

2.3 Particle impaction over a dry surface

Particle impacting a surface at normal incidence can be viewed in two phases namely: an approach phase and a restitution phase [62]. The approach phase starts when the incident particle comes in contact with the substrate during which stresses are developed in the contact region. The stresses are short ranged and decrease rapidly with increasing distance from the contact area leading to concentration of internal energy in a small region around the contact area. If the pressure induced due to compression forces overcome the material yield limit, plastic deformation occurs in the softer material while the relative velocity becomes zero and marks the end of the approach phase. In the restitution phase, the stored elastic energy is imparted back to the particle resulting in particle rebound. The ratio of particle velocity before contact and the maximum particle velocity during rebound is termed as the coefficient of restitution which is usually denoted as 'COR' or as 'e'. This quantifies the momentum loss over the entire process of impaction and rebound. In principle, part of the kinetic energy associated with the impacting particle is dissipated as elastic and surface wave propagations, partly to vibration, sound and heat generation while most of the energy goes into purely elastic or elastic-plastic deformation. A detailed explanation of the process can be found elsewhere [15, 44, 62]. The basic energy balance at the end of the approach phase for a particle undergoing elastic-plastic deformation is given by the relation:

$$Q_k + Q_{A,a}(F) = Q_{el} + Q_{pe}(F) + Q_p(F) \quad (2.6)$$

where F is the contact load and Q_k is the kinetic energy of the incident particle given by

$$Q_k = \frac{1}{2} m_p v_{i,n}^2 \quad (2.7)$$

m_p being the mass of the impacting particle and $v_{i,n}$ being the particle normal velocity before collision.

The term $Q_{A,a}(F)$ represents the surface adhesion energy caused by the attractive forces between the interacting surfaces and is described as:

$$Q_{A,a}(F) = \Gamma \pi \left(r_{el}^2 + \frac{F - F_{el}}{\pi y} \right) \quad (2.8)$$

Γ being the work of adhesion defined by $\Gamma = 2\sqrt{\lambda_1 \lambda_2}$. λ_1 and λ_2 are the free surface energies associated with the particle and the surface, r_{el} is the radius of the contact area. F is the contact load and if the contact pressure exceeds the elastic load limit

'y', plastic deformation starts and the limiting case where the maximum pressure is the same as the elastic load limit, F_{el} is defined as the contact load at the limiting point and is given by:

$$F_{el} = \left(\frac{2}{3}\pi\right)^3 \frac{R^{*2}}{\left(\frac{4}{3}E^*\right)^2} y^3 \quad (2.9)$$

R^* is the effective radius given as:

$$R^* = \frac{R_1 R_2}{R_1 + R_2} \quad (2.10)$$

where R_1 and R_2 corresponds to the radii of the interacting particles. E^* is the effective Youngs modulus defined as

$$\frac{1}{E^*} = \frac{1 - \nu_1^2}{E_1} + \frac{1 - \nu_2^2}{E_2} \quad (2.11)$$

where E_i and ν_i are Young's modulus and Poisson ratio for body i (i=1,2).

The term Q_{el} represents the amount of elastic energy stored in the contact area and is given by the relation

$$Q_{el} = \frac{2}{5} \left(\frac{2}{3}\right)^5 \frac{\pi^5 R^{*3} y^5}{\left(\frac{4}{3}E^*\right)^4} \quad (2.12)$$

During plastic deformation, the area in which plastic deformation occurs is also subjected to elastic deformations which is recovered when the contact load is released. This is given by the relation:

$$Q_{pe}(F) = \frac{1}{2} h_{el}(F - F_{el}) \quad (2.13)$$

where h_{el} is the elastic deformation defined by the relations:

$$h_{el} = \left(\frac{2}{3}\pi\right)^2 \frac{R^*}{\left(\frac{4}{3}E^*\right)^2} y^2 \quad (2.14)$$

The contact load can be written as a sum of elastic and plastic components as:

$$F = F_{el} + F_p \quad (2.15)$$

where F_p is

$$F_p = \pi r_p^2 y \approx 2\pi R^* H y \quad (2.16)$$

H being the final remnant deformation depth. Experimentally, if one can measure the volume of the indentation formed and knowing the material properties, the energy that was dissipated in the formation of the indentation can be quantified. This method of measuring indentation is widely used to determine hardness of a material

by Rockwell, Vicker and Brinell hardness testing methods.

Q_p represents the amount of energy expended in the plastic flow of the material and is given by the relation:

$$Q_p(F) = \frac{(F - F_{el})^2}{4\pi R^*y} \quad (2.17)$$

For a particle impacting another particle or a surface under dry conditions as discussed in the previous section, the particle sticks to the surface if the sum of stored elastic energy that is released to the particle in its restitution phase is less than the adhesion energy during the restitution phase. i.e.,

$$Q_{el} + Q_{pe} \leq Q_{A,r} \quad (2.18)$$

2.4 Particle impaction over a liquid coated surface

The collision of a particle over a liquid coated surface results in a lower restitution coefficient as compared to a similar dry collision due to viscous losses in the liquid layer. Eirich and Tabor [26] reported that if the surfaces are covered with a thin film of a highly viscous liquid, during an impact of a flat hammer over the film, high pressures are developed and transmitted through the liquid layer. Clark and Burmeister [20] observed that the pressure required for an impinging particle to force the fluid from the gap is of high magnitude which reduces the impact velocity of the particle. A first step towards modeling the particle impaction over liquid coated surface was established by Davis et al. [23]. Barnocky and Davis [9] performed experiments by dropping particles over liquid coated surfaces to determine the drop height beyond which the particles rebounded and conclude that the results agreed well with the model proposed by Davis et al. [23]. Similar experiments were conducted and the rebound velocities were measured by Davis et al. [21]. They observed that the apparent restitution coefficient increased with increasing Stokes number and the results were in good agreement with the model of Davis et al. [23]. Lian et al. [39] proposed a model on the same lines as that of Davis et al. [23] with modified coefficients. However, Antonyuk et al. [7] suggested a detailed model to determine the wet coefficient of restitution by accounting the various forces acting on the particle during impact and subsequent rebound of the particle. Among other articles reviewed, the work of Davis et al. [23] and Antonyuk et al. [7] were found to be most relevant for modeling particle deposition in fouling process and are analyzed in the following sections. A brief overview of the models and numerical comparison for both models are presented in the following sections. For simplicity, henceforth, the model proposed by Davis et al. [23] is referred to as 'Model 1' and that of Antonyuk et al. [7] is referred to as 'Model 2' where 1 and 2 are chosen based on chronological appearance.

Consider a flat substrate which is coated with a liquid film of known viscosity

(μ_L) and layer thickness (h_L). If a spherical particle (ball) of radius r_p and mass m_p is dropped vertically over the liquid coated substrate at normal incidence velocity ($v_{i,n}$) as shown in figure 2.5, a non-dimensional Stokes number can be defined for the process. In line with equation 2.3, with $v_{(i,n)}$ as the incident velocity and r_p as the characteristic length scale, the resultant Stokes number is given as:

$$Stk = \frac{m_p v_{i,n}}{6\pi\mu_L r_p^2} \quad (2.19)$$

The Stokes number provides a measure of the inertia of the particle relative to the

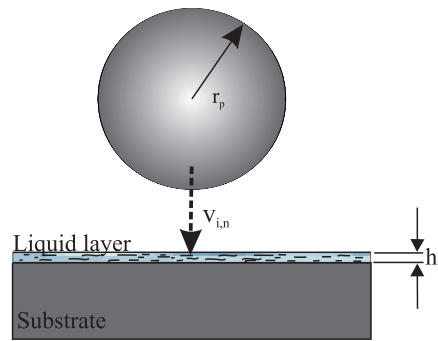


Figure 2.5: Schematic representation of wet impact.

viscous forces of the liquid layer [23]. Similarly, an initial gap Reynolds number is defined as

$$Re_{gap} = \frac{v_{i,n} h_L}{\nu_L} \quad (2.20)$$

The gap Reynolds number indicates the ratio of particle inertia to the viscous force with a characteristic dimension based on the liquid layer thickness. ν_L is the kinematic viscosity of the liquid. The rebound characteristics for the wet impact is given by the relation:

$$e_{wet} = \frac{|v_r|}{v_{i,n}} \quad (2.21)$$

where e_{wet} is the wet coefficient of restitution, v_r is the rebound velocity and $v_{i,n}$ is the incident velocity of the particle.

2.4.1 Model 1

Davis et al. [23] derived an analytical expression for the elastic deformation on two elastic spheres approaching each other with a fluid medium in between them. As the particles approach each other, the fluid in between is squeezed out while the fluid exerts a hydrodynamic force on the particle due to which elastic deformation occurs.

The surface of the particle and the substrate is assumed to be hydrodynamically smooth and the inertial effect of the fluid is neglected. The theoretical development is also based on the condition that the gap Reynolds number is small ($Re_{gap} \ll 1$). The pressure profile in the fluid layer in the line of action is obtained from the lubrication theory and the elastic deformations induced in the particle due to the pressure is evaluated. A detailed theoretical development of the model can be found in Davis et al. [23].

The viscous lubrication force resisting the motion of the particle (hydrodynamic force) is given by the relation:

$$F_{vis} = \frac{6\pi\mu_L r_p^2 v}{z} \quad (2.22)$$

where z is the instantaneous distance between the nose of the undeformed sphere and the substrate. The equations of particle motion are

$$\frac{dz}{dt} = -v(t) \quad (2.23)$$

$$m_p \frac{dv}{dt} = -F_{vis}(t) \quad (2.24)$$

where $v(t)$ is the velocity of the particle and F_{vis} is the hydrodynamic force that acts on the particle. Substituting equation 2.23 in 2.22 and using the resulting form in equation 2.24 yields:

$$dv = \frac{6\pi\mu_L r_p^2}{m_p z} dz \quad (2.25)$$

Using the relation 2.19, the terms can be rearranged to get

$$dv = \frac{v_{i,n}}{Stk} \frac{1}{z} dz \quad (2.26)$$

Integrating equation 2.26 with the initial condition $v = v_{i,n}$ when $z = z_o$ takes the form:

$$\frac{v}{v_{i,n}} = 1 - \frac{\ln(z_o/z)}{Stk} \quad (2.27)$$

where z_o is the initial separation distance at which the viscous forces begin to act on the particle. Equation 2.27 indicates that the particle will slow down as it approaches the substrate due to the viscous forces. Barnocky and Davis [9] suggested that the particle has to penetrate to a certain depth in the liquid layer for the viscous forces to become significant and chose a distance $z_o = 2h_L/3$. The particle is assumed to rebound when it reaches a separation distance $z = z_r$ (which is unknown and has to be evaluated). The magnitude of the rebound velocity is reduced by a factor e_{dry} which accounts for the energy dissipation in the solid and the rebound behavior of a particle is defined in terms of a wet restitution coefficient as:

$$e_{wet} \equiv e_{dry} \left(1 - \frac{Stk_{cr}}{Stk} \right), \quad Stk > Stk_{cr} \quad (2.28)$$

where Stk_{cr} is the critical Stokes number ($Stk_{cr} = \ln(z_o/z_r)$) which is the limiting value below which a particle will not rebound. If the colliding surfaces have sufficiently large roughness elements, the surfaces will come into physical contact and the value of z_r is equated to the dimension of the maximum roughness element. However, to derive an expression for the critical Stokes number, Davis et al. [23] assume the surfaces to be hydrodynamically smooth and using the theory of linear elasticity, the deformation of the particle at the axis of symmetry due to the lubrication force is approximated by:

$$\delta_h \approx \frac{\theta F_{vis}}{r_h} \quad (2.29)$$

where r_h is a characteristic radius of the load area which is subjected to high pressures. The surface of the sphere near the axis of the symmetry is approximated by $h = z + r^2/2r_p$, r being the radial coordinate. The elastic deformation and the radial coordinate are shown in figure 2.6. The characteristic distance over which the

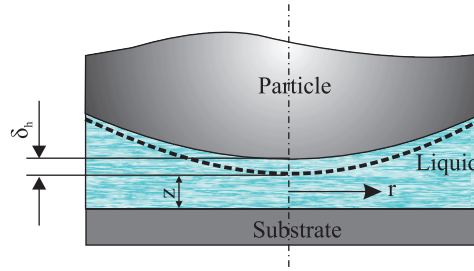


Figure 2.6: Schematic representation of elastic deformation at the axis of symmetry due to distributed lubrication force Davis et al. [22].

viscous force is distributed is approximated as $r_h = \sqrt{2rz}$ and θ is the inverse of the effective or composite Young's modulus which is defined as $\pi\theta = 1/E^*$ (see equation 2.11 for E^*). Thus, equation 2.29 takes the form:

$$\delta_h = \frac{\theta}{\sqrt{2r_p z}} \frac{6\pi\mu_L r_p^2 v}{z} \quad (2.30)$$

The deformation δ_h is considered to be substantial when it is comparable to the distance separating the undeformed surface [22] or $\delta_h = z = z_r$. The relative velocity in principle can be obtained by equation 2.27, but the authors make a simpler choice and take the value as half of the initial velocity so that the particle maintains a significant fraction of its velocity by the time deformation becomes important [22]. Thus, equation 2.30 yields

$$z_r = \left(\frac{3\pi\theta\mu_L r_p^{3/2} v_{i,n}}{\sqrt{2}} \right)^{2/5} \quad (2.31)$$

Defining an elasticity parameter which provides a measure of the tendency of the solids to deform as:

$$\epsilon = \frac{4\theta\mu_L v_{i,n} r_p^{3/2}}{z_0^{5/2}} \quad (2.32)$$

Substituting the necessary forms for Stk_{cr} yields

$$Stk_{cr} = \frac{2}{5} \ln \left(\frac{\sqrt{2} z_0^{5/2}}{3\pi\theta\mu_L v_{i,n} r_p^{3/2}} \right) = 0.40 \ln \left(\frac{1}{\epsilon} \right) - 0.20 \quad (2.33)$$

Thus, knowing e_{dry} and the properties of the interacting particles and liquid, e_{wet} can be evaluated. Figure 2.7 shows the typical plot of particle rebound behavior evaluated using model 1.

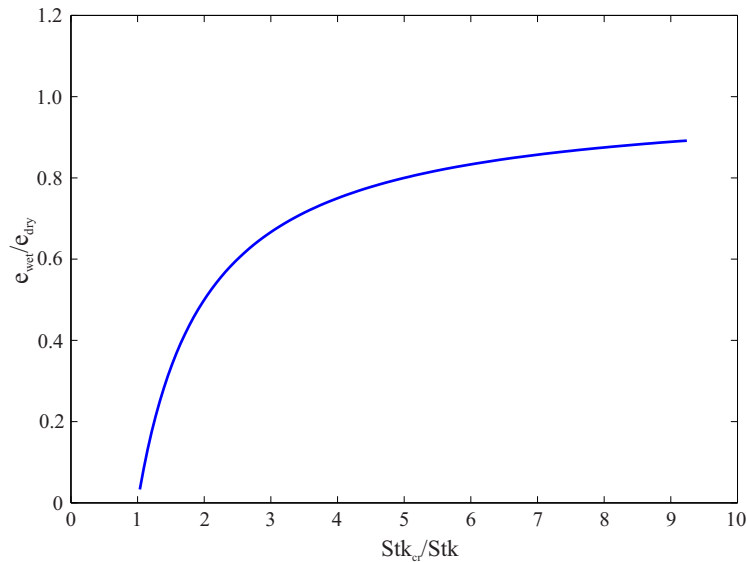


Figure 2.7: Rebound characteristics for a particle impacting a liquid coated surface as a function of Stokes number Davis et al. [22].

2.4.2 Model 2

Antonyuk et al. [7] proposed a model to evaluate the energy loss during the normal impact of spherical granules on a flat steel plate coated with a liquid layer. The model considers different forces acting on the particle such as viscous, capillary, contact, surface tension, buoyancy and gravitational forces to evaluate the energy lost by the particle in the impact process. The overall impaction process is divided into four different phases as shown in figure 2.8

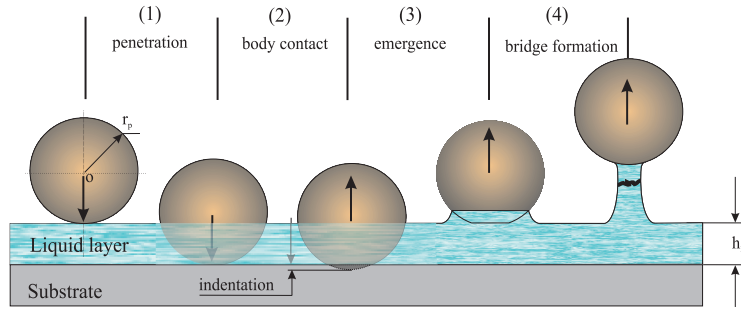


Figure 2.8: Different phases involved in particle impact over a liquid coated surface [7].

1. The initial phase corresponds to the duration from which the particle contacts and penetrates the liquid layer surface, and travels through the liquid layer.
2. The second phase relates to the contact between the particle and the substrate which can result in an elastic or elastic-plastic deformation.
3. The rebound of the particle from the substrate until it exits the liquid layer thickness is termed as the third phase.
4. As the particle leaves the surface of the liquid layer, a liquid bridge is formed between the particle and the liquid layer. At a certain height, the liquid bridge ruptures and corresponds to the last phase.

The restitution coefficient for wet impactation is defined by:

$$e_{wet} = \sqrt{1 - \frac{Q_{diss,tot}}{Q_{k,0}}} \quad (2.34)$$

where $Q_{diss,tot}$ corresponds to the energy loss over the whole process and $Q_{k,0}$ is the particle kinetic energy before the first phase.

The kinematic equations that describe the relative motion of the particle impacting a substrate coated with a liquid layer is expressed in the form:

$$m_p \frac{d^2 \vec{x}}{dt^2} = \vec{F}_{p,g} + \vec{F}_t + \vec{F}_b + \vec{F}_D + \vec{F}_c + \vec{F}_{vis} + \vec{F}_{cap} + \vec{F}_{l,g} \quad (2.35)$$

where x is the immersed depth of the particle in the liquid layer which can be related to the position of the particle center. The immersed depth is thus related to the distance between the surface and the particle tip as $z = h_L - x$ (see figure 2.10). The terms on the right hand side of equation 2.35 represent different forces acting on the particle throughout the whole process which are briefly described here. A detailed description with relevant references can be found in Antonyuk et al. [7]. The

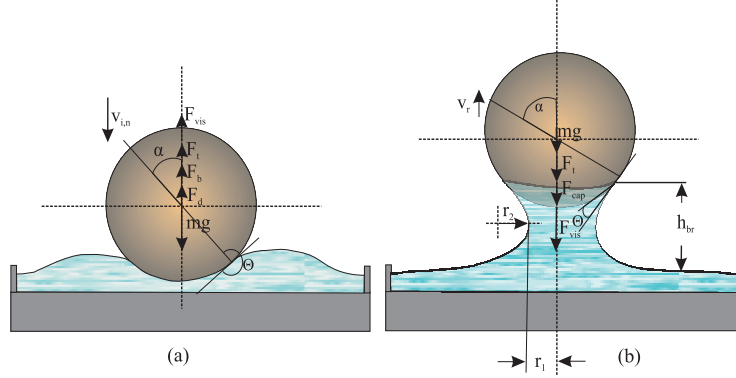


Figure 2.9: Different forces acting on the particle (a) during penetration and (b) during rebound phase. Adopted from [7]. Angle α is shown on the opposite and vector notation for forces are not shown for clarity.

forces acting on the particle during penetration and rebound phases are schematically shown in figure 2.9.

$\vec{F}_{p,g} = m_p g$ is the gravitational force due to the particle and $\vec{F}_{l,g}$ is the added mass on the particle due to the liquid layer during the rebound phase which is taken to be 10% of the particle volume.

\vec{F}_t is the surface tension force which depends on the surface properties of the particle and liquid. The vertical component of the surface tension force is given as:

$$\vec{F}_t = \pm \gamma_{l,a} \pi d_p \sin(\alpha) \sin(\Theta + \alpha) \quad (2.36)$$

where $\gamma_{l,a}$ is the liquid-air surface tension and θ is dynamic contact angle which depends on the wetting conditions of the particle and α is half central angle shown in figure 2.9. Due to the non-availability of information on the dynamic contact angle, Antonyuk et al. [7] assume a constant angle of 175° for the penetration and 25° for the rebound phase respectively. As the amount of energy dissipated due to surface tension is very small, this assumption is said to be valid.

The buoyancy force is expressed as:

$$\vec{F}_b = \pm \frac{1}{6} \pi x (3r_p^2 - x^2) \rho_L g \quad (2.37)$$

where ρ_L is the density of the liquid. The drag force is given by the relation

$$\vec{F}_D = \pm \frac{1}{2} c_D \rho_L A_D v_p^2 = \pm \frac{1}{8} \pi c_D \rho_L d_p^2 \sin^2(\alpha) v_{i,n}^2 \quad (2.38)$$

The drag coefficient c_D depends on the particle Reynolds number $Re = v_{i,n} d_{p,eq} \rho_L / \mu_L$, with $d_{p,eq}$ as the equivalent diameter of the penetrated part of the particle and is evaluated using a relation which holds good for a wide range of Re (0 to 4.10^5).

The second phase is dominated by the contact force which is given by the sum of the elastic deformation and the damping force.

$$\vec{F}_{ct} = \vec{F}_{ct,el} + \vec{F}_{ct,d} \quad (2.39)$$

The force induced by elastic deformation with $R^* = \left(\frac{1}{r_p} + \frac{1}{r_g}\right)^{-1} \approx r_p$ is given by the relation:

$$\vec{F}_{ct,el} = \frac{2}{3}E'\sqrt{r_px_{ct}^3} \quad (2.40)$$

with x_{ct} being the contact displacement and the effective modulus here is related to equation 2.11 as $E' = 2E^*$. The contact force damps the impact and is liable for a big part of energy dissipation and is given as:

$$\vec{F}_{ct,d} = \alpha_d \sqrt{m_p k'_{el} x_{ct}^{0.25}} \frac{dx_{ct}}{dt} \quad (2.41)$$

The damping force is strongly controlled by the damping parameter α_d which has to be determined by falling experiments. The Hertzian constant k'_{el} describes the displacement-related stiffness and is given by:

$$k'_{el} = \frac{2}{3}E'\sqrt{R^*} \quad (2.42)$$

The constant values α_d and k'_{el} can be evaluated in compression and fall experiments. During the formation of the bridge (interval 4) a capillary force acts on the particle and is given by:

$$\vec{F}_{cap} = -\gamma_{la} \left(\frac{1}{r_1} - \frac{1}{r_2}\right) \pi r_p^2 \sin^2(\alpha) \quad (2.43)$$

The radii r_1 and r_2 are evaluated using an empirical formulation based on experimental observations. More details on this can be found in Antonyuk et al. [7].

Antonyuk et al. [7] divide the liquid film thickness into three distinct regions to evaluate the viscous force which arise due to the resistance offered by the liquid layer to the particle motion. A constant viscous force is assumed to act on the particle, if the distance between the nose of the particle and the surface (z) is more than a predetermined value ($z_{L,max}$) and given by the relation:

$$\vec{F}_{vis1} = \pm \frac{6\pi\mu r_p^2}{z_{L,max}} \frac{dx}{dt}; \quad z \geq z_{L,max} \quad (2.44)$$

In the second region, where z is between ($z_{L,max}$) and the height of the surface roughness of the substrate or particle (z_r), the viscous force is given by the relation:

$$\vec{F}_{vis2} = \pm \frac{6\pi\mu r_p^2}{z} \frac{dx}{dt}; \quad z_r \leq z \leq z_{L,max} \quad (2.45)$$

For the third region, in order to limit the viscous force ($F_{vis} \rightarrow \infty$ as $z \rightarrow 0$), the following relation is used:

$$\vec{F}_{vis3} = \pm \frac{6\pi\mu r_p^2}{z_{L,min}} \frac{dx}{dt}; \quad z \leq z_r \quad (2.46)$$

Figure 2.10 schematically shows the comparison between the different viscous terms used in model 2 and that of model 1.

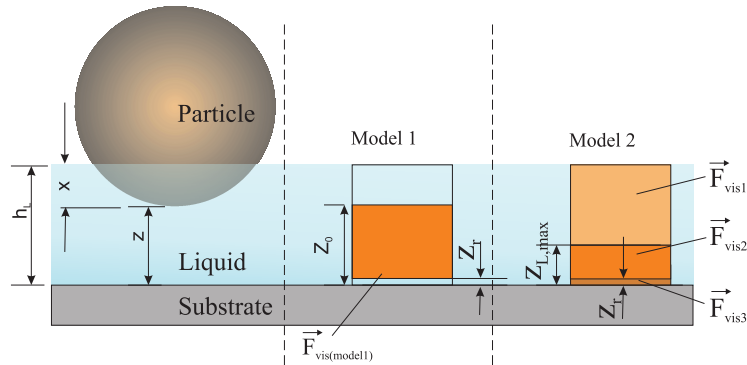


Figure 2.10: Schematic presentation of viscous force terms used in model 1 and 2.

2.4.3 Comparison of models

Model 1 of Davis et al. [23] was experimentally validated by Barnocky and Davis [9] and Davis et al. [22] by their drop experiments where the liquid viscosity, ball size, density and liquid layer thickness were varied.

Model 2 of Antonyuk et al. [7] was validated by dropping aluminum oxide particle of one size and at constant velocity on liquid layer of varying thickness.

The experimental parameters which the authors have used to validate their models are listed in table 2.1. It can be observed that the experiments corresponding to model 1 involve liquids of high viscosity as compared to that used to evaluate model 2.

The use of high viscosity liquids and thin liquid layers result in low gap Reynolds numbers. The derivation of model 1 is also based on the assumption that the interacting surfaces undergo small elastic deformation and the gap Reynolds number is less than unity. The use of nylon and steel balls impacting on a quartz substrate coated with a highly viscous thin liquid film satisfies the requirement of low Re_{gap} and elastic deformations.

As mentioned earlier, the experimental data of model 2 relates to single particle type and size along with a constant impact velocity, which results in a single

Table 2.1: Experimental data for Model 1 and Model 2 validation cases

	Model 1	Model 2
Particle	Nylon 66	$\gamma - Al_2O_3$
	Stainless Steel	-
	$d_p = 3.2, 6.4$ mm	$d_p = 1.75$ mm
Liquid viscosity	0.99 Pa.s	4.5 mPa.s
	1.25 Pa.s	-
	$h_L \approx 250$ μm	$h_L = 200$ to 1000 μm
Substrate	Polished Quartz	hardened tool steel
Velocity	-	2.36 m/s
Gap Reynolds number	$Re_{gap} < 1$ (0.58, 0.46)	$50 < Re_{gap} < 200$
Stokes number	0-25	106

Stokes number. The model does not state any limitation and hence should be able to perform well under different conditions. However, in their experiments, Antonyuk et al. [7] vary the liquid height and hence Re_{gap} keeping other parameters constant. As the experimental conditions are completely different for model 1 and 2, any comparison made on experimental data will be quite elusive.

Comparing the equations of model 1 and 2, it can be readily observed that model 2 provides a detailed description of all the forces acting on the particle during different phases. However, model 1 considers only two factors: viscous dissipation during penetration and the energy loss due to contact between the particle and the substrate. The energy dissipated in the liquid layer is a dominant parameter. Model 1 considers that the viscous force begins to act when the particle has entered one third of the liquid layer thickness. However, model 2 approximates the onset of viscous forces when the particle has penetrated a distance equal to 1% of the particle diameter. Further, as discussed earlier, model 2 considers different forms of equations for viscous dissipation based on particle position in the liquid layer.

As a first step towards understanding the applicability and limitations of the models, a comprehensive numerical code was developed to simulate the impactation of a particle over a liquid coated substrate according to model 1 and model 2. Model 2 requires detailed calculation of different forces based on the kinematic motion of the particle (eq. 2.35). The equations were solved using an Euler implicit integration scheme. A time step of 10^{-7} was used for stability and proper temporal resolution. The results obtained from the present numerical solutions were compared with that of the models 1 and 2. The result for model 1 is shown in figure 2.7 and the comparison of the present numerical calculation with Antonyuk et al. [7] (model 2) is shown in table 2.2. The result of the current simulation matched well with that of Model 1. However, small differences were observed in the contribution of the dif-

ferent mechanisms for model 2. The reason for this can be attributed to the possible difference in the numerical schemes and the time steps used by Antonyuk et al. [7] and in the present numerical calculations. The experimental parameters correspond-

Table 2.2: Comparison of present numerical results to the numerical results of Antonyuk et al. [7]. The contribution is shown for the various forces for the impact of a $\gamma\text{Al}_2\text{O}_3$ particle over a liquid layer ($\mu = 4.5 \text{ mPa}\cdot\text{s}$) impacting normally at 2.36 m/s

Contribution	Antonyuk et al. [7]	Present calculation
Q_{vis}	56.4%	57.4%
Q_c	26.9%	26.11%
Q_D	12.4%	13.1%
Q_t	4.7%	4.2 %
Q_{cap}	-1.15%	-1.46%
Q_{mg}	0.75%	0.65%
$Q_{diss,tot}$	100%	100%

ing to model 1 (as listed in table 2.2) was used as input data to evaluate model 2. The prediction of model 2 as compared to model 1 is shown in figure 2.11. Although model 1 predicts a rebound beyond $\text{Stk} = 6$, Model 2 does not predict rebound up to $\text{Stk} = 16$ and the differences between the restitution coefficients are quite large. In a similar way, the experimental data corresponding to model 2 was used to evaluate the prediction of model 1. For increasing liquid layer thickness, it is seen that model 2 predicts lower restitution coefficients. However, model 1 does not show much deviation in the restitution coefficient for various liquid layer thicknesses. As the predictions of the models are different, it is important to evaluate the importance of gap Reynolds numbers and Stokes numbers for varying liquid viscosities and layer thicknesses.

2.4.4 Modifications to model 2

The equations used in Antonyuk et al. [7] for the energy dissipated in the contact phase assumes a constant restitution coefficient. However, as shown earlier (figure 2.4), the restitution coefficient varies for different impact velocities. Further, the elastic parameter used in model 1 has to be determined using compression tests. Model 1 was modified by incorporating the Rogers and Reed [44] model for the contact phase. This allows one to calculate the restitution coefficient which varies with the impact velocity and also to use material properties (which are readily available for standard materials) rather than the elastic parameter which has to be experimentally evaluated. Further, the buoyancy term (equation 2.37) was found to be inconsistent and was modified to $F_b = (1/3)\pi x^2(3r_p - x)$. Similarly, the area of the spherical cap

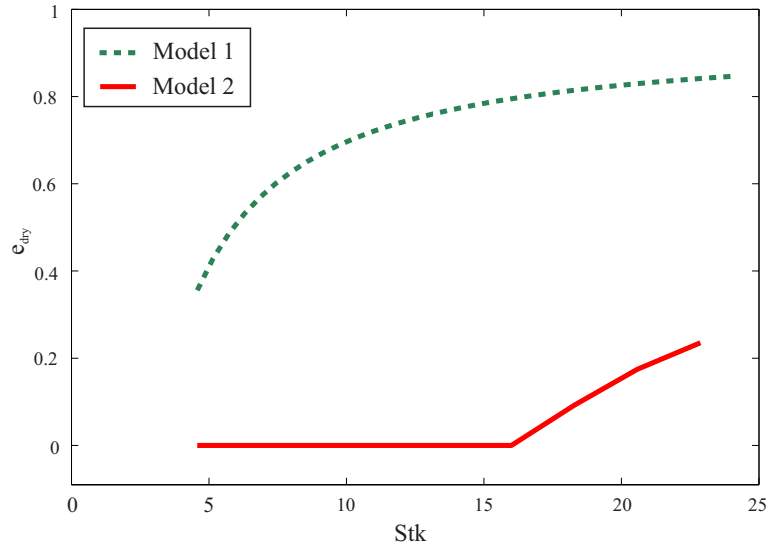


Figure 2.11: Performance of the models for experimental data of model 1 ($r_p = 3.2 \text{ mm}$, $\rho_{nylon} = 1140$, $\mu_L = 0.99 \text{ Pa}\cdot\text{s}$, $h_L = 80 \mu\text{m}$, $v_{i,n} = 2 \text{ to } 30 \text{ m/s}$).

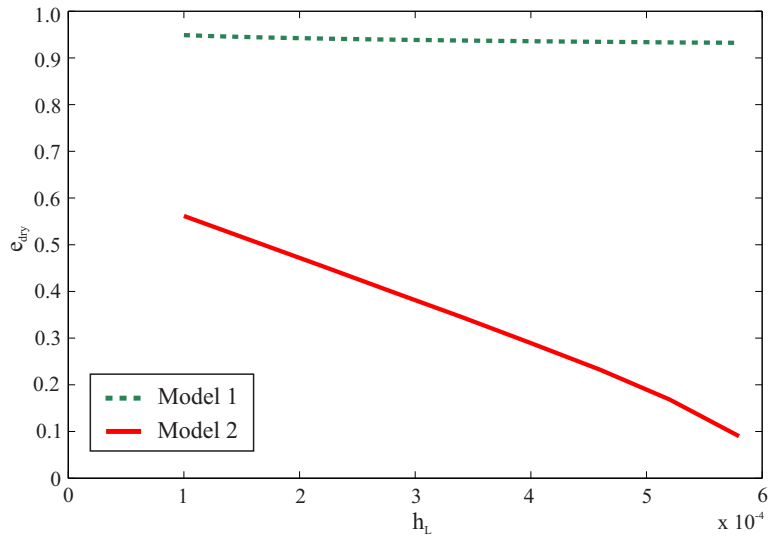


Figure 2.12: Performance of the models for experimental data of model 2 ($r_p = 0.875 \text{ mm}$, $\rho_{Al_2O_3} = 1040$, $\mu_L = 4.5 \text{ mPa}\cdot\text{s}$, $v_{i,n} = 2.36 \text{ m/s}$, $h_L = 80 \text{ to } 580 \mu\text{m}$).

used in the drag force was changed to $A = 2\pi r_p x$ instead of $A = 0.25\pi d_p^2 \sin^2(\alpha)$. Figure 2.13 shows the energy dissipated by the various mechanisms using the modified

equations for similar conditions as reported by Antonyuk et al. [7]. A 3% increase in the drag force was observed and a 5% reduction in the contact phase is observed.

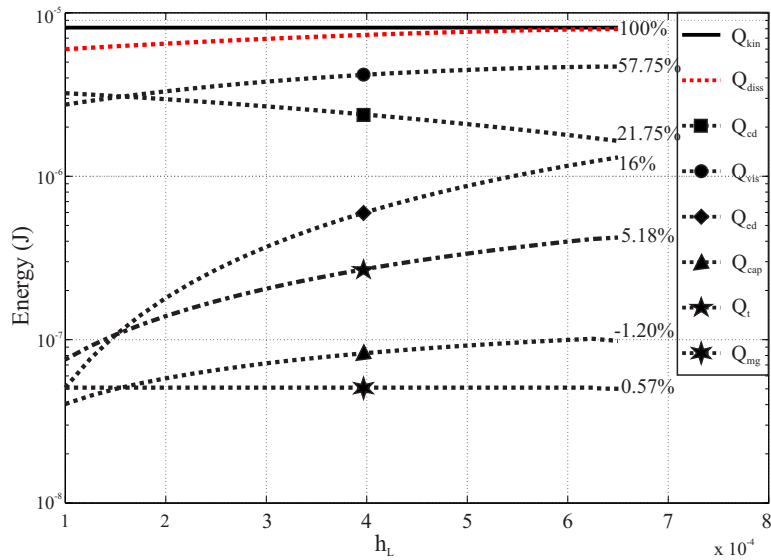


Figure 2.13: Contribution of different forces in the energy dissipation of the particle for varying liquid layer thickness . Evaluated according to modified model of Antonyuk et al. [7].

2.5 Conclusions

The simultaneous action of several interacting mechanisms coupled with numerous particles interacting at the same time renders the difficulty in numerical modeling of particle deposition process. Depending on the heat exchanger section in question, different modeling approaches are adopted. For slagging conditions, the critical viscosity approach has been used. For biomass related applications, the melt fraction approach has been used to understand the deposition process in heat exchanger regions where condensation occurs. However, for application involving dry particles or for heat exchanger regions with partial condensation, the critical velocity approach provides a means to evaluate the sticking, rebound, and removal processes in a detailed fashion. Based on the literature survey, it can be concluded that the impaction of dry particles on dry surfaces has been studied by many researchers and the subject matter is well documented with both theory and experimental evidence.

Contrary to dry impaction, information related to impaction of particles on a substrate with an interstitial viscous liquid in between is very limited and has not been established well. A detailed literature survey was conducted to study the physics

associated with particle impacting on a liquid coated surface. The models of Davis et al. [23] and Antonyuk et al. [7] were studied in detail, and the models were incorporated in a numerical scheme. The models were evaluated against each other and it was found that they had limited applicability. The model proposed by Davis et al. [23] was found to be valid for cases when the gap Reynolds number was less than unity. Further, experiments involving impacts that extend beyond the elastic limit of the particle (i.e plastic deformation) have not been reported. Model 2, proposed by Antonyuk et al. [7] provides detailed analysis of the various forces acting on the particle and the eventual energy dissipated by the particle in the complete process of impact and rebound. However, the model was validated with a liquid of very low viscosity as compared to the high viscosity liquid used to validate model 1. The models were found to be valid for a certain Stokes and Reynolds number. In order to evaluate the models in detail, experimental data is necessary which covers a wide range of Stokes and gap Reynolds numbers which can aid in better understanding of the process.

Experiments on particle impaction over liquid coated substrates

Experiments were performed for particles impacting liquid coated substrates for a range of Stokes and Reynolds numbers. The models discussed in the previous chapter were compared to the experimental results of wet coefficient of restitution. Further, a new experimental approach was adopted to evaluate the energy dissipated in the viscous layer for different Stokes numbers. The experimental methodology and the results are presented.

3.1 Experimental methods

In the present experimental work, three different categories of experiments were performed. In the first type, the process of wet impaction was observed with a high speed camera by setting the field of view close to the particle-liquid-surface interaction region. The second category of experiments correspond to the measurement of the impact and rebound velocities of particles to compare with the models discussed in the previous chapter. A third variety of experiments were performed to evaluate the energy expended by the particle in the viscous liquid layer. The schematic of the experimental setup used to perform drop experiments is shown in figure 3.1. It mainly consists of: a particle dropping head, target material (substrate) and recording camera along with corresponding lighting system.

Based on the particle size, two different types of dropping heads were used. Par-

ticles in the range 1.5 to 5 mm were dropped using a perforated disc in a housing. The perforated disc when slowly rotated allows the particle to fall freely on the target at the same spot each time. Care was taken to turn the disc slowly, so that the ball does not rotate while dropping down.

A thick plate with reamed holes were used to drop bigger particles. The holes were provided with a side screw which held the particle in position in the hole, by loosening the screw, the particles were dropped from its position. The particles were marked with a ink dot to observe particle rotation, and the rotation observed was found to be negligible. The dropping head can be positioned at different heights and the particle impact velocity was based on the particle dropping height.

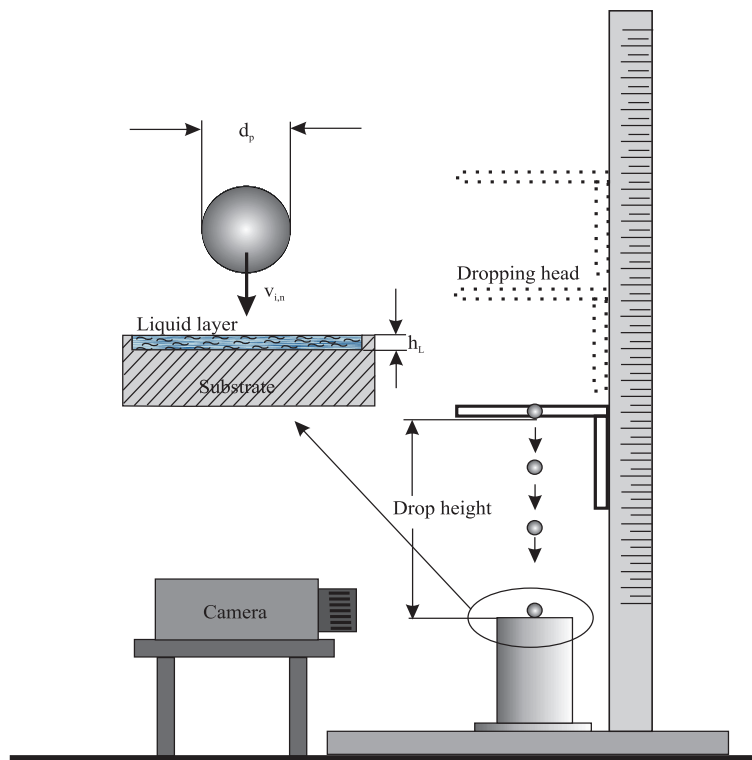


Figure 3.1: Schematic of free fall impaction experimental setup.

The substrates were thick, having a diameter of 80 mm and a thickness of 40 mm. This was to avoid elastic wave propagation and vibration effects due to the impaction process. A recessed pocket was provided on the top to act as a liquid reservoir as shown in figure 3.1. The depth of the pocket ranged from 100 μm to 2000 μm which corresponds to the liquid layer thickness. The surface of the pocket was made smooth with emery paper and polished with a diamond paste to get a

smooth surface. Roughness measurements of the surface were done and resulted in an average roughness value in the range 0.2 to 1.5 μm (RMS value).

The viscosity of each liquid was measured before each experiment with a Rheometer [Rheometric Scientific TM ARES]. An assortment of liquids with different viscosities were chosen to achieve a wide range of gap Reynolds numbers and Stokes numbers. The viscosity measurements indicated a linear relationship between the shear rates applied and the shear stress (i.e. Newtonian liquids were used). The viscosity and density values of the liquids are provided later.

To get a closer look into the wet impaction process, larger particles were used in conjunction with a high speed camera [Phantom V7]. The trajectory of a particle was observed as a shadow using a Light Emitting Diode (LED) light source with a diffuser plate in between the particle and the light source. The use of a LED light source avoids heating of the liquid layer and thus the viscosity of the liquid layer remained unchanged during the experiments. Although, high speed recording provides all the necessary information required to evaluate the impaction process, the system cannot be used for particles which bounces off beyond the focal area. The camera recording rate, lens system and the image resolution are closely interlinked and these pose a limitation to the extent to which the high speed recording can be used.

In order to measure the incident and rebound velocities of smaller particles in the range of 2 to 5 μm , a camera [Kodak ES 1 @ 30 Hz recording rate, Navitar CCTV lens 25mm, f1.4, Res: 1008 x 1018 pixels] along with a LASER was used. The beam of the continuous argon laser [Spectra physics- Stabilite 2017-AR] was converted into a pulsating light sheet using an optical chopper and a combination of cylindrical lenses. The use of two lenses provided a thicker light sheet [4 mm] which is necessary to capture the particle path. The combination of pulsated laser sheet and comparatively lower recording rate of the camera resulted in images of particle trajectories as light streaks, as shown in figure 3.2. The particle velocity can be evaluated by measuring the length of the light streak. Further details of this recording method can be found elsewhere [1, 62] and is not dealt here.

In some of the experiments which will be discussed later on, it was necessary to measure the hardness of the substrate and the volume of the indentation (crater) formed on the substrate due to impaction. The hardness measurements were performed with a CSM micro indenter hardness testing equipment. The surface roughness, crater depth and diameter was measured with a [Sensofar PL μ 2300] profilometer. The image inlaid in figure 3.3 shows a typical profilometer image of the crater formed and the plot shows the center cross sectional data. The crater diameter was evaluated in two mutually perpendicular directions and both measurements were found to be within 2-5% with each other. The larger dimension was however used for the analysis.

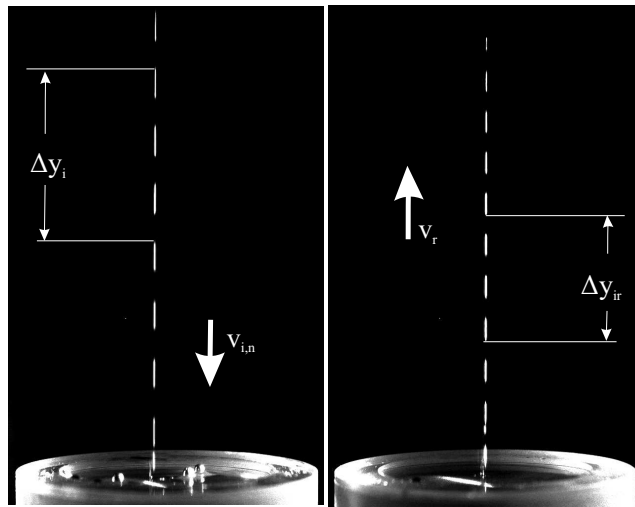


Figure 3.2: Typical image recorded by the camera of a particle displacement: (a) before impact and (b) after impact (rebound).

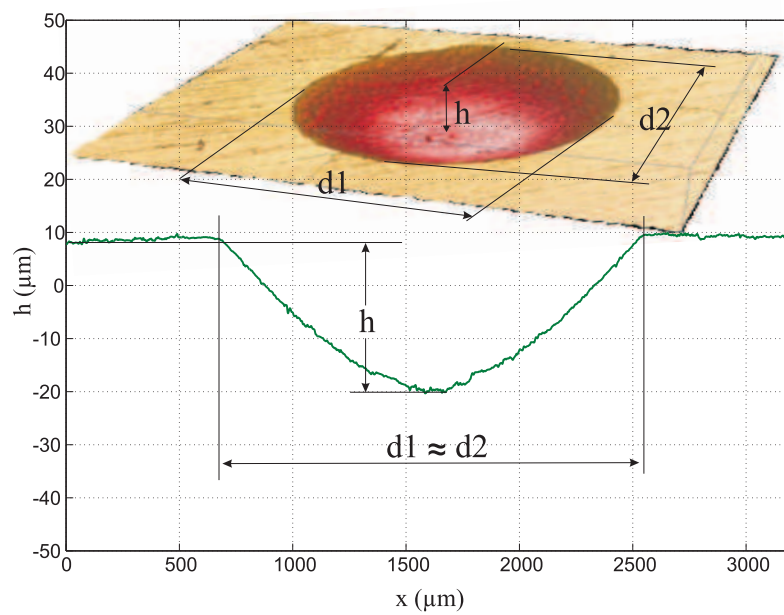


Figure 3.3: Typical image of profilometer measurement of crater diameter and depth at the center plane. The inlaid graphical image shows a typical image of the crater obtained by the profilometer.

3.2 Physical description of the wet impaction process

Figure 3.4 shows the recorded images of a particle: (a) just before contact with the liquid layer, (b) during penetration, (c) during the liquid bridge formation and (d) at maximum height to which the particle rebounds, using a high speed camera. Based on the process description of Antonyuk et al. [7] and critical observations during and after the experiments, the overall impaction and rebound process of the particle over a liquid film can be described as follows:

- Phase 1: This is the duration between which the particle comes in contact with the liquid layer and travels through the liquid layer until it comes in contact with the rigid planar surface of the substrate. The liquid forms a spherical cap over the particle and as the particle penetrates the liquid layer, a high pressure region is created in between the particle and the substrate. This high pressure region however is localized and due to the pressure gradient, the liquid is squeezed out at high shear rates. A crown forming phenomena can be clearly observed for liquids of lower viscosity as seen in figure 3.4 (b). Liquids of higher viscosity do not display crown formation as the intermolecular forces are quite large as compared to lower viscosity liquids. As the gap between the particle and the substrate becomes very small, based on the surface roughness of the interacting surfaces, the impact can result in a direct physical contact between the particle and the substrate which can lead to plastic deformation. McLaughlin [40] performed impaction experiments where the particle

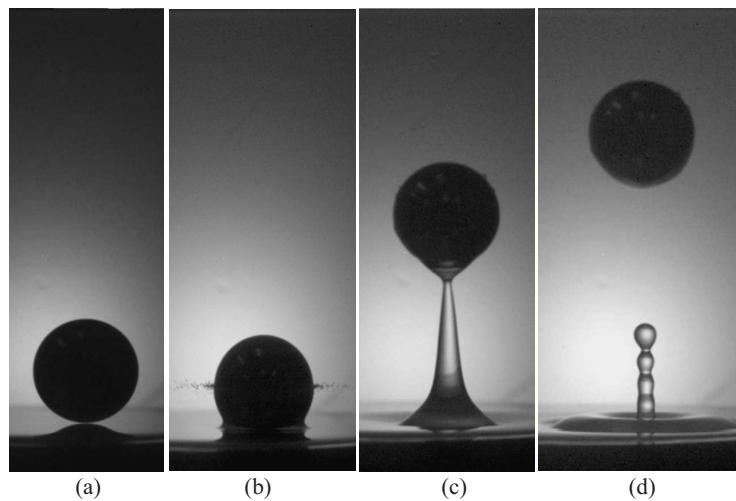


Figure 3.4: Typical recorded images (a) before impaction, (b) during crown formation, (c) during liquid bridge formation (d) at maximum rebound height.

was completely immersed in a liquid and observed that the velocity of the particle sharply reduces when the particle is very close to the flat surface, suggesting that most of the energy loss occurs over small liquid layer thickness. In the present experimental observations, it was observed that the particle velocity is considerably reduced when the particle is at a distance approximately 15-20% of particle radius. According to equation 2.22, the net force exerted on the particle by the fluid increases infinitely as the gap between the particle and the surface tends to zero. Equation 2.22 for the viscous force is derived assuming 'hydrodynamically' smooth surfaces. Thus, in reality, if the surfaces are hydrodynamically smooth, a physical contact should never occur.

Clark [18, 19] have observed plastic deformations in their erosion tests and the post experimental observation of the substrate in the present work also indicated plastic deformations. Eirich and Tabor [26] in their model similar to a fall-hammer experiment, suggest that for heavy impacts, the pressure developed in the liquid film are sufficient to deform the surfaces either elastically or even plastically in the course of the collision process. Gee et al. [29] suggest that under the compression due to collision, the liquid in the gap solidifies for a brief period of time and thus transmits the pressure between the surfaces without physical contact. Further, in most practical applications, the surfaces are always associated with a certain degree of surface roughness. The peak-valley structure on the surface comes into contact before the viscous force becomes infinitely large. The concept of pressure transmission through the liquid layer and the effect of surface roughness is schematically shown in figure 3.5. Thus, it can be concluded that the particle and substrate experience the pressure created due to impact either by direct contact due to surface roughness, or due to pressure transmitted by the thin film. In either case, if the pressure is large enough to cause plastic deformations beyond elastic deformations, permanent deformations will be formed on the surfaces. The present study assumes no cavitation effects and negligible rise in temperature due to impaction. Further, the rotation of the particle is assumed to be negligible and only impacts at normal incidence are considered.

- Phase 2: This corresponds to the duration in which the particle is in contact with the substrate during which the substrate and the particle undergo elastic-plastic interaction.
- Phase 3: This corresponds to the period from the start of particle rebound up to the time when the particle reaches its maximum height. During this period, based on the viscosity, layer height and particle velocity, a liquid bridge connecting the particle and the liquid layer forms due to inverse pressure gradients induced while the particle rebounds. Figure 3.4 (c) shows the liquid bridge formation and the image represents the pinch off point where the liquid

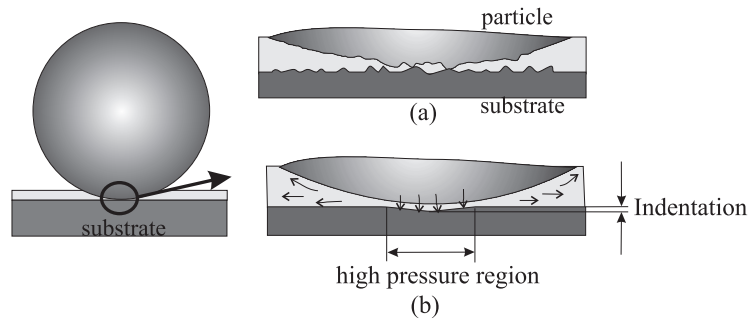


Figure 3.5: Schematic representation of possible modes of plastic deformation. (a) Deformation caused by direct contact between the surfaces due to roughness, (b) Deformation due to pressure transmission between interacting surfaces through a thin film of liquid.

bridge is about to be detached. For lower viscosity liquids, the liquid bridge ruptures quickly in accordance with the Savart-Raleigh- Plateau instability criteria as shown in figure 3.6 (a). For liquids of higher viscosity, the length of the liquid bridge is considerably longer and a typical bead formation is observed as in figure 3.6 (b). A certain amount of energy will be dissipated in the formation and the rupture of the liquid bridge and results in a lower rebound height as compared to the dry rebound with similar initial rebound velocity and for lower viscosity liquids. The particle reaches to a maximum height where all of its kinetic energy is transformed to potential energy and drops down again.

3.3 Comparison of models with experimental data

As discussed in the previous chapter, it was difficult to evaluate the available models for wet impaction. It is necessary to perform experiments similar to the one that have been reported, but for varying gap Reynolds numbers and Stokes numbers. Brass particles in the range of 2 to 5 mm in diameter were dropped on a glass substrates coated with liquids. By varying the liquid layer viscosity, layer thickness and drop height, a range of Stokes numbers and Reynolds numbers were achieved. Table 3.1 lists the viscosity (measured value) and density (manufacturer data) values of the liquids used in the experiments. As seen from the table, a wide range of viscosity values are chosen. The material properties of the substrate and the particles are listed in table 3.2.

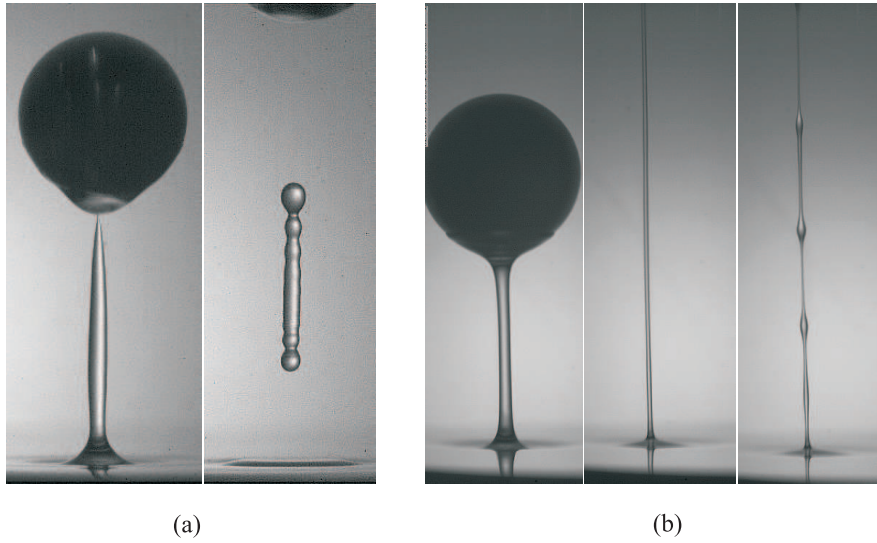


Figure 3.6: Liquid bridge formation and rupture for (a) low viscosity liquid (1 mPa.s), (b) high viscosity liquid (1 Pa.s).

Table 3.1: Properties of the liquids used in the experiments

Liquid	Dynamic viscosity (Pa.s) $\pm 3\%$	Density (kg/m^3)
Oil 1	$\mu_1 = 0.6978$	$\rho_1 = 894$
Oil 2	$\mu_2 = 0.102$	$\rho_2 = 887$
Oil 3	$\mu_3 = 0.0176$	$\rho_3 = 881$

Table 3.2: Properties of the substrate and particles

Substrate	Particle
material: Glass	material: Brass
Young's Modulus, $E = 64 \text{ GNm}^{-2}$	Young's Modulus, $E = 110 \text{ GNm}^{-2}$
Poisson's ratio, $\nu = 0.27$	Poisson's ratio, $\nu = 0.34$
density, $\rho_p = 2470 \text{ kgm}^{-3}$	density, $\rho_p = 8450 \text{ kgm}^{-3}$
surface roughness, $R_a = 0.1 \mu\text{m}$	surface roughness, $R_a = 0.1 \mu\text{m}$
	yield strength = 390 MNm^{-2}

Particle rebound characteristics for Stokes numbers in the range of 3 to 18

Figure 3.7 (a) shows the wet coefficient of restitution of the particle impacting a layer of Oil 1. The Stokes and Reynolds numbers are somewhat larger than the values

corresponding to model 1 of Davis et al. [23], but are of the same order and are comparable. The variation of gap Reynolds number and corresponding Stokes number for different conditions are shown in figure 3.7. The lowest gap Reynolds number is between 1.56 and 6 and the highest value is about 12. The critical Stokes number beyond which the particle rebounds is found to vary between 5 to 9. This value is however dependent on the resolution of the recording system and the way a 'rebound' is defined. In the high speed recordings discussed earlier, it was observed that although the particles do change their direction of motion and "rebound", they sometimes do not emerge completely out of the liquid layer. In the present analysis, particles which rebound at least to a height greater than the diameter of the particle are considered to be rebounded. For increasing liquid layer thickness, the critical Stokes number was found to be correspondingly higher. Lower values of Stokes number indicates higher viscous resistance to the particle motion and thus, a major part of the particle kinetic energy is dissipated in the liquid layer and the particle does not rebound. The particle inertia is completely balanced by the viscous forces for Stokes equal to unity. However, if a particle has to rebound, it must possess sufficient energy to overcome all the forces which acts against its motion. For higher Stokes numbers, the particle shows an increasing trend in the values of restitution coefficient for a given liquid layer thickness indicating a diminishing effect of viscous forces. At a given Stokes number, the restitution coefficient reduces with increasing liquid layer thickness indicating the importance of gap Reynolds numbers at lower Stokes numbers.

The predictions of model 1 and 2 are also shown in figure 3.7 (a). Model 1 predicts the critical Stokes number and the trend for the restitution coefficient for varying Stokes numbers quite well. This is however valid for a liquid layer thickness of 0.5 mm and the corresponding gap Reynolds number is between 1.5 and 4. The model over-predicts the restitution coefficients for higher gap Reynolds number (liquid layer thicknesses).

Model 2 does not predict rebound for the entire range of Stokes number shown here. The numerical simulations for model 2 requires careful attention to the surface roughness values. The surface roughness values of the substrate were measured (and found to be in the range of 0.1 to 0.3 μm), however the particle surface roughness was unknown and a value of 0.2 μm was chosen for the "polished" particles that were used. The model was checked for higher roughness values and the model did not predict any rebound of the particles for the Stokes numbers values discussed above.

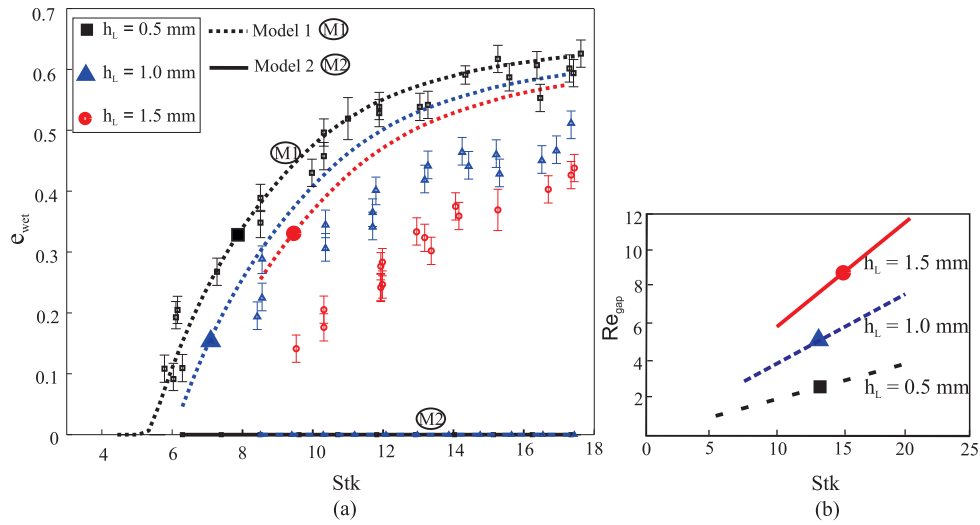


Figure 3.7: (a) Wet coefficient of restitution as a function of Stokes number for brass particles impacting a glass substrate coated with Oil 1 of three different thicknesses. Open symbols - experimental data, dotted lines with symbols - model 1, solid lines with symbols - model 2; (b) Variation of gap Reynolds number with Stokes number for Oil 1 with varying velocity and liquid layer thickness.

Particle rebound characteristics for Stokes numbers in the range of 10 to 80

Figure 3.8 shows the rebound characteristics for Oil 2. The experiments were similar to that of Oil 1. The gap Reynolds numbers are in the range of 5 to 45 and the experiments indicate that for higher Stokes numbers (> 40), the restitution coefficient flattens out. The restitution coefficients for Stokes numbers up to 70 have different values for varying liquid layer thickness. However, at higher Stokes numbers the restitution coefficients for different layer thicknesses begin to overlap each other indicating a dominating effect of particle inertia.

Model 1 qualitatively predicts the trend of the experimentally observed restitution coefficients but the model over-predicts the values. The difference in the values of restitution coefficients for varying liquid layer thickness is lower than the experimental values.

The prediction of model 2 of Antonyuk et al. [7] shows that the particles begin to rebound around Stokes number of 40 and 70 for a liquid layer of 0.5 and 1 mm respectively. However, the model does not predict any rebound for larger liquid layer thickness.

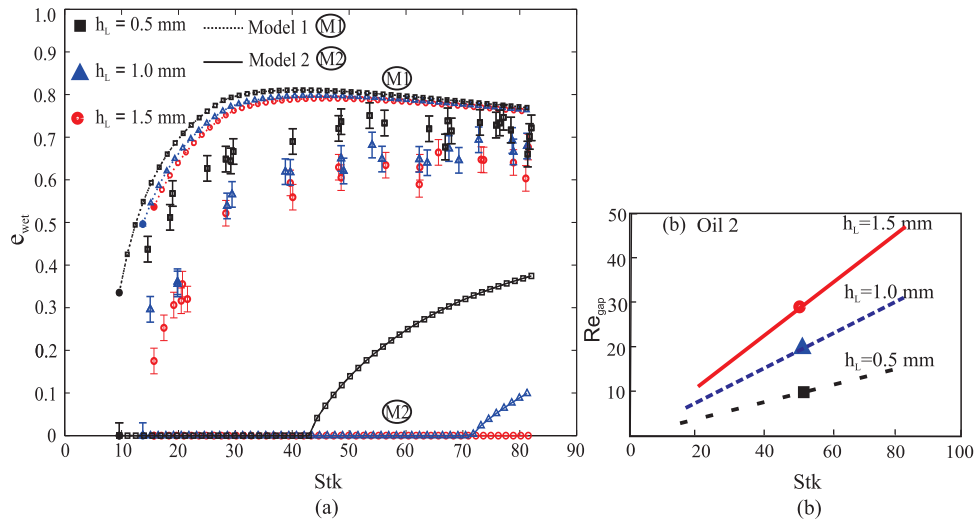


Figure 3.8: (a) Wet coefficient of restitution as a function of Stokes number for brass particles impacting a glass substrate coated with Oil 2 of three different thicknesses at different velocities. Open symbols - experimental data, dotted lines with symbols - model 1, solid lines with symbols - model 2; (b) Variation of gap Reynolds number with Stokes number for Oil 2 with varying velocity and liquid layer thickness.

Particle rebound characteristics for Stokes numbers in the range of 100 to 700

Oil 3, which has a comparatively lower viscosity than the other two liquids was used to obtain higher Stokes numbers along with higher incident velocities. The variation of the restitution coefficient is shown in figure 3.9. It is observed that the restitution coefficients for different liquid layer thickness tend to overlap each other for Stokes number beyond 200 and the values of the restitution coefficients are much higher than for the other two oils considered. The inertial effects are dominant than the viscous forces. For a liquid layer thickness of 0.5 mm, the impaction behavior was found to be similar, although with a lower restitution values of about 7-8% as compared to that of dry impaction values (based on dry experiments, data not shown). Thus, at higher Stokes numbers, the viscous effects due to the fluid is negligible and results in higher restitution coefficients similar to that of dry impaction.

Model 1 (of Davis et al. [21]) predicts a higher restitution coefficient and for different liquid layer thickness, the results of models 1 overlap each other.

Model 2 (of Antonyuk et al. [7]) predicts rebound of particles for all the three liquid layer thicknesses. However, the values of restitution coefficients are rather under predicted. The previous experiments involved liquids of higher viscosity and from

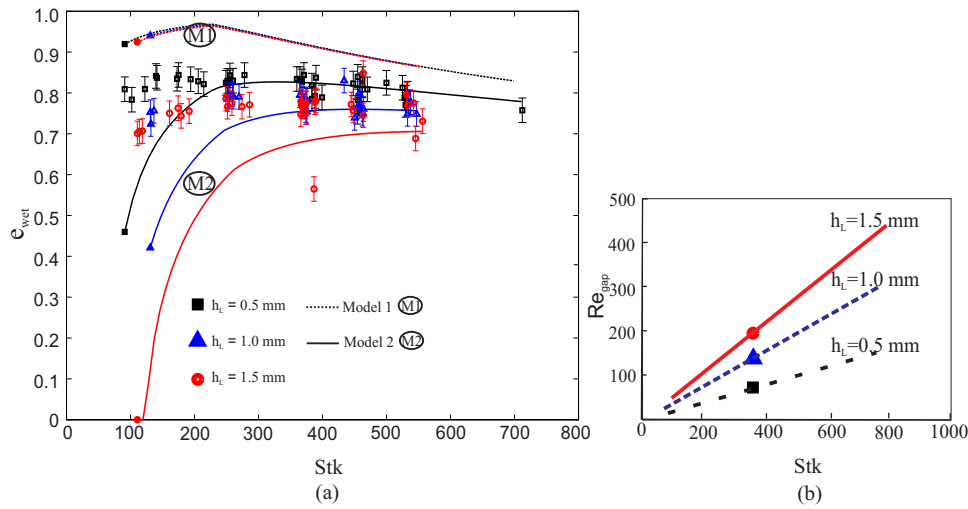


Figure 3.9: (a) Wet coefficient of restitution as a function of Stokes number for brass particles impacting a glass substrate coated with Oil 3 of three different thicknesses. Open symbols - experimental data, dotted lines with symbols - model 1, solid lines with symbols - model 2; (b) Variation of gap Reynolds number with Stokes number for Oil 3 with varying velocity and liquid layer thickness.

the numerical data of model 2, it was noted that the model over predicts the viscous dissipation term. The model also assumes a viscous force to act on the particle during the rebound phase. But for the conditions in which the particle size is larger than the liquid layer thickness, this seems not to be the case.

For impacts at lower Stokes numbers, the viscous forces are dominant and the particle loses a major part of its kinetic energy in the liquid layer. Depending on the amount of energy associated with the particle at the end of the penetration phase, the particle may contact the surface and dissipate the remaining energy which completely depends on the material properties of the particle and the surface. It was seen in all sets of experiments that, model 2 over predicted the energy that was dissipated in the liquid layer.

During particle impacts at higher Stokes numbers, a particle can penetrate the liquid layer and owing to its higher inertia, the particle-surface can undergo elastic or elastic-plastic impact. Brass particles were used in the present experiments which can display elastic-plastic impactation behavior. Few experiments were performed on copper and steel substrates, and several small indentations were observed on the substrates indicating that an elastic-plastic deformation had occurred. Model 1 basically assumes elastic impacts and the model has not been validated with experiments which involve impacts that result in loads which exceed the yield limit of the particles or substrates. A major loss of particle kinetic energy can thus be due to

viscous forces and also due to plastic deformations. Due to the lack of any published literature on the experimental or numerical results for wet impaction involving plastic deformations, a new set of experiments were carried out to quantify the energy losses in such interactions.

3.4 Energy balance for impaction involving elastic-plastic deformations

Considering a hard ball impacting a ductile substrate coated with a thin liquid film, regardless of the mode of pressure transmitted to the substrate, if the substrate undergoes plastic deformation, the energy expended in the plastic deformation can be evaluated using the principles of contact mechanics. For the present study, the model of Rogers and Reed [44] is used to evaluate the energy dissipated during the plastic deformation of the substrate.

If Q_k is the particle kinetic energy (as defined in equation 2.7), Q_{pot} is the (potential) energy associated with the particle at its highest point after rebound, Q_{liq} is the energy dissipated in the liquid layer over the whole process and Q_p represents the energy expended in the plastic deformation of the substrate, an energy balance for the process of wet impaction for normal incidence can be written as:

$$Q_k - Q_{pot} = Q_{liq} + Q_p \quad (3.1)$$

Figure 3.10 shows the particle impact and the maximum height to which the particle

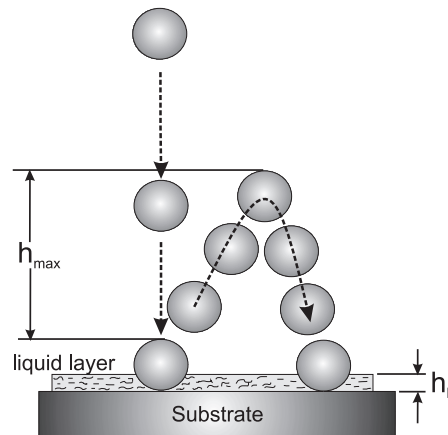


Figure 3.10: Schematic of particle impact and maximum rebound height attained by the particle post impaction.

rebounds. Q_{pot} can then be written as:

$$Q_{pot} = m_p g h_{max} \quad (3.2)$$

where g is the acceleration due to gravity and h_{max} is the maximum rebound height. Q_p represents the energy expended in the plastic flow of the substrate. By measuring the crater volume on the substrate, the energy expended in the plastic deformation can be evaluated using the concept of contact mechanics.

3.4.1 Energy dissipation in plastic deformation

The Rogers and Reed model was developed and validated for small particles (micrometer sized) undergoing elastic-plastic deformations. To evaluate the applicability of the model to larger particles, dry impactation experiments were conducted. Brass balls of 2.5 mm diameter were dropped on glass substrates and the restitution coefficient was measured using the experimental method described earlier. Figure 3.11 shows the experimental data and the numerical prediction of the Rogers and Reed model. The model predicts the dry restitution coefficient values with considerable accuracy. For higher impact velocities, it is also seen that the restitution coefficient reduces. In order to evaluate the energy expended in the plastic deformation, the crater dimensions are necessary and hence the model was also validated for crater depth and height.

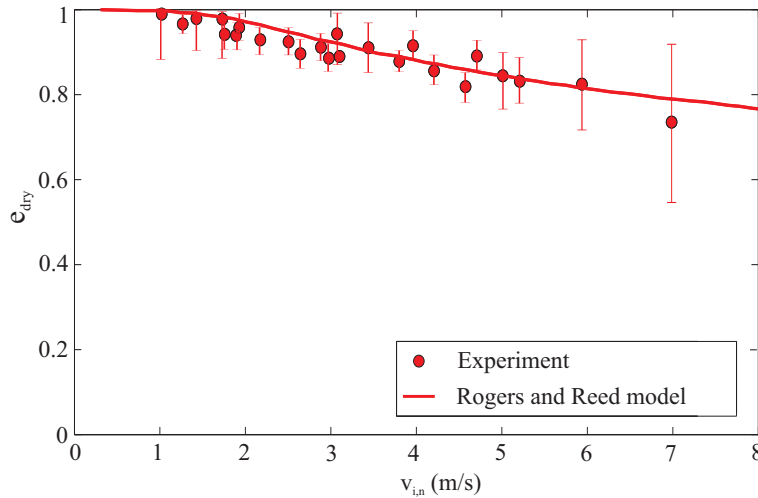


Figure 3.11: Comparison of Rogers and Reed model with experimental data for coefficient of restitution of a brass particle $d_p = 2.5$ mm impacting a glass substrate at different incident velocities.

Thirupataiah and Sundararajan [57] have reported experimental data of the rebound behavior for the impact of Tungsten Carbide balls against ductile surfaces.

The incident velocity of the ball ranged from 5.5 to 7.5 m/s. They report the nature of the elastic rebound in terms of restitution coefficient and by the size of the crater formed by the impact. By equating the kinetic energy of the particle to the energy required to form the crater, they provide an empirical expression relating the crater diameter (d_{crater}) to the particle (ball) density (ρ_{ball}) and hardness of the substrate (H_{base}) as:

$$\frac{d_{crater}}{r_{ball}} = 2.56 v_{i,n}^{0.5} \left(\frac{\rho_{ball}}{H_{base}} \right)^{\frac{1}{4}} \quad (3.3)$$

where r_{ball} is the radius of the impacting ball.

The necessary conditions for the above relation to hold good is that the deformation occurs only in the substrate, and the relaxation of the crater shape due to the release of stored energy causing the ball to rebound is such that all the relaxation occurs only in the depth direction of the crater.

The crater depth is given by the relation:

$$\frac{h_{crater}}{r_{ball}} = 0.82 v_{i,n} \left(\frac{\rho_{ball}}{H_{base}} \right)^{\frac{1}{2}} \quad (3.4)$$

where d_{crater} and h_{crater} are the diameter and the depth of the crater formed. H_{base} is the hardness of the substrate (Meyers hardness in Pa). A ball (of ball bearing) was dropped from a known height on a polished Aluminum surface. The diameter of the ball was $d_{ball}=15.88$ mm and the mass was $m_p = 16.316$ g (± 2 mg) (measured using calibrated precision weighing machine with a least count of 1 mg). The hardness of the Aluminum specimen was measured and was found to have a mean value of 1212.4 MPa with a standard deviation of 24.3.

The comparison of experimental observations with both approaches for the crater depth and crater diameter is shown in figure 3.12 and 3.13 respectively. The empirical model of Thirupataiah and Sundararajan [57] predicts the crater depth and diameter reasonably well. The model of Rogers and Reed [44] fits well for crater depth and diameter even for the impaction of bigger particles, thus validating the applicability for the interaction of larger particles.

3.4.2 Wet elastic collisions

Experimental observations using a high speed camera had earlier indicated that when the liquid layer thickness is less than half of the particle radius, most of kinetic energy of the particle is dissipated when the particle is very close to the surface. However, experiments were conducted for various Stokes and gap Reynolds numbers to obtain an energy balance for a wide range of parameters. In the following discussions, experimental results are discussed mainly based on the Stokes number. Experiments were carried out with glass and steel particles impacting on glass

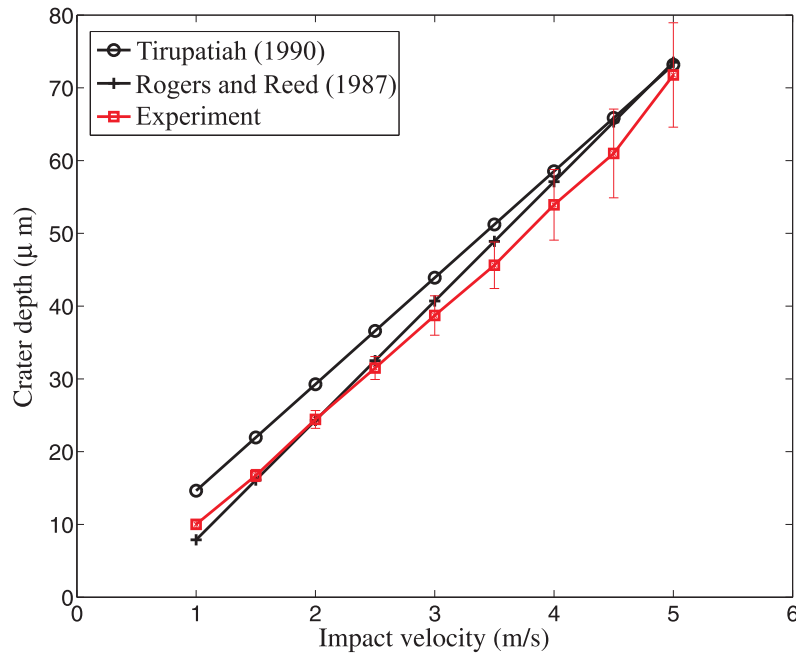


Figure 3.12: Comparison of empirical model and Rogers and Reed model with experimental data for the indentation depth of a 16 mm steel ball impacting a polished aluminum surface at normal incidence.

substrates coated with liquid film of varying viscosity and thickness. Before the experiments, prior calculations were done using the model of Rogers and Reed [44] to choose the experimental conditions such that the impactation always resulted in only elastic collisions. The liquid layer thickness was held constant and for varying liquid viscosity and particle impact velocity, a range of Stokes and gap Reynolds numbers was achieved. As there is no energy dissipated in plastic deformation, the term Q_p in equation 3.1 is zero. The process of impact and the maximum height to which the particle rebounds after impactation is recorded with a high speed camera. The field of view of the camera, accuracy and available materials imposed limitations on the extent to which experiments could be performed.

Experiments were conducted up to a Stokes number of 255 and the energy balance for the process is shown in figure 3.14 along with the inlaid plot for the variation of gap Reynolds number. A critical Stokes number beyond which a particle begins to rebound from the surface was found to be 4. Beyond the critical Stokes number, the energy dissipated in the liquid decreases monotonically up to a Stokes number of about 100, beyond which it flattens out indicating a constant dissipation of energy

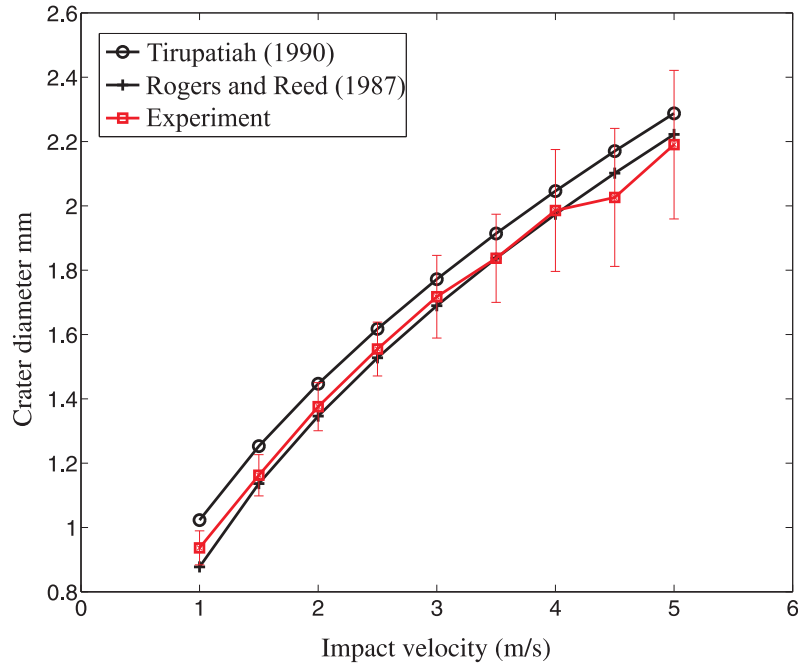


Figure 3.13: Comparison of Rogers and Reed model with experimental data for indentation diameter of a 16 mm steel ball impacting a polished aluminum surface at normal incidence.

by the liquid layer which is almost 50% of the incoming particle kinetic energy.

3.4.3 Elastic-plastic collisions

Experiments were performed with hardened steel balls (Ball bearing) impacting on Copper and Aluminum substrates coated with lubricating oils, water, glycerol and a range of mixtures of water and glycerol. Keeping the incident velocity and the liquid layer thickness constant, experiments were performed for varying gap Reynolds numbers by changing the liquid layer in order to understand the influence of liquid layer thickness. Figure 3.15 shows the energy balance for different incident velocities. The last data points corresponding to the highest gap Reynolds number correspond to the experiments that were performed with distilled water. The energy dissipated in the plastic deformation is more than the potential energy at maximum rebound height. The viscous dissipation by the liquid layer is maximum for lowest gap Reynolds number and decreases monotonically up to a value of around 100. For $Re_{gap} \geq 100$, the viscous dissipation is almost constant at 50% of the particle incident kinetic energy. A similar trend is observed in the experiments conducted for all

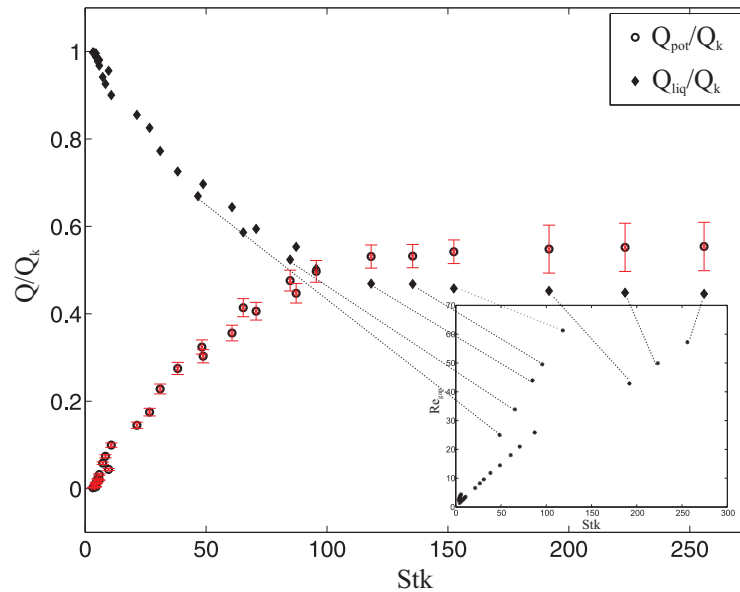


Figure 3.14: Energy balance for purely elastic wet impaction of glass and steel particles over glass substrate coated with different liquids and liquid layer thicknesses. The variation of Re_{gap} with Stk is shown in the inner plot. The liquid layer thickness was held constant and variation in Re_{gap} with Stk is due to changes in the liquid viscosity and the particle impact velocity.

velocities (1.5, 2, 2.5 and 3 m/s). Figure 3.16 shows the energy budget for varying Stokes number. Experiments were performed with varying particle diameter, liquid layer thickness and viscosity. A critical Stokes number of 5 was observed beyond which the particle begins to rebound. The energy dissipated in the viscous liquid layer is considerably high for lower Stokes number. For $Stk = 100$, almost half of the initial particle kinetic energy is dissipated in the liquid layer. For higher Stokes numbers a maximum of about 50 to 60% of the initial kinetic energy is lost in the viscous layer. The behavior at higher Stokes number indicates an increase in the amount of viscous dissipation ($Stk > 10000$). However, this can be attributed to the experimental errors caused due to dropping of particle from higher positions. The process can be visualized in terms of three regions of Stokes numbers depending on the impaction behavior. The first region corresponds to $0 < Stk < Stk_{cr}$ where all of the particle kinetic energy is dissipated in the liquid layer. In the second region ($Stk_{cr} < Stk < Stk_{max}$) the viscous effect gradually reduces as the particle inertia increases. A third region can be observed where the effect of viscous layer is constant.

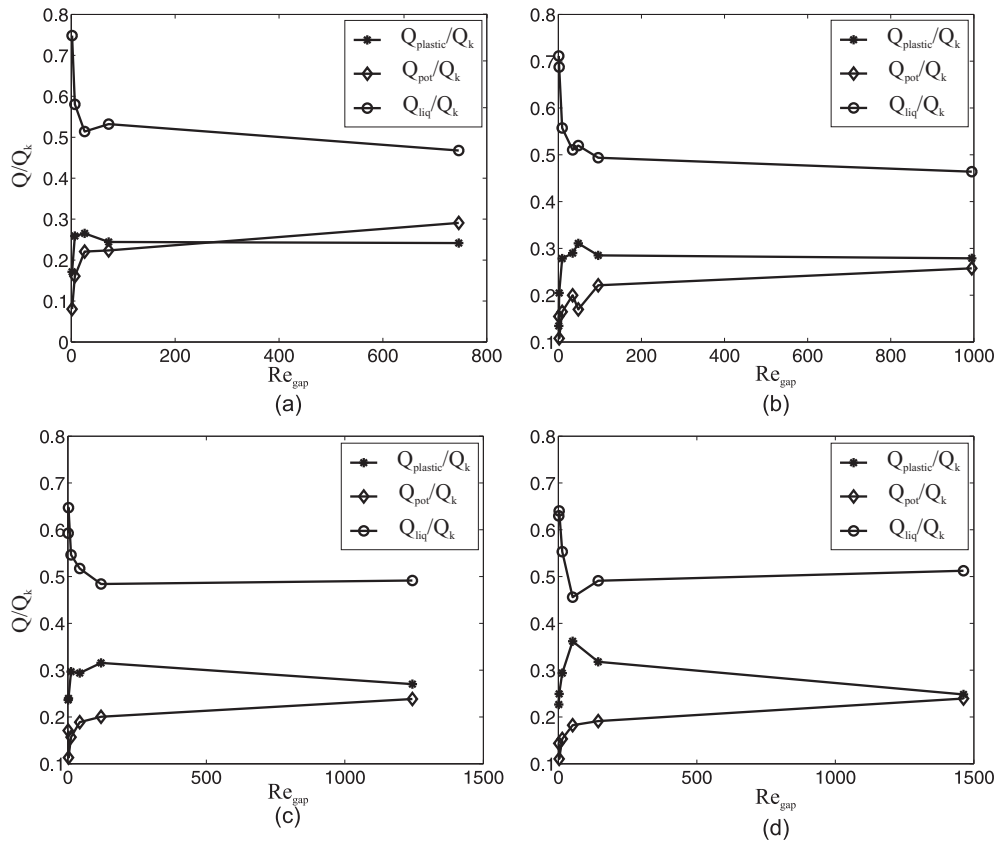


Figure 3.15: Energy balance for wet impaction with elastic-plastic deformation for different gap Reynolds numbers (constant $h_l = 1$ mm) (a) $v_{i,n} = 1.5$ m/s (b) $v_{i,n} = 2.0$ m/s (c) $v_{i,n} = 2.5$ m/s (d) $v_{i,n} = 3.0$ m/s .

3.4.4 Comparison of elastic and elastic-plastic collisions

Figure 3.17 shows the energy dissipated in the liquid layer during normal impaction of a particle on a liquid coated substrate. The number of data points of elastic-plastic impaction are reduced to aid in comparison. Elastic-plastic impacts have a steeper gradient as compared to the purely elastic case. This could be as a result of simultaneous deformation of the soft substrate due to the pressure transmitted by the liquid layer while the particle penetrates. The variation in the trends can be partly due to the fact that the surface properties of the materials used were different. For elastic collisions, glass and steel particles collided on a polished glass surface. The surface roughness of the polished glass surface is much lower than that of Copper or Aluminum substrates used in the elastic plastic deformation case. As mentioned earlier,

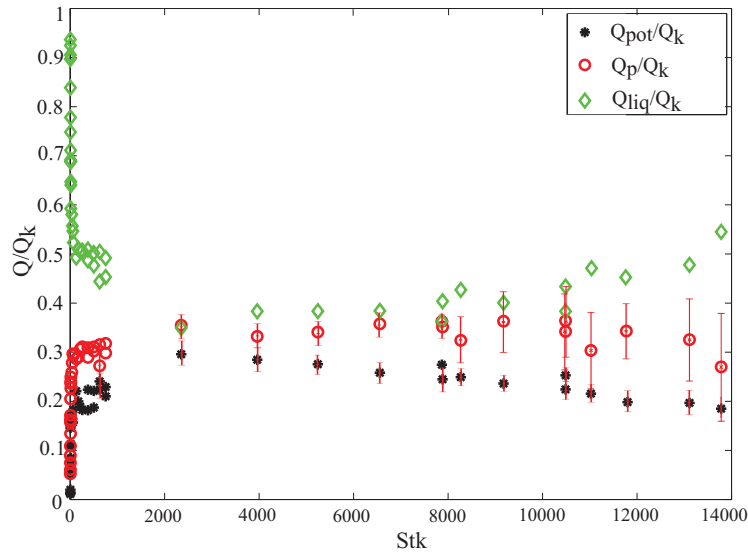


Figure 3.16: Energy balance for wet impactation with elastic-plastic deformation.

a particle comes into physical contact with a rough surface at a much early stage than for a smooth surface. Though the viscous resistance for particle motion is higher for smooth surfaces, the plastic deformation effects come into play and dominate the process. Though the initial trend is different for purely elastic and elastic-plastic deformation cases up to $Stk = 100$, the amount of energy dissipated in both situations are of the same order and are comparable for higher Stokes numbers.

Coefficient of restitution

The coefficient of restitution is a measure of the total energy dissipated in the process of impactation. In the present analysis, the restitution coefficient was measured by processing the images acquired by the high speed camera. Further, as a consequence of the energy balance of the process described by equation 3.1, the coefficient of restitution can be evaluated. The comparison of the restitution coefficients obtained by image processing and the indirectly measured values are shown in figure 3.18. The measured values (image processing) and calculated values (equation 2.34) are found to be in agreement with each other. However, a small difference in the values are observed which are below $\pm 5\%$ of each other. The small difference in restitution coefficients can be due to the following reasons:

- The particle begins to rebound at a higher velocity soon after the contact phase and the viscous forces acting on the particle during the rebound process gradually decelerates the particle. To evaluate the rebound velocity, the images are

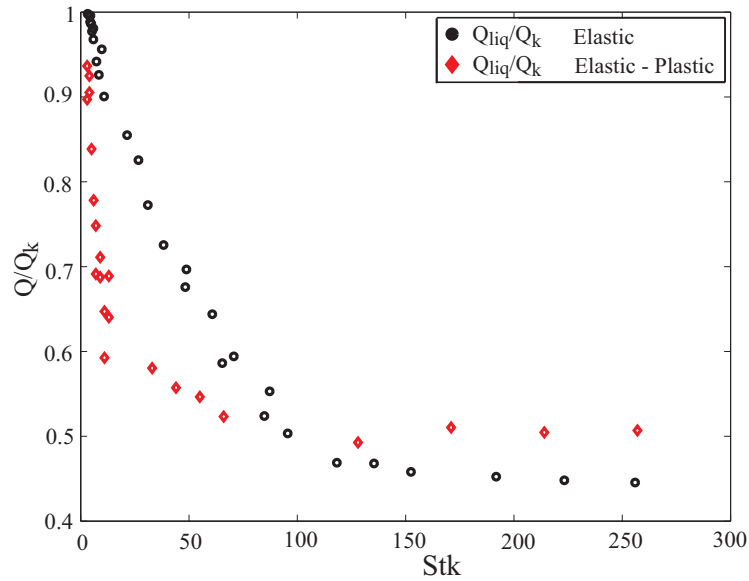


Figure 3.17: Energy dissipated in the liquid layer for elastic and elastic-plastic collisions.

processed as soon as the particle begins to rebound. However, the maximum height to which the particle rebounds is measured to evaluate viscous dissipation. Thus, the difference might actually reflect the energy being lost during the liquid bridge formation and rupture. But a detailed analysis on this was not done.

- The difference can be a direct result of the experimental errors.

In either case of possible reason for the difference in the restitution coefficient, as the difference is less than $\pm 5\%$, it can be concluded that these measurements indirectly validate the methodology used to evaluate the energy lost in the viscous layer.

3.5 Conclusions

To evaluate the particle impaction models for a liquid coated surface, an experimental setup was constructed to perform impaction experiments. Experiments were performed with different liquids, particles and substrates to obtain data for a wide range of Stokes and Reynolds numbers. It was found that model 1 predicted the onset of particle rebound comparatively well and model 2 was limited to very low viscosity liquids. Quantification of the energy dissipated in the liquid layer provides a good means to evaluate the sticking criteria. A new approach was used to quantify the energy lost in the viscous layer for purely elastic and elastic-plastic collisions.

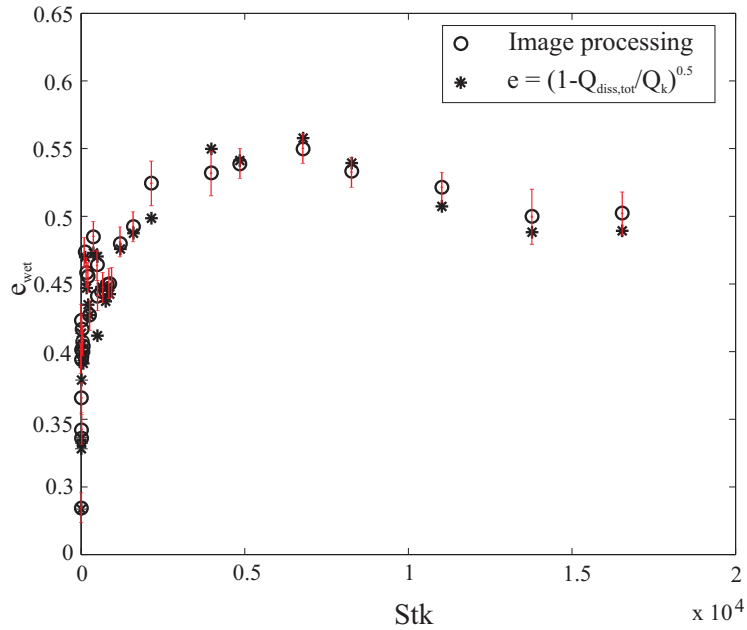


Figure 3.18: Comparison of wet restitution coefficient for directly measured values and indirectly measured values using total energy dissipated in the process.

Drop experiments were conducted with different particle sizes, substrate materials and liquids to obtain data for a wide range of gap Reynolds number and Stokes number. It was observed that most of the energy is lost for a small thickness of liquid layer and experiments done for various gap Reynolds number indicate that the energy losses were similar for different impact velocities. The experiments indicate that the particle impaction behavior can be visualized in three distinct regions based on the Stokes number. In most of the cases, a critical Stokes number was observed beyond which the particle begins to rebound and was found to be between 2 to 5. Thus a perfect sticking range can be described where the particle loses all of its kinetic energy and does not rebound $0 < Stk < Stk_{cr}$. A second region can be observed ($Stk_{cr} < Stk < 100$) for which the particle loses significant amount of energy in the viscous layer and the rebound velocity is very low. A third region beyond $Stk = 100$ exists where almost 50% of the particle kinetic energy is lost in the liquid layer. For drastically higher Stokes numbers > 5000 , the rebound characteristics of the particle is similar to dry impacts indicating minimal energy losses in the liquid layer.

The present work provides a means to quantify the energy lost in the liquid layer which is important to evaluate the particle deposition for a numerical model. If the particle and substrate properties are known, it is possible to evaluate whether a particle will cause dents and erosion of the substrate in the presence of the liquid layer.

Controlled fouling experimental facility

Process parameters like carrier phase velocity, temperature, particle concentration in the flow, target material, geometry, etc., play a vital role in particle deposition and removal. On site experiments performed in real heat exchanger systems provide vital information, but as a lumped effect of several process conditions. In order to evaluate the effect of each individual parameter, it is important to perform controlled experiments. The present chapter describes the design, construction and testing of an experimental facility in which controlled experiments can be performed.

4.1 Background

Experimental methods used to understand particulate fouling can be broadly classified as follows:

- Experiments performed on-site: This involves collecting and analyzing the samples from different sections of heat exchangers. The samples are usually obtained when the plant is shut down for maintenance or can be drawn out using special probes. Specially designed probes are sometimes used to monitor the rate of fouling. The deposit structure and components are compared to the chemical composition of the fuel and conclusions are drawn thereupon based on correlations. Experiments of this kind provided important information on the overall effects of fuel composition, boiler geometry, flow conditions, temperature etc, on fouling behavior [10, 11, 14, 16, 37, 49, 64]. The experimental

data are very important to understand the effects of global boiler parameters on fouling like: influence of fuel composition, boiler geometry, temperature, feed rate of fuel, cooling water feed rates etc. However, from a numerical modeling point of view, the information obtained is difficult to use and analyze.

- Experiments performed on pilot plants or at lab scale facilities: Experimental facilities like entrained flow reactors have been widely used to evaluate the fouling tendency under controlled conditions which mimics the deposition process for superheater section of a boiler. Usually a known fuel or fuel mixture which is fed at the top of the reactor is combusted in a chamber, a probe is positioned downstream and the fouling rate is monitored with different techniques. These experiments are valuable to understand the effects of fuel and fuel mixtures, combustion technique, deposit chemistry etc., [43, 54–56]. Although the experiments provide valuable information on the deposit chemistry and relation between fuel and deposit, the effects of process conditions are not reported. The experimental data indicate the overall effects of several lumped parameters and are difficult to use in numerical modeling.
- Controlled fouling experiments: To understand the fundamental mechanisms governing particle deposition, several researchers have performed deposition measurements which provides information on capture efficiencies. The capture efficiencies are however based on the assumption that all the particles that reach a surface would eventually stick; i.e., assuming a perfect sticking condition. But for powdery deposits, the particle can stick or rebound based on several parameters. A systematic study of the particulate fouling under controlled conditions have been reported [2–5, 36, 46]. However, the experimental data available are usually for very high temperature experiments > 800 °C or at nominal temperatures. Further, a detailed parametric study of the effect of process conditions on particulate fouling was not found during the literature survey. In order to provide qualitative data for numerical studies and for better understanding, an experimental facility was necessary. The following sections describe the design, construction and operation of an experimental facility with which controlled experiments on particulate fouling can be performed under various process parameters.

4.2 Design considerations

Particle deposition depends on transport mechanisms in the vicinity of the obstacle and the interaction mechanisms between the particle and the surface. The inertial mechanism of particle deposition was covered in the previous chapter. The relevant process conditions can be briefly characterized into flow parameters, particle parameters and target parameters. Flow parameters chosen to investigate in the

present work include: carrier phase velocity, temperature, and humidity. Particle parameters include: particle concentration in the flow, particle type and particle size distribution (PSD). Target parameters that influence deposition include: target size, shape, material, orientation to the flow, liquid coating on the surface of the target etc. In most cases, changing one variable inadvertently changes another variable. For example, changing the orientation of the target geometry changes the wall shear, flow field and the interaction of particles with the surface. This exactly defines a need for a controlled experimental facility which reduces the number of unknown parameters that affect the end result as much as possible. To this end, experiments were designed to understand the governing mechanisms rather than measuring the outcome of particle deposition i.e fouling rate, temperature differences, pressure drop etc.

Particles in real systems vary from sub micrometer to several hundred micrometers. Particle transport and its eventual deposition on a surface strongly depends on the dominant transport mechanisms which in-turn depend on the particle size. Thus, one of the basic criteria was to use particles which are of the same size as found in real systems. Glass, Calcium carbonate ($CaCO_3$), and Polyethylene particles which have defined physical properties were chosen along with ash particles procured from a Dutch gasifier plant. The details on the shape and size parameters of the particles will be covered later. Further, it was expected that particle deposition depends on the flow features and target size. The relationship between flow, particles and target size can be quantified by the non dimensional Reynolds number and Stokes number. Depending on the application, the size of heat exchanger tubes can vary from 10 mm up to 300 mm and the flow velocities can range anywhere from 3 to 30 m/s. The main considerations in the initial design were to:

- achieve similar Stokes and Reynolds numbers as found in real heat exchanger systems;
- study initiation of particle deposition;
- monitor the growth rate of the fouling layer based under variable process conditions under dry conditions;
- study deposition behavior for a liquid coated surface under variable process conditions;
- devise an energy efficient and environmentally friendly system to study the above parameters and
- construct and test a facility which should be easy to handle and maintain.

4.3 Experimental facility design

Based on dimensional analysis, the experimental facility was designed such that a range of Reynolds number and Stokes number can be achieved which aids in understanding the process. At room temperature, the Reynolds number based on target size (deposition tube) can be varied from 1400 to 16000. The primary design of the system was iteratively modified several times to arrive at an optimal design which is shown in figure 4.1. The experimental setup is basically a vertically oriented wind tunnel and consists of different parts interconnected by stainless steel ducting. The following sections provides a brief description of the different parts of the setup.

- **Heater:** A specially designed compact 20 kW, 3 x 400 V electric air heater (Veab heat Tech AB) is mounted after the blower and connected by a transition duct. The heater is regulated by a thyristor and a control unit which provides over-heating cut outs. The heater requires a flow velocity of at least 1.5 m/s during operation and a thermocouple mounted at the exit of the heater provides the feed back information for regulators of the heater coils. The feed back control system regulates the exit air temperature within ± 1 °C of the set point temperature.
- **Flow conditioning unit:** The flow from the air blower is highly turbulent usually associated with large scale eddies. Although the presence of heating coils in the electric heater reduces the scale of the eddies in the flow, the flow through bends induces uneven acceleration of the flow and large scale eddies. Guiding vanes are provided in the bends which aid in streamlining the flow to some extent. The upstream flow characteristics and the flow at the test section is an important feature. Wind tunnel designs usually incorporate a combination of honeycomb structures, contractions and screens to reduce the longitudinal and lateral components of turbulence. Although particle dispersion and bulk transport of the particles in the channel strongly depends on the turbulence parameters in the duct, the focus was to achieve an acceptable mean velocity profile at the test section. A combination of flat grid, perforated plate and a wire mesh was chosen to break down the large scale eddies in the flow. A divergent (diffuser) section is provided before the flow conditioning unit and a convergent section is provided at the exit to assist in flow conditioning.
- **Screw feeder:** The experiments calls for continuous seeding of particles into the flow at required concentration. Further, the injection system must provide freedom to use different particles of varying physical properties. Commercial particle injection systems which feed the particles gravimetrically are designed for specific particles or have very limited range for which the systems can be used. These systems were economically unviable due to their high costs. In order to have a flexible system where different particles can be seeded at re-

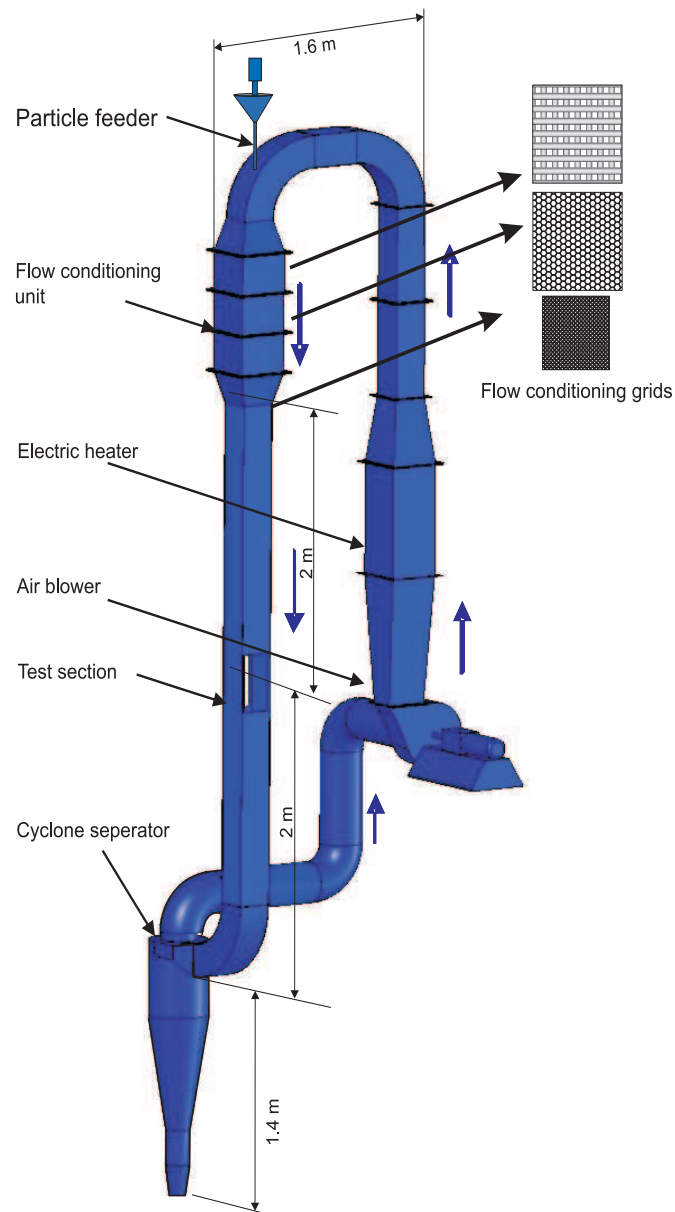


Figure 4.1: Schematic of the high-temperature controlled fouling experimental facility.

quired rates, a screw feeder was designed and manufactured. The schematic design of the screw feeder is shown in figure 4.2 (a). Particles are fed into the hopper section and a stepper motor drives the shaft of a helical screw. The he-

lical screw can be replaced to accommodate feeding of different particles. As the screw rotates, particles are transported in the helical groove of the screw and reaches the outlet. The rate of particle transport can be controlled by varying the speed of the screw feeder. Particles are injected into the flow through a connecting pipe of which one end is connected to the outlet of the screw feeder and the other end is positioned at the center of the duct. Several CFD simulations were performed to evaluate the optimal position of the particle injection point to achieve a homogeneous particle distribution in the duct. The particle injection point was selected to be at the center of the duct cross section and at the wire mesh. The particles are injected 2 m before the test section to allow sufficient residence time for the particles in the flow.

The feeder was tested for consistent output. Though the particle output from the feeder was not continuous, the average output per minute was within $\pm 8\%$ of the set value and when averaged over longer durations, the difference was within $\pm 5\%$ of the set value.

If the volumetric flow rate of air (m^3/min) is known, one can determine the amount of particles to be seeded in the flow (g/min) to achieve a certain concentration of particles in the flow (g/m^3). However for this, the output of the screw feeder at a specific rotational speed of the feeder shaft must be determined. At a given rotational speed of the feeder, particles can be collected at the outlet for different time intervals and weighed. The process must be repeated for different rotational speeds. A typical plot of feeder output with rotational speed is shown in figure 4.2 (b). The plotted values represent an average of 5 measurements for each speed and time interval. Based on the predetermined particle concentration, the required screw feeder speed can be selected using the plot for a specific batch of particles.

- Test section: The test section is optically accessible through glass windows on three sides to visualize fouling. This facilitates measurement of fouling layer thickness over a deposition tube placed in the test section. The three windows helps to capture the profile of the particle deposition layer from radial and axial directions (with respect to the axis of the deposition probe). A schematic of the test section is shown in figure 4.6.
- Cyclone separator: As the facility is a closed loop system, the presence of particles in the air can deposit within the blower or heater. An efficient particle separation/removal system is thus necessary. A cyclone separator is used to remove the seeded particles in the flow downstream of the test section. The proportions of different sections of the cyclone separator was carefully chosen based on the different particles and mass flow rates that will be used for the experiments. The detailed design and calculations of the cyclone is provided in appendix B.

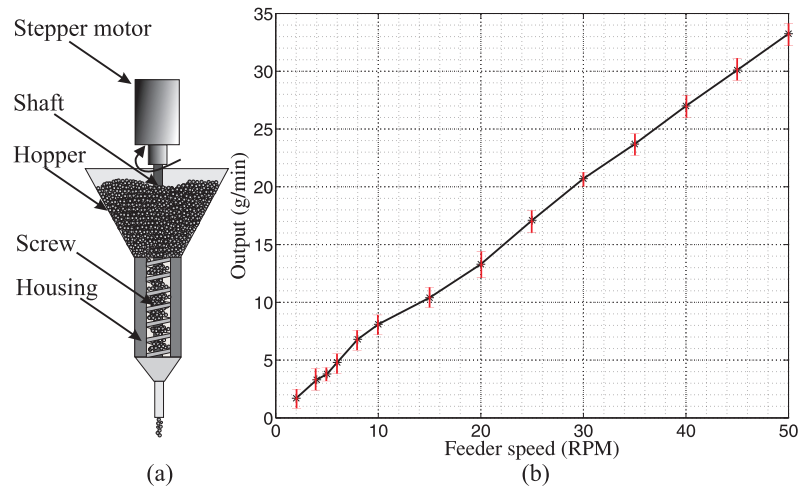


Figure 4.2: (a) Schematic representation of the screw feeder; (b) Feeder output for CaCO_3 particles with a mean diameter of $20\mu\text{m}$.

- Blower: A centrifugal air blower (Halifax) with an impeller made of corrosion and wear resistant steel (3CR12) was opted to maintain the required flow rates of the air in the system. The drive shaft of a variable speed motor is connected through a flexible coupling unit that drives the impeller at a maximum speed of 2850 RPM delivering a maximum volumetric flow rate of $0.35\text{ m}^3/\text{s}$. The coupling and bearing system are oil cooled to withstand the high temperatures. The maximum pressure gradient of the blower is 1200 Pa at maximum speed under nominal conditions.

It is necessary to operate the blower under a higher static pressure head than the sum of pressure drops across various regions. The pressure drop in the whole system is the sum of individual contributions by the heater, ducting, flow conditioning unit and the cyclone separator. The calculations for the system pressure drop are given in appendix B. The blower performance curve is shown in figure 4.3. The blower performance curve corresponds to maximum flow rate of $0.2\text{ m}^3/\text{s}$ at room temperature. The performance curves at higher temperatures were not available. The total pressure drop at various temperatures are plotted and at nominal temperatures, the total pressure offered by the system at maximum flow rate is about 850 Pa . The pressure head of the blower for corresponding flow rate is 1100 Pa which is sufficient to keep the flow of air through the system.

- Ducting: The different parts of the experimental facility is interconnected by stainless steel ducts with a smooth surface finish. The ducts and the parts are

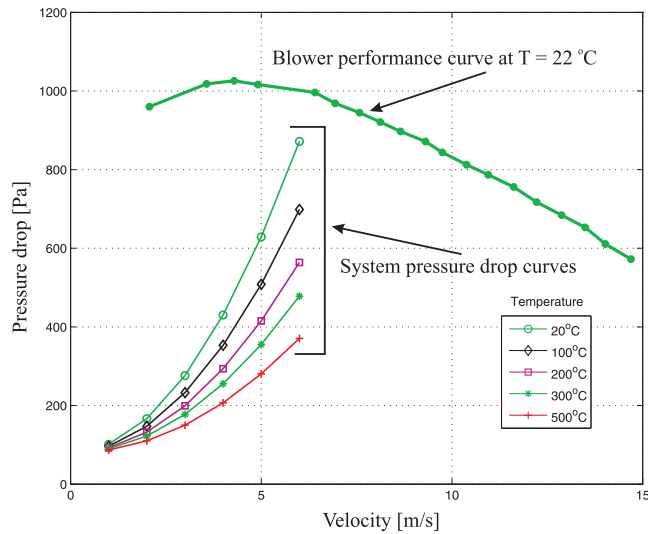


Figure 4.3: Pressure head across the blower at room temperature under various flow rates (plotted in terms of velocity due to constant cross sectional area) and the total pressure drop of the system for varying temperatures.

provided with flanges and can be clamped with bolts and nuts. A flexible sealant is used to fill the gap between the flanges to avoid leakages.

- **Insulation:** The setup is insulated with two layers of material. Ceramic wool, which can withstand temperatures up to 1200 °C forms the first layer of the insulation over which a glass wool insulation is used. Based on the calculations, the expected outer temperature of the insulation was found to be 40 °C at a maximum temperature of air inside the duct which was 550 °C .
- **Control unit:** The heater, blower and the screw feeder can be controlled via a computer through the control unit. The system variables are automatically logged continuously in order to keep track of the changes.
- **Supporting structure:** The ducting and the cyclone separator spans about 7 m high and is 2 m wide. The facility was designed to be in 3 stages, one under the ground level, the second one at the ground level and a third level. A supporting structure for the facility was designed by considering the following:
 - **Ease of movement:** The particle feeder is positioned on the top most point of the experimental facility and it is important to facilitate easy and safe accessibility to the screw feeder and all other parts.
 - **Safety:** The structure should be built such that the important parts are

readily accessible, easy to get away in case of emergency and structurally sound.

- Provision for expansion and contraction: High temperature experiments induces thermal expansion and contractions. If a rigid system is built for high temperatures, thermal stresses developed will be high and undesirable. The supporting structure must be able to allow easy expansion of parts and contraction during recovery.
- The space should be economically used with minimal footprint and maximum usable area.

4.4 Instrumentation

A Pitot tube with an integrated K-type thermocouple was used to measure the velocity in the test section (*KimoTM* - TC K). The elliptic shaped Pitot tube can be used up to 1000 °C . A high sensitivity ultra low differential pressure sensor (Sensirion) was connected to the dynamic and static ports of the pitot tube. The differential pressure transmitter has a resolution of 0.002 Pa which allows measurement of velocity with high resolution. A hot film anemometer (TSI VelciCalc Plus) was used to calibrate the pitot tube. The error associated with the pitot tube measurements was found to be 2-3%. The pitot tube system offers direct measurement of air flow at higher temperatures by incorporating temperature compensation. However, the accuracy of the measurements at higher temperatures was not determined.

The humidity of air for experiments which were performed at room temperature was measured with the TSI hand held meter. The thermocouples used for temperature measurements were of K-type with an accuracy of ± 0.4 °C . A set of fast response thermocouples were installed at the windows to indicate and shut down the system in case of window breakage during high temperature experiments. A weighing machine with a least count of 0.01g was used to calibrate the screw feeder. A precision jewelers weighing machine with a least count of 1 mg was used to measure the mass of the particles deposited in the experiments. A Scanning Electron Microscope (SEM) was used to study the particles and to obtain particle size distributions (PSD). To determine the PSD, a set of 10 images was acquired for each batch of particles to get a representative value. Typical SEM images for glass and calcium carbonate particles are shown in figure 4.5.

4.5 Measurement technique for particle deposition

A schematic representation of the test section and the measuring technique to determine the fouling layer thickness is shown in figure 4.6. Glass windows provided on three sides of the test section facilitate observation of particle deposition over the



Figure 4.4: *Top: Photograph of the experimental facility. Bottom: Schematic of the full facility.*

tube from two principal sides: inline and perpendicular to the tube axis. A compact LASER diode module with an in-built lens system (Roithner Laser Technik) produces a laser sheet of 1.5 mm thickness. The laser sheet illuminates the region around the

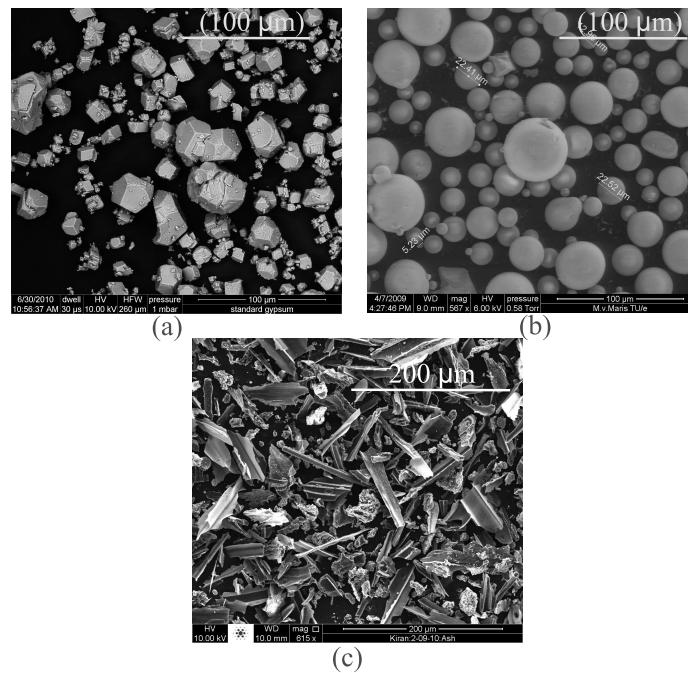


Figure 4.5: SEM images of the particles used. (a) CaCO_3 (b) Glass (c) Ash.

deposition tube. A mirror is provided on the opposite side of the laser system to illuminate the other half of the tube. The laser and mirror system can be aligned to avoid noise due to reflected light. Further, the laser system and the camera forms an integral system and are mounted on a traversing system. By moving the camera towards or away from the test section, the distance between laser sheet and camera focal point being fixed, facilitates measurement of axial profile of the deposit layer on the tube. However, experimental observations indicated a uniform deposition in the axial direction as shown in figure 4.10 and a different camera was used to obtain images from the other side rather than traversing the system. A digital video camera with a resolution of 800×680 pixels is used to measure the growth of fouling layer thickness over the cylindrical tube. A calibration paper (graph paper) can be stuck on to a specially designed clamp which can be fixed on the tube. This is used to align and focus the imaging system and to get the reference image for calibration. Images of the tube are taken before, during and after the experiments.

Figure 4.7 (b) and (c) show the raw images taken at the start and end of the experiments respectively. The clean tube is taken as a reference and the fouling layer thickness can be measured using pixel count. The measurement error is 3 to 7 pixels which corresponds to a maximum error of 3% in the measurement of layer thickness.

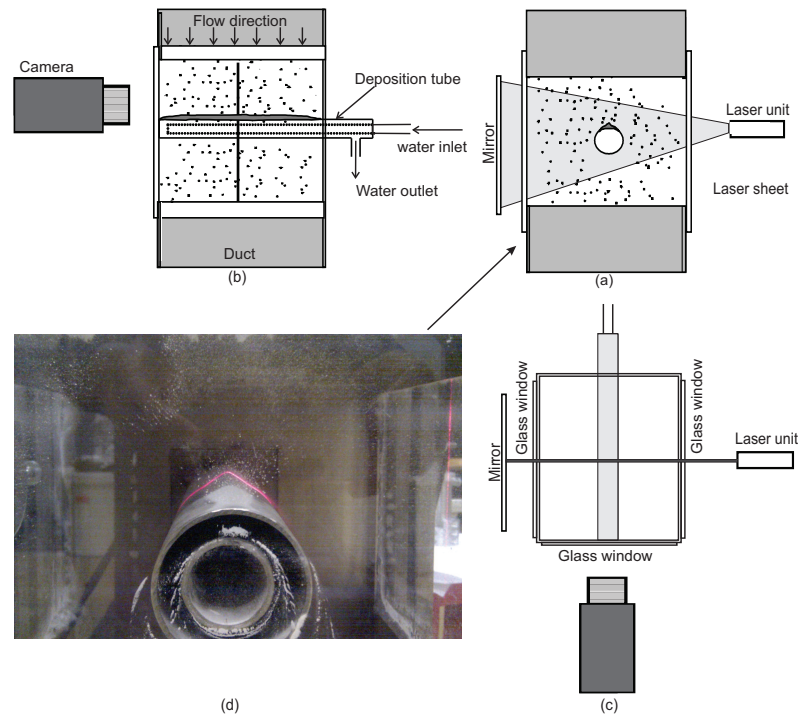


Figure 4.6: Test section and schematic representation of the measurement technique for thickness of fouling layer. (a) View along the tube axis, (b) View perpendicular to the tube axis, (c) Top view and (d) Photograph of the tube as seen from glass window.

The axis of the tube and camera are positioned in the same line, but the camera axis is shifted above the axis of the tube to obtain a better field of view. The error associated due to skewed view induced by the camera shift is less than 0.5%. Figure 4.7 (a) shows the processed image which is obtained by overlaying the snapshots taken at different instances of time during the experiment. The edge of the fouled layer for each snapshot is obtained and the colors are inverted for a better view. The plot shows typical changes in the deposit layer which grows in a direction opposite to the flow direction. The measurements reported are for the maximum thickness of the layer which occurs at the streamwise stagnation line.

4.6 Operation and testing

An important requirement of the experimental setup is to operate at the set point values for long durations without fluctuations in the process conditions. Further, it is necessary to evaluate the flow parameters. The experimental setup was tested

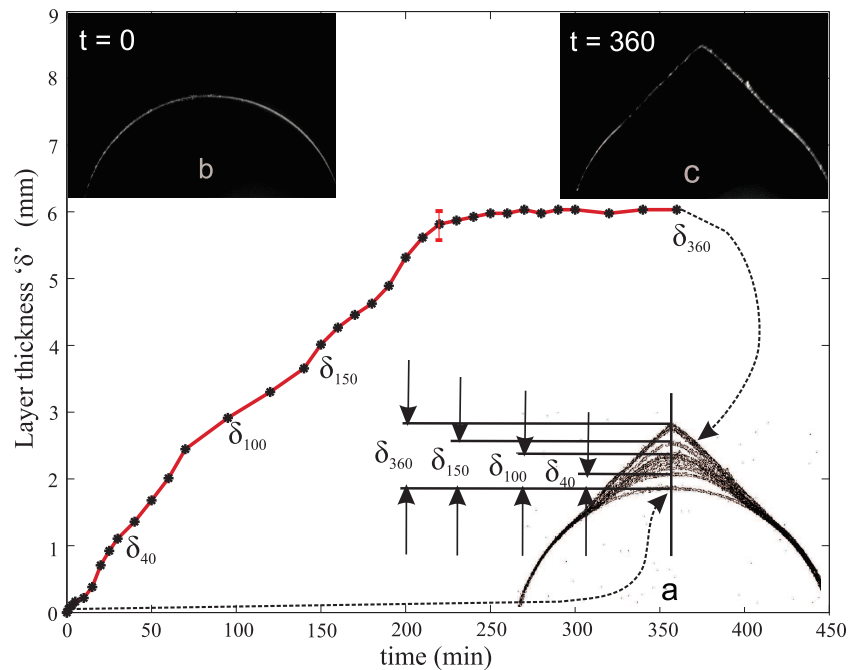


Figure 4.7: Typical fouling layer growth profile. Figure shows the deposition of Ash particles on stainless steel tube. (a) Processed image, (b) Raw image at the start of experiment, (c) Raw image at the end of the experiment.

for integrity of various parts and for process conditions. The system was tested for elevated air temperatures at the test section. Glass cannot withstand thermal shock and as the test section windows are made of soda-lime glass, the system cannot be heated up or cooled down beyond 3 to 4 °C /min. Thus, the system slowly heats up and meanwhile, the other parts get hot and slowly stabilize. Once the system reaches the required temperature of air at the test section, it was observed that the temperature remains within ± 1 °C of the set point (after a hold on time of about 30 mins) as shown in figure 4.8 (a). The maximum temperature attainable at the test section was 550 °C .

The velocity in the test section remained within $\pm 2\%$ of the set point value. Before installing the screw feeder and flow conditioning system, the turbulence intensity was measured with Hot Wire Anemometry (HWA). A Constant Temperature Anemometer (CTA) probe with a Titanium wire of 5 μm was used in conjunction with Dantec/LabView data acquisition system. The flow was sampled at 25 kHz at the center of the duct. The statistics for the complete cross section of the test section could not be obtained due to breakage of the CTA. This can be attributed to the particles in different parts left over from the manufacturing process. However, the

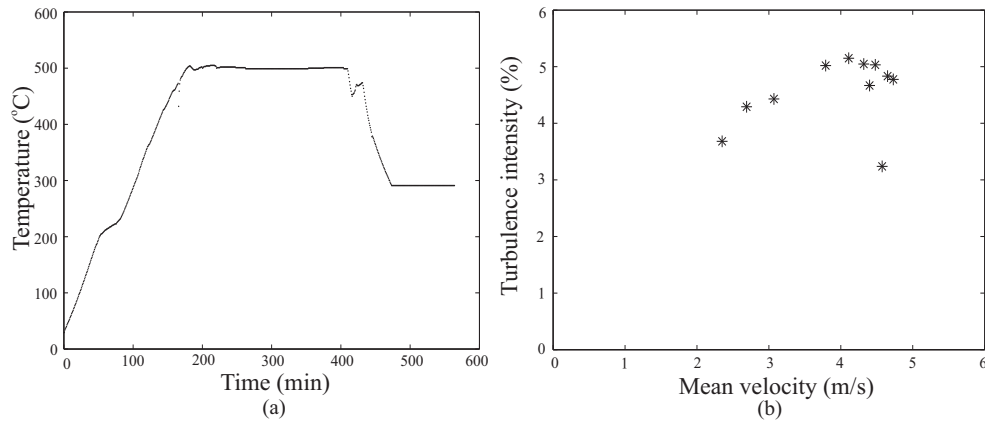


Figure 4.8: (a) Air temperature as a function of time at the test section. (b) Turbulence intensity at the center of test section.

center point data samples provide a measure for maximum turbulence intensity in the duct. The observed turbulence intensity 100 mm above the deposition tube for different velocities was found to be between 3 and 5%. It should be noted that this turbulence intensity qualitatively represents the maximum values. The system was later incorporated with flow conditioning units and it is assumed that the (stream-wise) turbulence intensity values will be smaller.

To obtain the velocity profile at the test section, the velocity at 100 mm above the tube axis (without the tube) was measured with the pitot tube. The pitot tube was traversed from one inner wall of the duct to the other in steps of 5 mm. Figure 4.9 shows the velocity profile in the duct in two mutually perpendicular directions. It can be observed that the maximum boundary layer thickness developed at 5 m/s is about 35 to 45 mm and the velocity is moderately even in the center region for velocities up to 3 m/s. At higher velocities, the velocity profile is skewed on one of the sides but the difference in magnitude is not more than 4% of the mean value.

4.7 Experimental procedure

A short description of general procedure(s) followed during the experiments is outlined here. For experiments involving significant deviation in the procedure, relevant explanation is provided in chapter 5.

- Preparation of the test section and the deposition tube: Experiments with different tube geometries, materials and orientations have been performed. As a first step, the ducting above and below the test section was cleaned by scrubbing off the deposited particles. Cleaning of the ducts was however not done

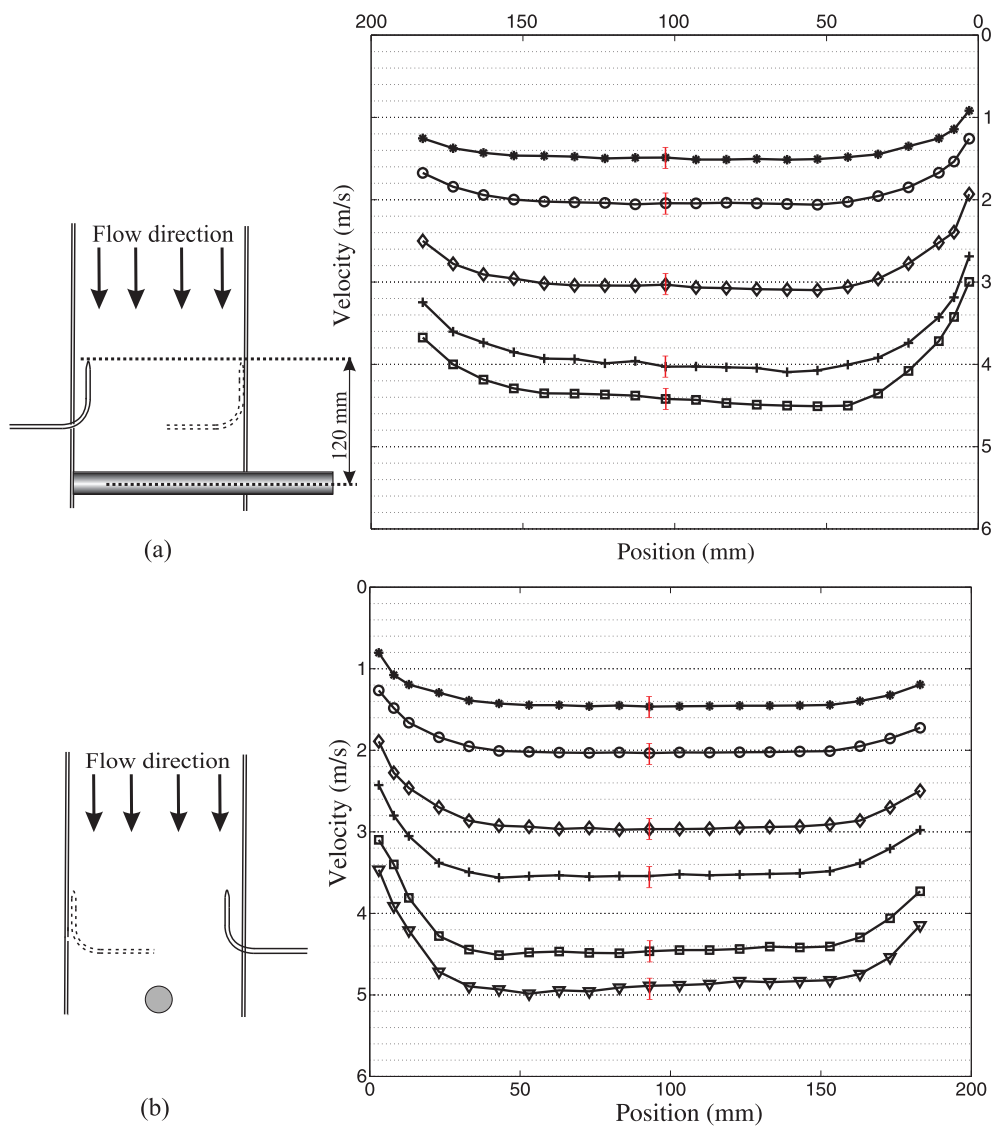


Figure 4.9: Top: Schematic representation of the traversing of the Pitot tube parallel to the deposition tube and the corresponding velocity profiles for different mean velocities. Bottom: Pitot tube traversing perpendicular to the deposition tube axis and the corresponding velocity profiles for different mean velocities.

after each experiment, but was based on the amount of deposit formed. The glass windows were cleaned with a water and soap solution. The windows were wiped off with industrial wiping paper and dried. The deposit tube was

cleaned with a high pressure air gun to thoroughly remove adhered particles. Care was taken to ground the deposition tube so as to eliminate charge build up.

- Reference image: The camera and lens system was adjusted to take a reference image before each experiment to relate the thickness of the layer buildup to the physical length scale. A standard graph sheet was used as a reference for the calibration.
- Flow setting: The blower was switched on with the required rotational speed to obtain the necessary flow velocity. A Pitot tube inserted above the deposit tube was used to measure and adjust the velocity of the gas phase.
- Temperature: For the experiments performed at elevated temperatures, the gas phase temperature was gradually increased to the set point temperature at the rate of 5 °C /min to avoid sudden changes in temperature. A thermocouple mounted in the Pitot tube provided the temperature reading. The system was held constant at the required temperature at the test section for at least 1 hr before the experiments commenced in order to allow thermal expansion of the ducting and to reach a quasi-steady thermal state.
- Particle seeding: The instant at which the particle seeding starts is taken as the reference point for the start of the experiment. Images are taken before the experiments and during the experiments at several intervals of time which correspond to the data points.
- End of experiments: The experiments were terminated by simultaneously turning off the feeder and the blower. However, for high temperature experiments, the feeder and heater are switched off while allowing the air to gradually cool down while the blower was on.
- In most of experiments, the deposit layer was uniform in thickness along the tube axis. Hence, all the measurements reported here correspond to the layer thickness formed at the center of the tube (i.e. 100 mm from the duct wall). For some experiments with mixtures and ash particles, the maximum deposition has been reported. Figure 4.10 shows the axial deposition pattern of glass and ash on a circular tube. Further, two experiments were conducted for a duration lasting 10 hours. It was noted that once the layer achieves the asymptotic state, the layer thickness does not deviate much with time. Hence the experiments were usually limited to 1 to 2 hours after the layer reaches an asymptotic state as the focus is on the particle deposition mechanisms and not on measuring the fouling resistances which would otherwise call for experiments of longer durations. Experiments were repeated with glass and $CaCO_3$ particles to evaluate the repeatability and the results indicated a deviation of 4-6%. Some of the

experiments were repeated in order to compare with similar experiments and humidity conditions and in all the cases, the repeatability of the experiments was within 5%.

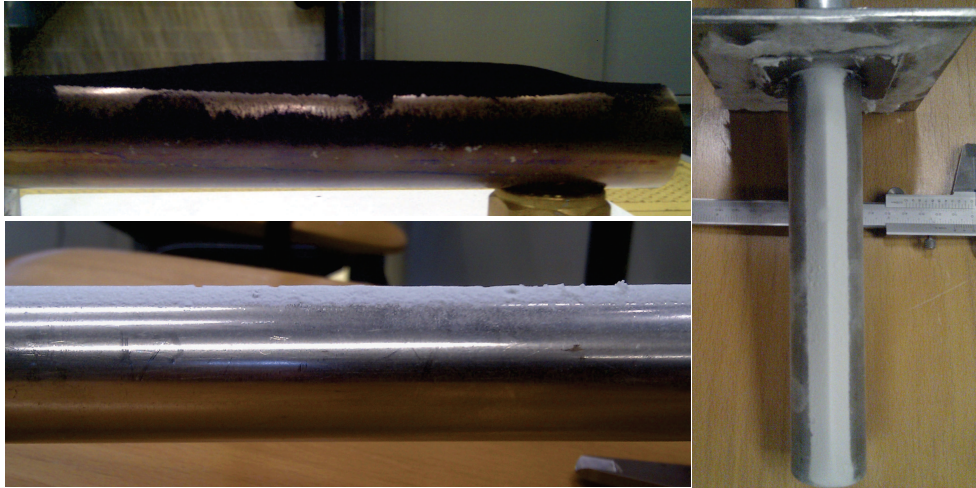


Figure 4.10: *Particles deposited on the tube. Pictures were taken after the experiments.*

Controlled fouling experiments

Particle deposition and removal are governed by various flow parameters. In-situ experiments in power plants provide information on the global effects of different parameters. However, in order to gain fundamental understanding on the individual effects of process conditions, controlled fouling experiments are conducted and discussed in the present chapter. The influence of parameters like gas phase velocity, temperature, tube geometry and orientation, particle properties etc are evaluated. The aim is to present a phenomenological description of the particulate fouling process and the quantification of the dynamics associated with deposition and removal. Further, the range of process conditions which are influential on the initiation, growth and destruction of fouling layers are aimed at.

5.1 Background

Yeong et al. [69] performed experiments in a horizontally oriented hot wind tunnel to reproduce the conditions of a utility boiler. Using a combustor fueled with oil, they achieved gas temperatures in the range of 700 to 1000 °C. Calcium hydroxide particles were used as foulant particles and Cr-Mo steel was used as the material for the fouling probe in their experiments. Using thermocouples embedded in the probe, they reported the local fouling factors at 0°, 90° and 180° from the stagnation point. The fouling resistance at the streamwise stagnation point was found to be larger than at 90° and 180° indicating higher particle deposition at the stagnation region. For increasing foulant deposition, they reported a decrease in heat transfer rate

and increase in the fouling factor. The experimental results which are reported are however limited to one specific condition and the effect on fouling due to variation in process conditions is not reported.

Thonon et al. [58] studied the effect of fluid velocity and particle concentration on the fouling behavior of a liquid/liquid plate heat exchanger. By varying the corrugation angle of the plates, they observed a reduction in the fouling tendency with increasing angles and the asymptotic fouling resistance was found to be inversely proportional to the square of the fluid velocity and directly proportional to the particle concentration.

In order to study heat recovery from exhaust gases, Kaiser et al. [36] devised an experimental facility to provide a description of the fouling layer formation in humid and solid loaded air streams. In their experiments, the air stream was seeded with $CaCO_3$ particles and humidified by injecting small water droplets. The water droplets evaporate and condense on the deposit tube along with the fouling particles. The mass accumulated on the fouling probe placed vertically in a channel is reported for various vapor and solid loading. They reported increasing fouling tendency with condensation as compared to dry deposition. Based on the mass deposition data, they conclude that moderate condensation promoted deposition while an increased moisture content and condensation resulted in the reduction and destruction of pre-formed fouling layers.

Abd-Elhady et al. [5] studied the effect of gas phase velocity on dry particulate fouling in a tube bundle. In an upward flowing gas, glass, copper and bronze particles were seeded. The focus of their study was on the centrally placed cylinder in an array of 3×3 cylinders. For increasing gas velocity, they observed a reduction in the thickness and the circumferential width of the fouling layer.

Particles that adhere on to a surface can be removed by the shear induced by the flow of the fluid over the particle. Yiantsios and Karabelas [70] studied the adhesion and removal of spherical glass particles both experimentally and theoretically. Due to the hydrodynamic forces of the flowing fluid medium over the adhered particle, different forces act on the particle which may cause the particle on the surface to slide, lift off or roll over the surface. They conclude that the force required to roll a particle over a surface is much lesser than the force necessary to slide or lift the particle. Hence, rolling moment is the primary mechanism for particle detachment. In a similar study, Zhang et al. [72] suggested that whenever the rolling moment acting on a particle resting over a flat surface overcomes the adhesion forces holding the particle in position, rolling occurs. A brief discussion on the particle detachment from a surface is provided in the next chapter. Based on the analytical model of Zhang et al. [72], Abd-Elhady et al. [5] observed that dry particulate fouling can be avoided if the gas phase velocity is maintained more than the minimum velocity required to roll the smallest particles in the gas stream. The corresponding velocity is termed as limiting velocity for fouling. Further, by analyzing the bronze and copper

particles deposited over the tube after experiments (done at 200 °C lasting 9 hours), they reported sintering behavior of particles. Sintering induces strong bonding between the particles and is hence difficult to remove. They were able to establish a criterion for gas phase velocity to avoid particulate fouling and also the effect of temperature in terms of sintering between the particles.

In their further studies related to particulate fouling, Abd-Elhady et al. [3] conducted experiments to evaluate the effect of flow direction on fouling. Comparing the results of horizontal, upward, downward and flow at an angle (45° with respect to the horizontal), they observed that a downward flow orientation results in the least fouling tendency. Further, by injecting external particles in a downward flow, they observed that the previously deposited foulant particles can be removed. However, for the upward and horizontal flow, the externally injected (sand) particles did not remove the pre-deposited particles [2]. A study based on the fouling tendency for tubes having cone structures with different apex angles attached to circular cylinders suggested that fouling can be minimized with the cone structures [4].

Based on the data collected for fouling in convective zones of a coal-fired boiler, Kalisz and Pronobis [37] suggest that in order to maximize fouling layer build up time, i.e. to minimize soot-blowing frequency, it is better to consider tube arrangement with a lower longitudinal pitch and high flue gas velocities.

The brief literature review provided here iterates the importance of process parameters on particulate fouling. Some vital points that can be drawn from the literature related to particle fouling include:

- Increasing gas phase velocity indicates reduction in fouling. Under dry conditions, the rolling moment model describes the limiting velocity to avoid fouling of spherical particles [5, 37, 58]. Further, a downward flowing fluid medium with particles has lesser fouling tendency as compared to an upward, horizontal or inclined flow [3].
- The geometry of the heat exchanger tube is an important parameter in terms of tube arrangement and shape [5, 37].
- Fouling is directly proportional to the concentration of foulant particles in the fluid medium [58, 69].
- The presence of a liquid film due to condensation effects greatly enhances particle deposition [55]. However, too much of liquid induces weakness in the fouled layers and the layer breaks and washes off [36].

Although it is evident that increasing the velocity reduces the fouling tendency, there is no clear understanding of the relationship between changes in velocity to that of fouling. In the present experimental study, an effort is made to (further) decouple the process parameters and to study their effects on particulate fouling under controlled conditions. An effort has been made to capture the growth dynamics of the layer

Table 5.1: Abbreviations for terms used in table 5.2

V_g	Gas phase velocity 100 mm above the tube axis
C_p	Particle concentration in the flow
T_g	Gas phase temperature
SS Dx	Stainless steel circular tube of outer diameter $x = 21, 30, 38$ and 51 mm
Sq	Square tube of 40 mm side
G(y)	Glass particles with mean diameter of $y = 20, 55, 80$ and 143 μm
Ca(40)	Calcium carbonate particle with mean diameter of 40 μm
UHMWPE	Ultra high molecular weight poly ethylene
Ash	Ash particles procured from a Dutch biomass gasifier
PVC	Poly Vinyl Chloride
Mix 1	Mixture of G(20) and Ca(40) 50:50 by weight
Mix 2	Mixture of G(20) and Ca(40) 75:25 by weight
Mix 3	Mixture of G(20) and G(55) 50:50 by weight
Mix 4	Mixture of G(20) and G(80) 50:50 by weight

thickness and to correlate the changes in the deposition pattern to the gas phase velocity, temperature, and particle properties. Further, the presence of liquid is known to enhance the fouling behavior and the initial stages of fouling in the presence of liquid has to be understood. Together with the influence of process parameters, the aim of this study is to provide (qualitative and to some extent quantitative) information which can be used to validate numerical models.

As the focus of this study is to evaluate the effect of several factors, a generalized experimental approach is adopted. A wide range of experiments with varying parameters are performed. Table 5.2 provides an overview of the experiments. Basically, the experiments can be categorized based on the type of particles used, particle concentration in the flow, velocity, temperature and deposition tube properties. A combination of these factors were chosen for the experiments. The varying parameter is colored in gray. The notations (abbreviations) used in this chapter are listed in table 5.1.

5.2 Initiation and layer growth dynamics

Experiments were done to evaluate the mass deposition over the cylinder with CaCO_3 particles to understand the initiation of the fouling layer. Figure 5.1 shows the mass of the particles that deposit on a stainless steel cylinder. The inlaid plot indicates the initial values of mass deposition with time. The SEM images (a) and (b) correspond to the particles collected after 10 seconds and after 1 hour. The gas velocity was maintained at 1.55 m/s and the particle concentration was maintained at 2 g/m³.

Table 5.2: Part 1: Overview of the experiments that have been performed. The main parameter that has been varied is colored in gray.

Particle	$C_p(g/m^3)$	V_g (m/s)	$T_g(^{\circ}C)$	Tube
1) $G(20)$	2.0	1, 1.55, 1.8, 2, 2.25, 2.5	22	SS D30
2) $Ca(40)$	2.0	1.5, 3, 5	22	SS D30
1) $G(20)$	0.2, 0.8, 2.0	1.5	22	SS D30
2) $Ca(40)$	2.0, 6.0, 8.0	1.5	23	SS D30
1) $G(20)$	2.0	1.5	22, 200, 500	SS D30
2) $Ca(40)$	2.0	1.5	23, 500	SS D30
3) UHMWPE	0.25	1.5	20, 70, 100	SS D30
$G(20)$	2.0	1.5	25	Glass, Brass, Steel, Copper, Aluminum, PVC
$G(20)$	2.0	1.5	23	SS D21,D30 D38,D51
$G(20)$ $Ca(40)$	2.0	1.5	25	
<i>Ash</i>				
$G(20, 55, 80, 143)$	2.0			
Mixture 1,2,3,4	2.0			
UHMWPE	0.38	1.5	23	SS D30
<i>Ash</i>	0.3			
(Influence of liquid layer)				
$G(20), G(143), Ca(40), Ash, Glycerol$	2	1.5, 3.0	23	SS D30, PVC, Sq(45 $^{\circ}$)
$G(20), G(143), Oil 1(\mu = 0.049 \text{ Pas})$	2	1.5		SS D30
$G(20), G(143), Oil 2(\mu = 0.156 \text{ Pas})$	0.25	1.5		SS D30

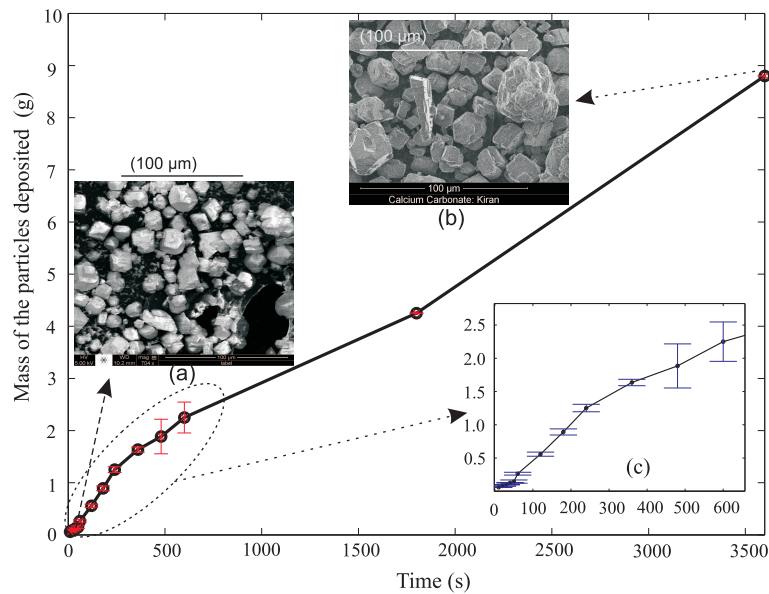


Figure 5.1: Mass of $CaCO_3$ deposited on a stainless steel tube. $V_g = 1.5$ m/s and $C_p = 2$ g/m³. (a) SEM image of the particle sample collected after 10 seconds; (b) SEM image of the particle sample collected after 60 minutes; (c) Zoomed in view for the mass deposited with time during first 10 minutes.

The cylinder was inserted in the flow for a specific time interval and was then taken out. The deposited particles were carefully collected with a small artist's brush to minimize the loss of particles. The collected particles were weighed on a precision weighing machine with a least count of 1 mg. A mean value for 5 tests performed for each time interval is reported in order to average the error associated with insertion and removal of the deposition probe. It has been reported by earlier studies by Abd-Elhady (2004) that fine particles are most likely to stick first to the tubes as compared to the coarse particles because smaller particles have a higher sticking velocity [44]. The particles collected after the experiments were analyzed with a scanning electron microscope and it was observed that the number of smaller particles found in the samples collected after 10 seconds was higher than for the samples collected at 60 minutes, thus confirming the earlier findings that smaller particles deposit first and aid the deposition of larger particles. The plot of mass deposition indicates a linear trend which increases monotonically up to 60 minutes of experimental duration, a similar trend as seen in the evolution of fouling layer thickness (see figure 5.2 (b)).

5.3 Influence of flow parameters

5.3.1 Effect of gas phase velocity

Figure 5.2 (a) shows the evolution of the thickness of the deposit layer at the stagnation line for glass particles depositing over a stainless steel tube of 30 mm in diameter. The particle concentration in each experiment was maintained at 2 g/m^3 . The center line thickness increases monotonically for the period where the deposition rates are more than the removal rate. The layer thickness reaches a constant value after a certain duration showing an asymptotic behavior where the particle deposition and removal rates are balanced. The layer thickness at the stagnation point for $V_g = 1 \text{ m/s}$ was observed to be 6.7 mm. Increasing the flow velocity from 1 m/s to

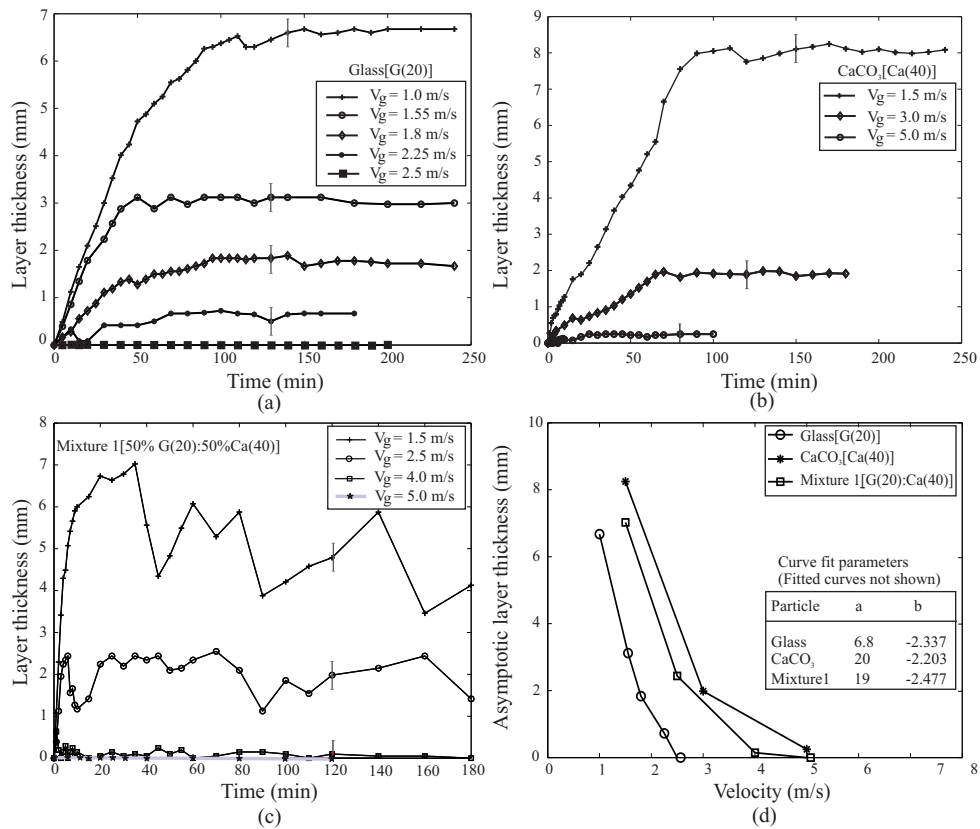


Figure 5.2: Changes in deposit layer thickness with time and velocity for (a) Glass, (b) CaCO_3 and (c) Mixture of glass and CaCO_3 particles. The particle concentration for all cases is 2 g/m^3 . (d) Variation of asymptotic layer thickness with velocity for different particles. Table shows the constants of curve fit to the data.

1.5 m/s resulted in a lower growth rate and the overall thickness at the stagnation line reached was 3.15 mm. Thus a small increase in the velocity resulted in almost half the thickness. The circumferential growth was also found to be correspondingly less at higher velocity. For a flow velocity of 1.8 m/s, the overall thickness at the stagnation point further reduced to 1.8 mm and for a flow velocity of 2.25 m/s, the thickness was found to have a maximum of 0.73 mm. Increasing the gas velocity to 2.5 m/s resulted in no deposit formation and the tube remained clean.

The deposition of calcium carbonate particles ($C_p = 2 \text{ g/m}^3$) over a stainless steel tube for different velocities is shown in figure 5.2 (b). The general trend in the variation of the fouling layer thickness with time is similar to the trend observed for glass particle deposition. The maximum layer thickness at the center was found to be 8.2 mm when the velocity was 1.5 m/s. Increasing the velocity to 3 m/s resulted in a layer thickness of 2 mm. The deposition at the maximum velocity attainable (5 m/s) was found to be 0.25 mm.

The influence of increasing velocity on the deposition of a mixture of glass and CaCO_3 particles [G(20):Ca(40)] is shown in figure 5.2 (c). A similar trend of decreasing layer thickness is observed for increasing gas velocity. The asymptotic layer thickness formed on the tube for different type of particles with varying velocity is shown in figure 5.2 (d). For all the three different particle types considered, it is observed that the trend of the decrease in the layer thickness with increasing velocity is similar. A curve fit with a confidence level of at least 95% to the experimental data indicates a power law relation of the form

$$\delta_{max} = aV_g^b \quad (5.1)$$

where a and b are the constants of the curve fit. The curve fit parameters are tabulated within figure 5.2 (d) and it can be seen that the value of b is in the range -2.3 to -2.5. Steinhagen and Middis [51] measured the fouling resistance in a plate heat exchanger under different flow velocities and observed that the asymptotic fouling resistance was inversely proportional to the velocity squared. In a similar study, Thonon et al. [58] studied the effect of velocity and corrugation angle of a plate heat exchanger. By fitting curves to the asymptotic fouling resistance values for different geometries, they too report a similar relationship. The results in principle indicate that fouling is strongly affected by the flow velocity and it is interesting to note the similarities between present results for fouling layer thickness and those corresponding to fouling resistance in plate heat exchangers.

Higher velocities in the gas phase result in two scenarios: it increases the particle inertia and the wall shear stress on the cylinder surface. As discussed earlier in chapter 2, the particles that arrive at the surface and impact at velocities greater than the critical sticking velocity always rebound. Further, due to the higher shear induced by the fluid, the particles can be carried away by the fluid medium. As discussed earlier, Abd-Elhady et al. [5] suggest that in order to avoid fouling, the gas phase velocity has to be more than a certain value which corresponds to the minimum

velocity necessary to roll a particle adhering over a flat surface. However, the particle impaction behavior coupled with the effects of fluid shear can be a determining factor which needs to be investigated in detail.

5.3.2 Effect of particle concentration

Suspended particulate matter in flue gases generally varies from a few mg/m^3 to anywhere between $10\text{--}20 \text{ g}/\text{m}^3$ based on different process conditions and feedstock. Figures 5.3 (a) and (b) show the effect of varying particle concentration in the flow for experiments with glass and CaCO_3 particles for a gas phase velocity of $1.5 \text{ m}/\text{s}$. Increasing the particle concentration from 0.22 to $2 \text{ g}/\text{m}^3$ results in a small deviation

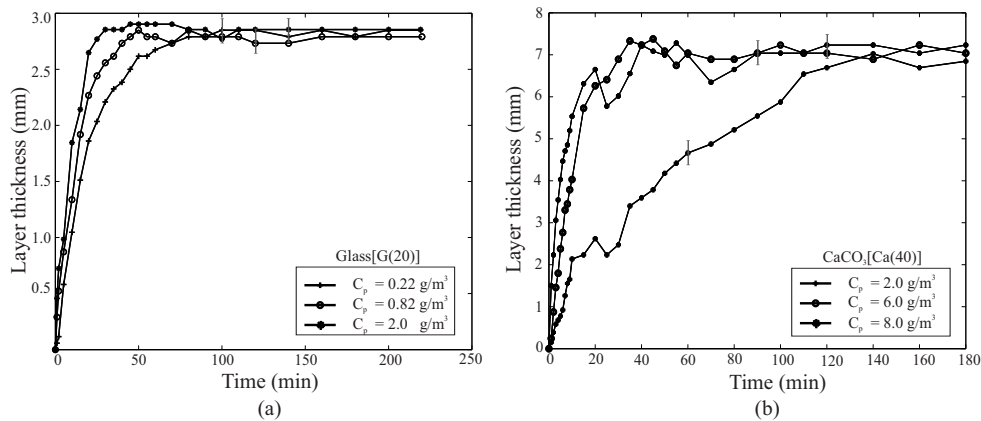


Figure 5.3: Changes in deposit layer thickness for varying particle concentration. Gas velocity is $1.5 \text{ m}/\text{s}$ for all cases. (a) Glass particles (b) CaCO_3 particles.

in the initial growth rate for glass particles, but after about two hours of operation, the asymptotic layer thickness for each case is of the same order. However, the rate of growth for CaCO_3 particles at $2 \text{ g}/\text{m}^3$ is much lower than at $6 \text{ g}/\text{m}^3$. Thus, the rate of fouling layer growth is directly proportional to the particle concentration but the asymptotic thickness is quite the same. Thonon et al. [58] report a similar relationship between the fouling resistance and particle concentration in a plate heat exchanger.

5.3.3 Effect of gas phase temperature

Figure 5.4 shows the results for the experiments performed with glass and polyethylene particles at a velocity of $1.5 \text{ m}/\text{s}$ for different temperatures.

Glass particles retain their physical properties up to a transition temperature of around $550 \text{ }^\circ\text{C}$. Experiments done at 300 and $500 \text{ }^\circ\text{C}$ showed no significant changes

in the final thickness of the layer as compared to the experiments done at room temperature shown in figure 5.4 (a). The initial stage of the layer showed decreasing growth rate with increasing gas temperature. At higher temperatures, the viscosity of air increases and hence, the Reynolds number and the particle Stokes number correspondingly change. The surface energy is one of the important criterion for dry particle deposition. However, the changes in surface energies associated with the particle and substrate at higher temperatures could not be found.

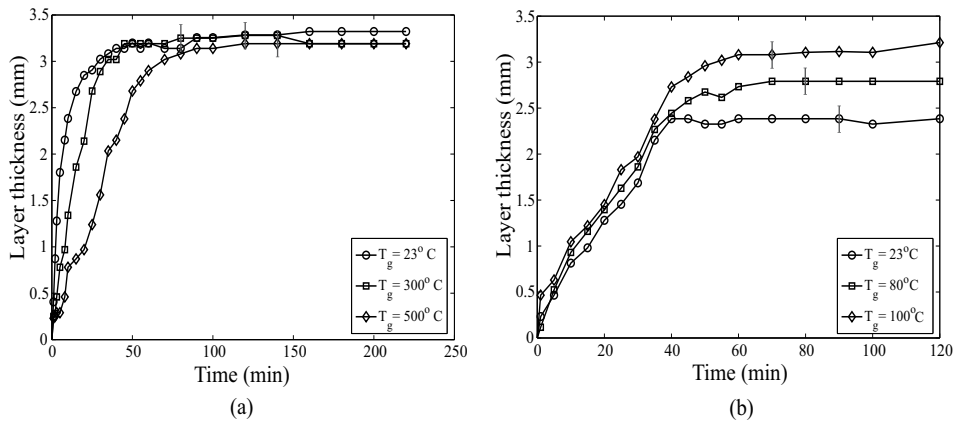


Figure 5.4: Changes in layer thickness for particle deposition at gas velocity of 1.5 m/s and particle concentration of 2 g/m³ at different temperature levels; a) glass particles; b) UHMWPE particles.

Figure 5.4 (b) shows the layer growth for the polymer particles at different temperatures which shows an increase in deposit layer thickness with increasing temperatures. The softening temperature of the polymer used was around 80°C and for the experiments performed at 80 and 100 °C, the rate of deposition and the final thickness correspondingly increased indicating the importance of particle properties. At higher temperatures, the particles become softer (the yield strength reduces) and the particles can deform plastically at much lower loads as compared to low temperature impacts. Thus, at higher temperatures the deposition increases. The nature of the polymer material used was not studied and it could display visco-elastic and visco-plastic behavior. However, the experiments indicate that the material properties play an important role in the deposition process.

A separate experiment was conducted for glass particles with a water cooled tube to introduce non-isothermal conditions. The results for the non-isothermal deposition was also similar to the isothermal conditions. The difference in the inlet and outlet temperature of the water was around 3 °C at 0.15 kg/s of mass flow rate for the gas temperature maintained at 350 °C. Thermophoretic forces due to temperature gradients act on small particles in the sub-micrometer range and in the present

case, the thermal gradient was too low and the size of the particles were comparatively big for any significant thermophoretic force to act on the particles.

5.4 Effect of particle type and size distribution

Figure 5.5 (a) shows the deposition behavior of glass, $CaCO_3$ and ash particles. The concentration of glass and $CaCO_3$ particles was maintained at 2 g/m^3 and the concentration of ash particles is 0.3 g/m^3 . The gas velocity was maintained at 1.5 m/s . Although the concentration of ash particles is lower than that of the other two, it is seen that the growth rate is higher for ash particles. Ash particles in the present

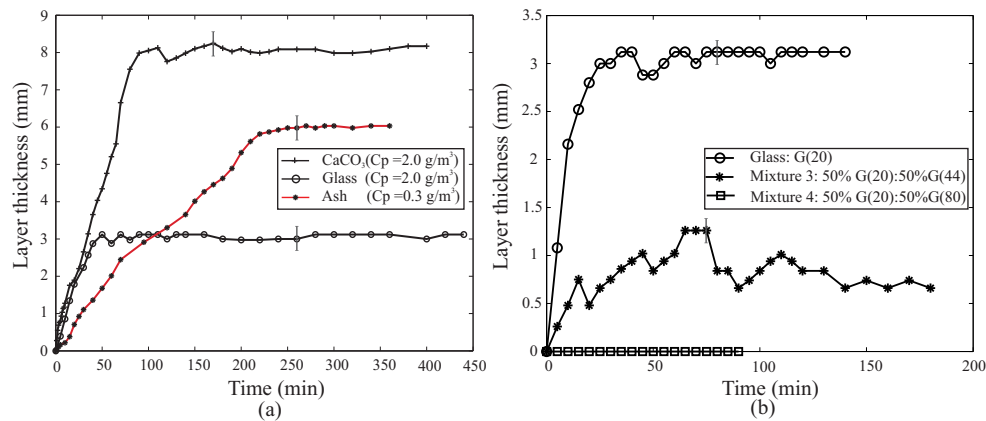


Figure 5.5: Changes in deposit layer thickness with time at gas velocity of 1.5 m/s for: (a) different foulant materials and (b) mixtures of glass particles of different mean diameters.

case are needle shaped and the interaction with a clean surface or a fouled surface is completely different from the other two particle types considered. As the density and material properties of the ash particles were unknown, a clear description of the transport and deposition mechanism is difficult to provide. Based on its shape and structure, it can be deduced that the velocity necessary to detach an ash particle from the surface is higher than for an equivalent sized spherical particle. Hence, if a particle reaches a surface, owing to its larger area of contact with the surface, the adhesion force is comparatively higher and the particle sticks.

The behavior of a mixture of glass and $CaCO_3$ particles can be seen in figure 5.2 (c). The layer that is formed over the cylinder is unstable and large portions of the layer collapse at certain intervals and the layer grows again. The process repeats and the asymptotic behavior as seen for glass or $CaCO_3$ cases is not observed. The reason for this behavior could be due to the structural instability of the layer due to the presence of spherical glass particles in a matrix of crystalline $CaCO_3$ particles.

Particles of different shapes have different packing characteristics. Regularly shaped particles (spherical glass particles in this case) have a better packing structure than a crystalline structure under random loose packing conditions. A random loose packing is a condition where particles settle when poured freely. It has been reported that the structure of a random loose packing is governed by the geometrical constraints which are related to the physical contact forces [34, 74]. The inter-particle friction that forms under packed conditions are thus dependent on the shape factor and for irregular geometries, the inter particle friction is relatively low as compared to regularly shaped particles and thus indicate structural instabilities. In the present case however, a strong coupling between flow features and particle deposition exists and this needs further investigation based on structural instability criterion and is not dealt in the present work.

Glass particles of two batches with different size were mixed in equal proportion by weight to study the effect of particle size distribution. Experiments were performed at 1.5 m/s with a particle concentration of 2 g/m^3 . The experiments correspond to the use of Mixture 3 and Mixture 4 (see table 5.1). Mixture 3 is a blend of two batches of glass particles with mean diameter of 20 and 55 μm . Mixture 4 is a blend of particle batches with mean diameter 20 and 80 μm . The particle size distribution of the resultant mixture was not analyzed. The experiment for glass particles with mean diameter 20 μm was repeated and compared with the mixtures. Figure 5.5 shows the influence of different particle size distribution in the flow. For mixture 3, it is seen that the presence of relatively bigger particles ($dp_{mean} = 54.5 \mu\text{m}$), results in a lower thickness of the fouling layer as compared to that of smaller particles. Also, the trend in the layer thickness for Mixture 3 indicates partial collapse of the layer frequently and a clear asymptotic behavior is not seen. The tube remained clean for Mixture 4. Abd-Elhady et al. [5] observed a similar behavior in their experiments with a mixture of relatively small copper particles ($dp_{mean} = 10 \mu\text{m}$) and bigger bronze particles ($dp_{mean} = 55 \mu\text{m}$). The critical sticking velocity of particles decreases with increasing particle size. Hence, smaller particles can more easily stick to a surface than bigger particles at a given velocity. Further, the critical flow velocity necessary to remove a small particle resting on a surface is much larger than that necessary to roll a bigger particle. Thus, at a given velocity, smaller particles tend to stick to the surface and larger particles at the same velocity have higher inertia due to their higher mass. When bigger particles strike a surface with any pre-deposited (small) particles, they can remove the smaller particles.

5.5 Influence of target geometry and orientation

5.5.1 Effect of tube size

At a given temperature, the Reynolds number based on the cylinder diameter as the characteristic dimension can be varied by changing the flow velocity and/or by changing the size of the cylinder. The effect of changing velocity for constant tube diameter was discussed in section 5.3.1. The deposition of glass particles on different tube dimensions is reported here. Glass particles [G(20)] were used in experiments and the velocity and particle concentration were held constant at 1.5 m/s and 2 g/m^3 , respectively. Stainless steel tubes with similar surface roughness values (RMS roughness values in the range $5\text{-}10 \mu\text{m}$) were chosen. The aim was to understand the deposition behavior under varying Reynolds and Stokes numbers. The particle Stokes number scales with the cylinder diameter and changes correspondingly. Figure 5.6 shows the deposition pattern over different tube diameters. The raw images correspond to the images obtained at the end of the experiment. Ta-

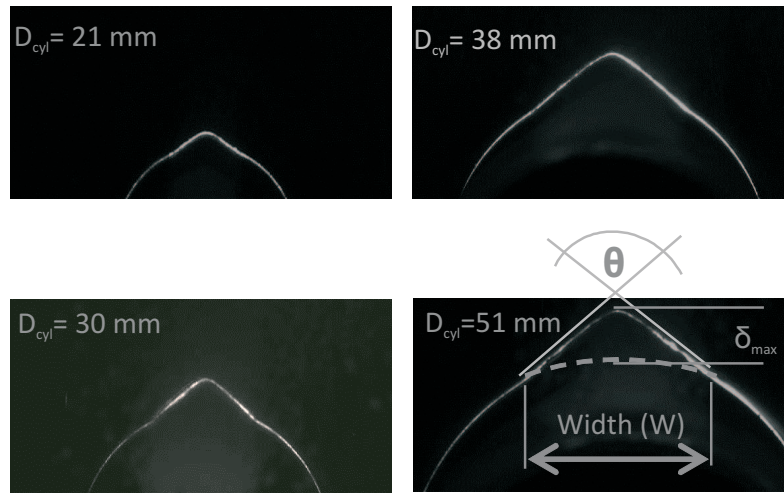


Figure 5.6: Pictures of glass particle deposit formed on stainless steel tube of varying diameters. Theta is the apex angle formed and W is the width of the layer on the cylinder. No deposit was found on the rear side of the cylinder.

ble 5.3 shows the ratio of layer thickness (δ_{max}) to width (W) along with the apex angle formed by the deposit layer. The ratio of the layer thickness to the width and the apex angle is similar for all the tubes indicating a constant pattern of deposit structure at the end of the experiments. For increasing diameter of the cylinder, the blockage ratio in the duct [ratio of duct dimension to the tube diameter] correspondingly changes. The variation in Reynolds number and blockage ratio changes the

Table 5.3: Deposit width, thickness and apex angle formed for the deposition of glass particles on tubes of different diameters.

$D(mm)$	$W(mm)$	$\delta_{max}(mm)$	$\theta(^{\circ})$	δ_{max}/W
21	6.5	1.62	117	0.249
30	12.3	3.3	115	0.268
38	20.3	5.4	116	0.266
51	31	8.3	118	0.267

wall shear stress acting on the cylinder wall and the overall boundary layer pattern on the cylinder. However, it is interesting to observe that although the flow features are affected, the deposition pattern seems to preserve its features.

The variation of deposit layer thickness with time is shown in figure 5.7. The time taken for the deposit to reach the asymptotic state is directly proportional to the tube size. The asymptotic layer thickness for varying Reynolds number is plotted

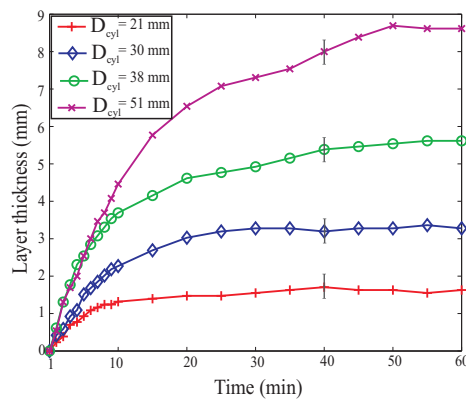


Figure 5.7: Changes in the deposit layer thickness with time for different tube diameters ($V_g = 1.5$ m/s, $C_p = 2$ g/m³).

in figure 5.8 (a). Glass particles with a mean diameter of $20 \mu\text{m}$ were used in the experiments and based on equation 2.3, the Stokes number for the particles can be evaluated. The Stokes numbers for different conditions are also indicated in figure 5.8 (a). The asymptotic layer thickness as a function of Stokes number is plotted in figure 5.8 (b). The experimental data points were curve fitted which follows a power law. The resulting equation and corresponding constants are indicated in figure 5.8 (b).

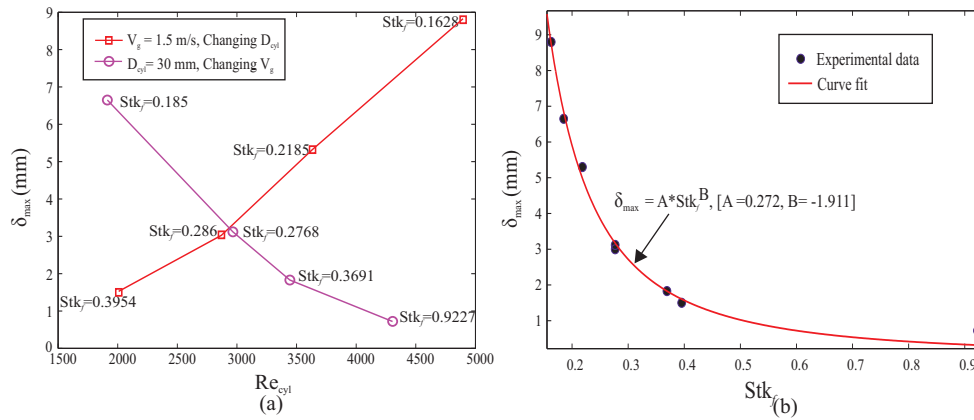


Figure 5.8: (a) Asymptotic layer thickness for varying cylinder Reynolds numbers with changing velocity and tube diameters; (b) Symbols denote the asymptotic layer thickness plotted against the Stokes number based on free stream velocity and tube diameter for G(20) particles. The solid line corresponds to a power law curve fit to the experimental data.

5.6 Effect of tube shape and orientation to the flow

To compare the deposition characteristics over a curved surface (circular cylinder) to that of a flat surface, a square aluminum cylinder of 40 mm width was chosen. The face of the tube was oriented at different angles to the flow direction as shown in figure 5.9. The axis of the tube was perpendicular to the flow direction. Experiments were performed with glass particles with a concentration of 2 g/m^3 and a velocity of 1.5 m/s. The tube was oriented at 0° , 15° , 30° and 45° to the flow direction. It was observed that the particle deposition invariably starts at the stagnation point and there was no deposition in the regions of high shear (near the edges). The deposition grows both outwards from the stagnation region and at the stagnation region. The maximum deposition is observed at the stagnation line and for increasing inclinations, the deposition reduces. The tube surface oriented at 45° to the flow remained clean. The experiments were also carried out with ash particles for the tube inclined at 45° ($V_g = 1.5 \text{ m/s}$, $C_P = 0.2 \text{ g/m}^3$) and a layer of deposit was formed over the inclined surface.

In another experiment, the axis of a circular tube was inclined at 30° to the flow direction as shown in figure 5.10. The tube remained clean for glass particles [G(20)] for a flow velocity of 1.5 m/s. Experiments performed with $CaCO_3$ at 1.5 m/s resulted in a small build up of the layer but for a flow velocity of 3 m/s, the tube remained clean again. For a tube which was not inclined, it was seen that at 1.5 m/s, the thickness of the $CaCO_3$ layer was about 8 mm and at 5 m/s the layer was 0.25 mm thick. However, for the inclined tube, fouling ceases at much lower velocities.

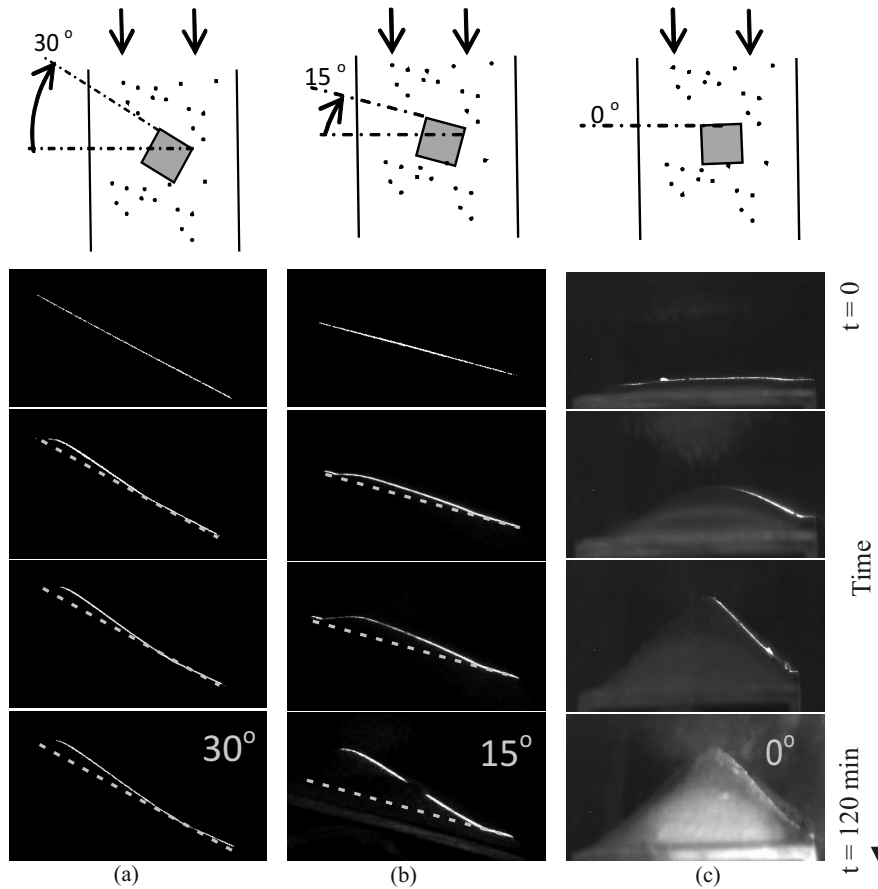


Figure 5.9: Deposit formation of glass particles over a square tube whose faces are rotated to various angles to the flow direction; (a) 30° (b) 15° (c) 0° . The axis of the tubes are perpendicular to the flow direction. The dotted lines represent initial clean tube which are inserted for reference.

If the particles are assumed to travel in a straight line from the top to the bottom, inclining the square tube introduces oblique impact of particles with the surface and is comparable to different positions on the curved surface of the circular. Similarly, inclining the circular tube to the flow direction introduces oblique impact in an additional dimension. During oblique impact, the tangential velocity of the particle is conserved and the critical sticking velocity for particle impact at oblique impact is considerably lower than the impacts which occur at normal incidence.

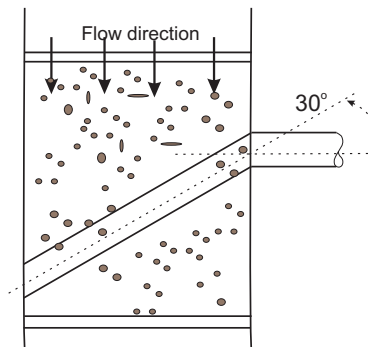


Figure 5.10: Schematic representation of a circular tube whose axis is inclined to the flow direction.

5.6.1 Three tubes in a row

Particles (with lower Stokes numbers) in the flow are governed by the flow dynamics. The wake formed behind a cylinder is associated with complex flow structures. To study the influence of flow structures on the deposition behavior, three cylinders ($D_{cyl} = 25\text{mm}$) were positioned in line with the flow direction with a longitudinal pitch of $2.5 \times D_{cyl}$ between the cylinder centers. Figure 5.11 shows a picture of the tubes and a schematic representation of the deposit structure formed on the tubes at the end of the experiment. CaCO_3 particles were seeded at 2 g/m^3 and the velocity of the flow was 1.5 m/s . The deposit formed on the top most cylinder was similar to the one found for the a single tube case. However, deposition was also observed on either side of the cylinder on the leeward side of the tube. The center tube and the bottom most tube displayed asymmetric deposition patterns. The deposition on the center tube was rather skewed towards the left side of the cylinder and the deposition on the third cylinder was skewed towards the right side, as shown in figure 5.11 (b). The layer growth of the center tube was monitored and the raw images of the initial and final stage are shown in figure 5.12 (a) and (c) respectively. Figure 5.12 (b) shows the processed image in which the evolution of the layer can be seen. It was observed that the radial thickness of the deposit formed on the tube was substantially larger than the experiments with a single tube.

For flows around cylinders, eddies are shed from each side of the cylinder generating vortices in an alternating fashion. Small particles which are in the turbulent wake of the flow inherit the flow characteristics and display complex unsteady motion which usually results in non-uniform spatial distributions. This can also lead to preferential concentration of particles in the shear zones between vortices. If the particle response time is larger than the typical turn over time for an eddy, the particle will not respond to the flow and thus will not gain the acceleration necessary to

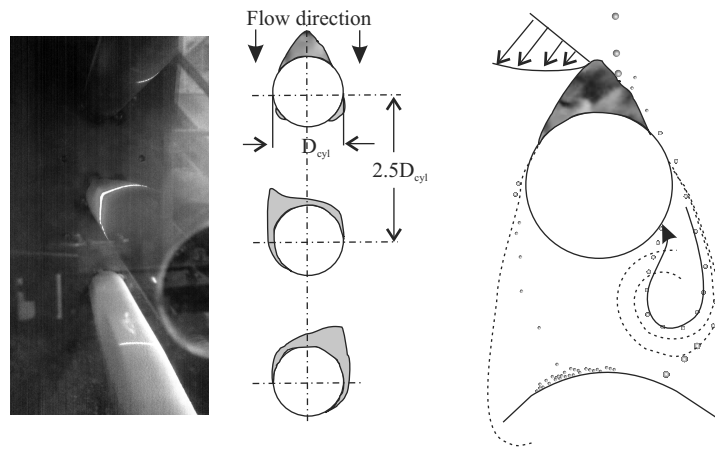


Figure 5.11: Deposition of calcium carbonate particles on a row of tubes. The left image is the picture taken during the experiments, the middle image schematically shows the final deposit layers formed over the cylinder after 90 minutes of operation and the right image shows the schematic of the fluid shear on the deposit layer and particle transport to the downstream cylinder.

impact on the rear side of the cylinder. For particles with very low response time, the eddy turn over time is too slow for the particles to gain acceleration in the direction towards the cylinder. Hence, the particles which have a response time similar to the eddy turn over time have higher probability to strike the cylinder on the leeward side. This explains the deposition pattern found on the rear side of the top most tube.

The skewed deposition pattern found on the center and bottom most tubes are mostly due to the complex flow features behind the cylinder. Due to the probable asymmetry in the arrangement of the tubes and random fluctuations in the flow, the vortices formed on the tube can interact with the downstream cylinder surface and can result in high complex flow structure. A comprehensive understanding of the phenomena calls for detailed numerical model which can describe the attachment and removal of the particle clearly which is the aim of the next chapter.

5.7 Effect of liquid layer

Fouling in heat exchangers strongly depends on the condensation rates of the vapor species on the heat exchanger surface. As the thickness of a fouling layer grows, the gas side surface temperature of the layer eventually reaches the same temperature as the gas phase and thus condensation due to the cooling tube stops. In most of the cases involving particulate fouling, the initiation period is a crucial phase and understanding the effect of condensation on the initiation and growth of fouling layers

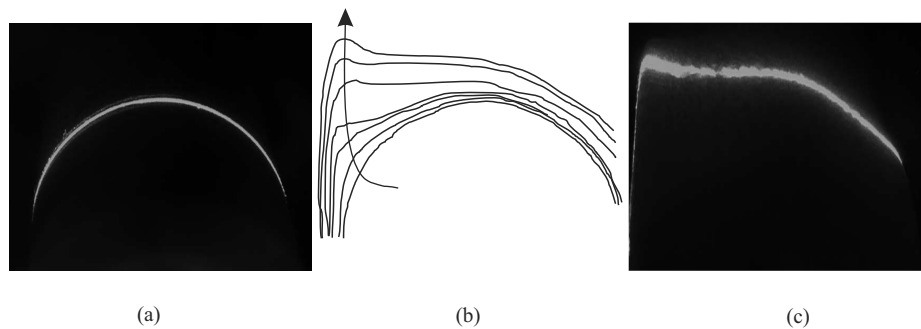


Figure 5.12: Deposit layer profile for the middle tube which was in a row of three tubes. (a) Before experiment, (c) Layer profile after the experiment (c) Processed image which indicates the evolution of the deposit layer.

provides vital information to understand and control the overall process.

Controlled fouling experiments were performed to evaluate the effect of the presence of a liquid layer due to condensation. To mimic the condensation, the deposition tube was coated with a thin layer of liquid of known viscosity. Figure 5.13 (a) shows the comparison of the deposition of ash particles on a dry and liquid (glycerol) coated tube. The gas phase velocity was 1.5 m/s and particle concentration was 0.2 g/m^3 . The inlaid pictures correspond to the processed images to capture the evolution of the fouling layer with time. Experiments performed with a liquid layer show a similar trend as that of dry deposition in the center line thickness. However, the initial rate of growth is much higher than for the dry deposition case. The liquid layer present captures almost all particles that reach the surface. The deposition of an initial layer provides more active sites for other particles to deposit and hence more particles deposit over the surface resulting in higher growth rates. The circumferential width of layer formed in the wet case is also larger and forms a shoulder kind of structure, thus changing the geometry of the layer which aids in particle deposition. The evolution and the final profile of the layers formed on a glycerol coated and a dry tube are shown in figure 5.13 (b) and (c) respectively. The effect of the liquid layer stops after a while and the layer growth follows a dry deposition pattern. At the end the apex angle formed on the top is similar to the one for the dry deposition case.

Experiments performed with glass particles [G(20)] at 1.5 m/s on dry and glycerol coated tubes display similar trends as for ash particle deposition (see figure 5.13). The deposition rate and the final thickness of the layer formed are higher for the wet deposition. The experiments were extended to higher velocities and at 3 m/s glass particles deposited on the liquid coated tube and formed a layer of 0.38 mm. However, the tube remained clean at 2.5 m/s under dry conditions.

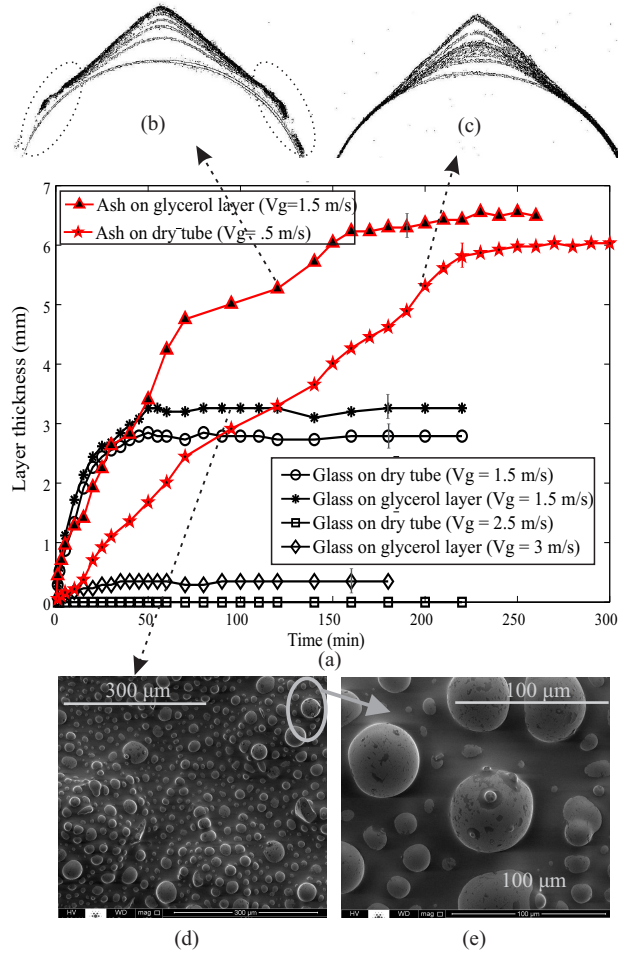


Figure 5.13: (a) Changes in the deposit layer thickness with time for dry and liquid coated surface for different foulant particles, (b) Deposit formation on a liquid coated cylindrical tube, (c) Deposit formation on a dry cylindrical tube, (d) and (e) SEM pictures of the particles collected after experiments for glass deposition on liquid coated tube.

Figure 5.13 (d) and (e) show the (SEM) images of the particles collected from the glass deposition [G(20)] experiment on a glycerol coated cylinder. The liquid present on the cylinder surface forms a matrix within which the glass particles deposit. It is also observed that smaller particles adhere on to the larger particles and if the smaller particles adhere to each other or bigger particles in the flow, it can agglomerate to form an effectively larger particle.

Experiments were performed with varying liquid viscosity and compared to dry

deposition of glass particles [$G(20)$, $V_g = 1.5$ m/s, $C_p = 2$ g/m³]. Figure 5.14 shows the variation of layer growth with time for different liquid coatings. The layer growth rate and the asymptotic thickness were observed to be directly proportional to the liquid viscosity.

Experiments were performed with bigger glass particles [$G(143)$] and the tube was covered with a thin film of liquid with comparatively lower viscosity [0.04 Pas], this resulted in the formation of a very thin deposit layer and was limited to stagnation zone on the cylinder. Further, an experiment with the tube inclined at 30° to the flow was conducted for glass particles [$G(40)$, $V_g = 1.5$ m/s, $C_p = 2$ g/m³] with a liquid layer to observe the effect of geometry under wet conditions. For similar parameters under dry conditions, a very thin deposit layer was observed at the stagnation region. However, for the wet case, the width of the deposit at the stagnation was comparatively larger but the thickness was similar to that of dry deposition case. The results for the inclined tube and bigger particles are not shown.

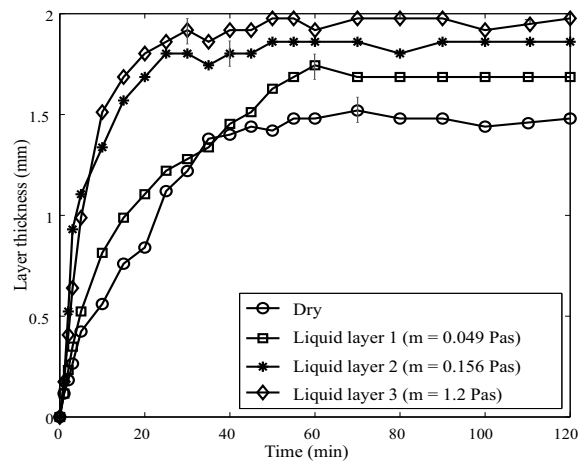


Figure 5.14: Changes in the deposit layer thickness with time for the deposition of glass particles on a cylindrical tube coated with liquids of different viscosities.

To quantify the differences between the dry and wet deposition cases, the mass of glass and $CaCO_3$ deposited on the surface of the cylinder was measured for different time intervals. The measurement method was similar to the one discussed earlier. A PVC tube of 25 mm outer diameter, 22 mm inner diameter and a length of 22 mm was mounted concentrically on another tube of outer diameter 22 mm. The PVC tube served as the deposit probe to collect the particles. The tube was weighed with a jewelers precision weighing machine before and after the experiments (tube + particles). A similar procedure was adopted for the liquid coated tubes. By measuring the weight of the tube before and after deposition, the mass of the particles deposited during a certain time interval was obtained and the data is plotted in fig-

ure 5.15 (a) and (b). Comparing the deposition for dry and wet cases, it is seen that

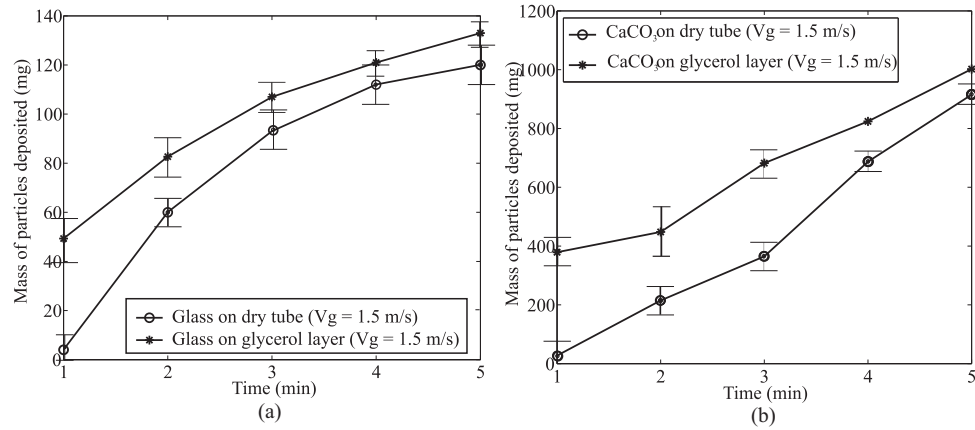


Figure 5.15: Comparison of the mass of particles deposited for dry and liquid (glycerol) coated tube. (a) Deposition of glass particles (b) Deposition of calcium carbonate particles.

for both glass and $CaCO_3$, the mass of particles deposited in the wet case is higher than the one for the dry deposition case. It is clearly observable that most of the increase in the deposition happens in the first few minutes of operation and for later stages the gap between the dry and wet curves closes in. At later stages, the initial layer which has been formed grows and the interaction of the incoming particle with that of the deposited particles show dry deposition behavior.

5.8 Conclusions

A phenomenological study of the influence of various factors on particulate fouling was conducted. The measuring technique was focused on gaining information on the deposition of particulate matter and to quantify the dynamics of the layer growth. Some of the important points which can be highlighted are:

- The gas velocity was found to have a very strong influence on the overall deposition process for both dry and wet conditions. For dry deposition, the asymptotic fouling thickness was found to be inversely proportional to the square of the Stokes number (Stk_f).
- Experiments performed at higher temperatures indicated the importance of particle properties on the deposition process.
- The geometry of the tube is an important parameter which influences deposition to a large extent by reducing the critical sticking velocity for the particles.

Thus, as the particle deposits on a surface and forms a layer, the geometry changes which in turn changes the flow field. As the layer geometry changes, the critical sticking velocity changes and lowers the number of particles that deposit.

- The presence of a liquid layer enhances particle deposition. The difference in mass of particles collected for wet deposition after 1 minute indicated an increase of 92% as compared to the dry deposition mass collected after the same time. Based on the Stokes number (as discussed in chapter 2 and 3), the sticking probability and the erosion characteristics can be determined.
- By altering the tube orientation, it was observed that the limiting velocity for fouling reduced drastically. It is also seen that the particle collision dynamics governs the deposition mechanism to a large extent. A detailed numerical model which captures the particle collision and removal dynamics will aid in better design procedures to minimize fouling.

Numerical simulations

In chapter 2, a two body collision model as used by Van Beek [62] was presented along with a model for particle impaction on liquid coated substrates. The modeling approaches of critical viscosity and melt fraction has been widely used for modeling slagging and fouling in high temperature sections. However, as discussed earlier, the critical velocity approach offers a better way to model particulate deposition for powdery layers and to understand the effect of erosion along with the presence of thin liquid films. The present chapter describes a preliminary modeling approach for dry particulate fouling along with the implementation methodology to capture the influence of a thin liquid film on a substrate using a commercial CFD package (FLUENTTM). A 2-dimensional circular cylinder in a cross-flow is considered and the influence of gas phase velocity, geometry and the presence of a liquid film is demonstrated. The study is further extended to square cylinders at different orientations to the flow and a qualitative comparison is made to the experimental observations as discussed in chapter 5.

6.1 Flow field and particle trajectory calculations

Fluid flows concerning more than one phase are labeled as multiphase flows. The ash particles in the flue gas represent a typical two phase dispersed flow. Generally either an Eulerian one fluid model or an Eulerian-Lagrangian approach is used to model multiphase systems. The details of different approaches along with their advantages and applicability can be found in several text books on multiphase flows. In the present work, an Eulerian-Lagrangian approach is used as the method allows one to calculate forces acting on the particles explicitly and determine the particle velocity, position, rotation etc, which are relevant for the present study.

For typical heat recovery boilers the Reynolds number based on the tube size ranges from 2000 to 20000 [62]. The flow around a cylinder in a cross flow for the range of Re specified is said to be sub-critical as the boundary layer develops upstream at the stagnation point and is laminar. However, flow on the leeward side of the cylinder is turbulent owing to the flow detachment and eventual vortex shedding process. It has been reported that the flow in a tube bundle exhibits the same features as for a single cylinder in cross flow [62] and the present work is mainly focused on modeling particle deposition on a single cylinder in a cross flow. A commercial CFD package is used for the numerical implementation and analysis.

6.1.1 Flow equations

The dynamical behavior of a fluid is governed by the Navier-Stokes equation. Disregarding the energy equation, the momentum and continuity equations are given as:

$$\rho \left\{ \frac{\partial \tilde{u}_i}{\partial t} + \tilde{u}_j \frac{\partial \tilde{u}_i}{\partial x_j} \right\} = -\frac{\partial \tilde{P}}{\partial x_i} + \frac{\partial \tilde{T}_{ij}}{\partial x_j} \quad (6.1)$$

$$\left\{ \frac{\partial \tilde{\rho}}{\partial t} + \tilde{u}_j \frac{\partial \tilde{\rho}}{\partial x_j} \right\} + \tilde{\rho} \frac{\partial \tilde{u}_j}{\partial x_j} = 0 \quad (6.2)$$

where \sim indicates instantaneous values and the subscripts indicate tensorial notation. T_{ij} is the viscous stress tensor, P is the pressure term, u is the velocity and ρ is the density.

For incompressible flows, $\frac{\partial \tilde{\rho}}{\partial t} = 0$ and $\frac{\partial \tilde{\rho}}{\partial x} = 0$, Thus, the continuity equation takes the form:

$$\frac{\partial \tilde{u}_j}{\partial x_j} = 0 \quad (6.3)$$

For Newtonian fluids the viscous stress tensor reads:

$$\tilde{T}_{ij} = 2\mu \left\{ \tilde{S}_{ij} - \frac{1}{3} \tilde{S}_{kk} \delta_{ij} \right\} \quad (6.4)$$

where the instantaneous strain rate tensor is defined as:

$$\tilde{S}_{ij} = \frac{1}{2} \left\{ \frac{\partial \tilde{u}_i}{\partial x_j} + \frac{\partial \tilde{u}_j}{\partial x_i} \right\} \quad (6.5)$$

and δ_{ij} is the Kronecker's delta which defined such that $\delta_{ij} = 1$ if $i = j$ and $\delta_{ij} = 0$ otherwise.

Thus, the stress tensor takes the form:

$$\tilde{T}_{ij} = 2\mu \tilde{S}_{ij} \quad (6.6)$$

Reynolds decomposition

The instantaneous quantities $\tilde{\phi}$ can be considered to be a fluctuating part ϕ' superimposed on the mean value $\bar{\phi}$ which is called as Reynolds decomposition. i.e:

$$\tilde{\phi} = \bar{\phi} + \phi' \quad (6.7)$$

The Reynolds Averaged Navier Stokes equations (RANS) are obtained by substituting $\tilde{u}_i = U_i + u_i$, $\tilde{P}_i = P_i + p_i$ and $\tilde{T}_{ij} = T_{ij} + \tau_{ij}$. For simplicity, the capital letters correspond to the mean values and the lower case letters correspond to the fluctuating part. After averaging, the momentum equation reads:

$$\frac{\partial U_i}{\partial t} + U_j \frac{\partial U_i}{\partial x_j} = -\frac{1}{\rho} \frac{\partial P}{\partial x_i} + \frac{\partial}{\partial x_j} [T_{ij} - \rho \overline{u_i u_j}] \quad (6.8)$$

Equation 6.8 has the same form as the fundamental momentum equation. However, the velocities now represent the time averaged values and the effects of turbulence is implemented through the Reynolds stresses ($\rho \overline{u_i u_j}$). Reynolds stresses are not stress terms per se, but are the reworked terms of the fluctuating contribution of non-linear acceleration terms and are symmetric, second order tensors having six components. Thus, RANS equations yield 6 stresses, 3 velocities and 1 pressure term. As the number of unknowns are more than the available equations (3 momentum and 1 continuity equation), closure relations are sought to close the non linear system of equations. A so called "turbulence model" provides closure relations in terms of known mean flow quantities.

RANS models are mainly divided into two categories: RANS-Eddy Viscosity Models (EVM)s and Reynolds Stress Models (RSM). RANS-EVMs are based on the assumption that the Reynolds stresses are proportional to the mean velocity gradients (with turbulent viscosity being the proportionality constant). RSM models can be of differential type, algebraic (ARSM) or explicit algebraic (EARSM) type. The RANS model used in the present study with relevance to particle tracking and deposition is discussed in the next section.

6.1.2 Particle dispersion and transport in a turbulent flow field

In a turbulent flow field, FLUENT predicts the particle trajectories using the mean velocity of the fluid and the instantaneous fluctuating velocities to predict the dispersion of the particles due to turbulence. FLUENT offers two models: a Particle Cloud tracking model and a stochastic Discrete Random Walk (DRW) model. The particle cloud model tracks the statistical evolution of a cloud of particles about a mean trajectory and the concentration of the particle within the cloud is represented by a Gaussian probability density function about the mean trajectory. The cloud model is usually implemented to analyze spray evolution.

The DRW model includes the effect of instantaneous turbulent velocity fluctuations on the particle trajectories through the use of stochastic methods. The model assumes that the particles encounter discrete turbulent eddies successively one after the other. Each eddy is characterized by a random velocity fluctuation determined by a Gaussian distribution and by the eddy time scale. The characteristic lifetime of an eddy can be taken as a constant or as a random variation around a fluid Lagrangian integral time scale T_L as:

$$\tau_e = -T_L \ln(r) \quad (6.9)$$

where r is a uniform random number between 0 and 1 and T_L is the fluid Lagrangian integral time generally approximated as:

$$T_L = C_L \frac{k}{\epsilon} \quad (6.10)$$

where C_L is a model constant which is determined by matching the diffusivity of tracer particles to the scalar diffusion rate predicted by the turbulent model. In addition to the eddy life time, an eddy cross over time is defined by the relation:

$$t_{cross} = -\tau \ln \left\{ 1 - \left[\frac{L_e}{\tau |u - u_p|} \right] \right\} \quad (6.11)$$

where τ is the particle relaxation time, $|u - u_p|$ is the magnitude of the relative velocity between fluid and particle, and L_e is the eddy length scale. The particle is assumed to interact with the fluid phase eddy over the smaller of the eddy lifetime and the eddy crossing time [6].

A turbulent eddy is characterized by the time scale τ_e and the random velocity fluctuation u_i . The values of u_i that prevail during the lifetime of the turbulent eddy are sampled by assuming that they obey a Gaussian probability distribution, such that

$$u_i = \zeta \sqrt{u_i^2} \quad (6.12)$$

where ζ is a normally distributed random number. For the widely used RANS-EVMs, especially the $k-\epsilon$ and $k-\omega$ models and its variants, the local RMS fluctuating components are deduced assuming isotropy and are given as:

$$\sqrt{u^2} = \sqrt{v^2} = \sqrt{w^2} = \sqrt{2k/3} \quad (6.13)$$

However, the flow in the boundary layer is non-isotropic where the wall normal and span-wise fluctuations are usually smaller than the tangential component of fluctuations. Thus, while sampling fluctuations from the local kinetic energy, a relatively large fluctuation is sampled in the wall normal direction and a relatively small value is obtained for the tangential component. This leads to over-prediction of particle deposition rates as the model cannot provide information on the near wall anisotropy.

Dhebi [24] investigated dispersion of particles in 90° bends and suggested modifications to the rms fluctuating velocities in the boundary layer with DNS data for channel flow. The modified equations provided better results as compared to the default models. A similar modification was adopted by Van Beek [62] to avoid over-estimation of particle deposition.

The RSM model closes the RANS equations by solving the transport equations for the Reynolds stresses together with an equation for the dissipation rate. The model completely abandons the isotropic eddy-viscosity hypothesis. Also, RSM model is most suitable to predict normal stresses as it can selectively damp the stresses due to curvature effects, buoyancy etc [6]. In a detailed study of particle deposition in turbulent duct flows, Tian and Ahmadi [59] compare the $k-\epsilon$ and the RSM model offered by FLUENT and conclude that the RSM model which accounts for anisotropy, provides a more accurate description of the turbulent flow field near the wall. With the use of an RSM model and the 'two-layer zonal' boundary condition, they report that the Fluent code leads to reasonable results for the deposition of nano and sub-micrometer particles. Further, it is reported that the deposition rate of particles with inertial transport, the effects of turbulence on deposition is less, and hence is less sensitive to the modeling accuracy. In the present work, the standard RSM model is used to obtain the flow field and the DRW model of FLUENT is used for particle tracking. The details of the implementation of the RSM model is not discussed here for brevity, but can be found in the theory guide of Fluent and the references therein.

6.1.3 Validation of flow model

In order to evaluate the flow model, the skin friction coefficient and the angle at which flow separation occurs over the cylinder is compared with experimental data of Son and Hanratty [50]. Experimental data were reported for two conditions: one with a splitter plate on the leeward side of the cylinder whose leading edge was placed at a distance equal to the cylinder diameter from the cylinder center and a configuration without a splitter plate. Figures 6.1 (a) and (d) schematically show the corresponding numerical domain used for the comparison. Van Beek [62] had earlier used a low-Re $k-\epsilon$ model using a domain similar to figure 6.1 (a). The presence of the splitter plate prevents the oscillatory movement of the wake behind the cylinder and results in a quasi-stationary flow field of the wake. The domain described in figure 6.1 (d) corresponds to the condition without a splitter plate as a symmetry boundary condition is not used at the cylinder axis. A structured mesh was used around the cylinder and a two-layer zonal wall model was used to calculate the near wall flow field. The wall treatment requires at least 10 cells in the buffer zone and the viscous sub layer and thus, the mesh resolution was maintained fine. The structured grid used is depicted in figures 6.1 (b) and (c). Based on the pressure coefficient, a grid independence study was conducted initially, and a solution independent grid was used for further studies. A PISO pressure-velocity coupling was used and sec-

ond order upwind scheme was implemented for the convective terms. A Dirichlet boundary condition was applied at the inlet and a homogeneous Nuemann boundary condition was used at the symmetry boundary except for the velocity component parallel to the boundary faces. A pressure outlet condition was set at the outlet. The experimental data for skin friction coefficient was used to validate the model which is given by the relation:

$$C_f = \frac{\tau_w Re^{0.5}}{\rho_g U_\infty^2} \quad (6.14)$$

The numerical prediction of skin friction coefficients for the two cases mentioned are compared to the experimental results which are shown in figure 6.2. It is seen that the model predictions are in good agreement with the experimental results and predict the flow separation point quite well. At the rear stagnation point at 180° , the values tend to zero which deviates from the experimental data but the overall predictions are within agreeable limits.

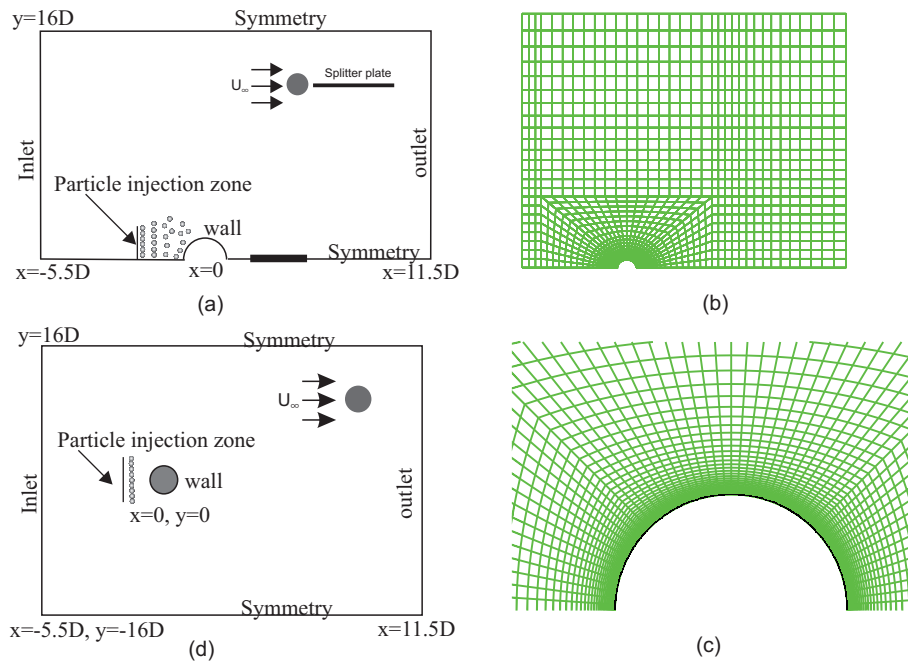


Figure 6.1: Schematic description of the domain used to validate the flow model; (a) Condition similar to the presence of a splitter plate; (b) Grid used for the calculations; (c) closer view of grid resolution at the cylinder wall; (d) condition similar to absence of a splitter plate.

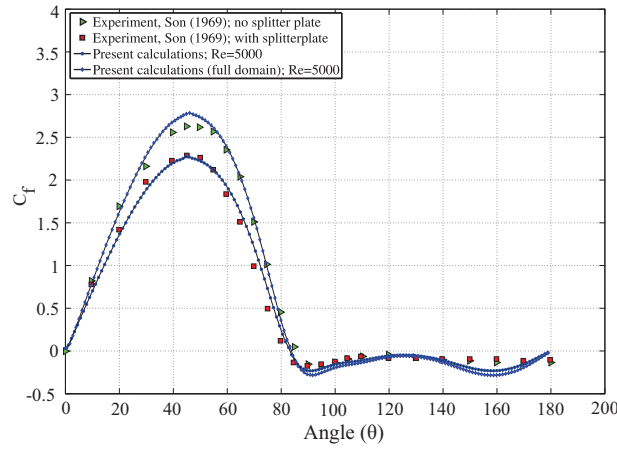


Figure 6.2: Comparison between experimental data and numerical results for the Skin friction coefficient at $Re = 5000$.

6.1.4 Validation of particle transport model

As a benchmark case, Van Beek [62] studied particle deposition on a circular cylinder assuming perfect sticking for the particles that reach the cylinder surface. The flow field was solved with a modified $k-\epsilon$ model to account for the anisotropy in the boundary layer. The model was validated against the experimental and DNS data of Bailer [8]. As a preliminary step, a test case was setup similar to the one studied by Van Beek [62]. However, the domain as shown in figure 6.1 (d) was used. To get a reasonable scaling, 60000 particles were injected from a distance $3 \times D_{tube}$ upstream and the particles were injected equidistant from each other over a distance of $1.2 \times D_{tube}$. A perfect sticking condition was assumed over the cylinder wall, i.e. all particles that reach the surface will stick and the drag force alone was considered during particle tracking. The simulations were done at a Reynolds number of 1900 and for various Stokes numbers (Stk_f). The deposition rates are expressed in terms of a Stanton number given by the relation:

$$St(\theta) = \frac{\phi(\theta)}{C_{p,d}U_\infty} \quad (6.15)$$

where $\phi(\theta)$ is the mass flux of the depositing particles, $C_{p,d}$ the particle concentration in the gas and U_∞ the free stream velocity of the gas. The mass flux and concentration can also be interpreted directly using the number of particles deposited and the number of particles in the gas. The collection efficiency of the cylinder is defined in terms of an averaged deposition rate scaled to the projected area of the cylinder. The collection efficiency is given by:

$$\eta_{col} = \pi \overline{St}_{0-2\pi} \quad (6.16)$$

where $\overline{St}_{0-2\pi}$ is the average Stanton number. Figure 6.3 shows the comparison of

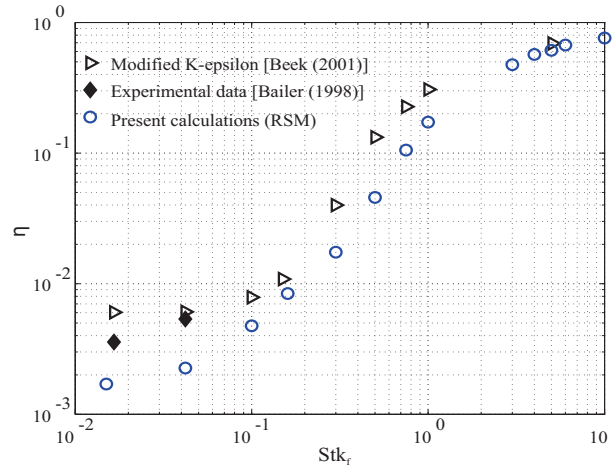


Figure 6.3: Comparison of RSM model with the modified K-epsilon model for particle deposition on a circular cylinder in cross flow for various Stokes numbers, $Re = 1900$.

collection efficiency for the present numerical calculations and experimental results of Bailer [8] along with the modified $k-\epsilon$ model of Van Beek [62]. As mentioned earlier, the $k-\epsilon$ model over-predicts particle deposition and needs corrections for the fluctuating velocity components. However, in the RSM model, the assumption of isotropy is abandoned and the Reynolds stresses are calculated explicitly. It is seen from figure 6.3 that the collection efficiency for the Reynolds stress model is lower as compared to earlier results. The difference narrows for larger Stokes numbers which indicates that the particle inertial mechanism dominates the process. At lower Stokes numbers, the velocity field highly influences the particle motion which highlights the importance to use a proper numerical model to obtain the flow field.

6.2 Removal model for dry particulate fouling

A dry particle which adheres to a surface can be removed by the forces induced by the fluid medium or due to particle impacts. A fluid medium can cause a particle which is resting on a surface to slide, to lift off or to roll over the surface as shown in figure 6.4. Particles which are spherical can be detached from the surface either by a rolling moment or due to lift forces acting on the particles as shown in figure 6.4 (a). However, for particles which are non-spherical, the dominant mechanism is the sliding motion as shown in figure 6.4 (b). The presence of roughness or other smaller particles which strongly adhere to the surface can offer considerable resistance to the rolling of the spherical particle which is shown in figure 6.4 (c). A non-spherical, ir-

regularly shaped particle resting over a surface is depicted in figure 6.4 (d) for which the primary mechanism of removal is difficult to establish. In most of the practical cases, the particles are randomly shaped and usually for simplification in numerical modeling, the particles are assumed to be of spherical shape which provides a descriptive behavior of other irregularly shaped particles.

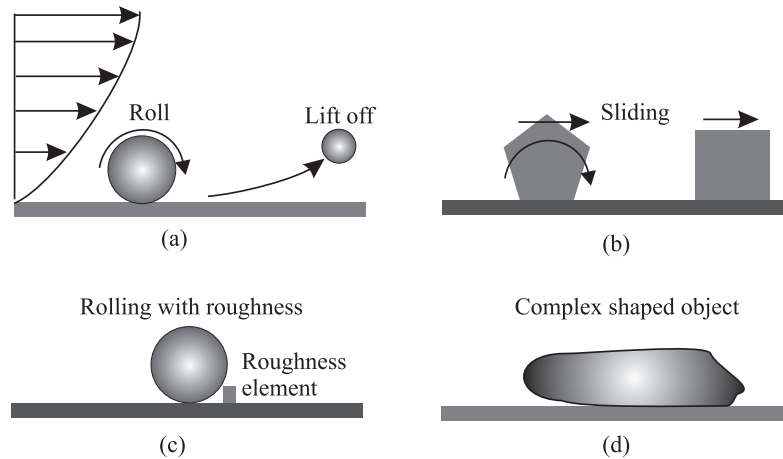


Figure 6.4: Possible modes of particle removal due to shear.

Yiantsios and Karabelas [71] studied the adhesion and detachment of spherical glass particles on a flat glass substrate dispersed in a liquid medium and found that the hydrodynamic force necessary to detach a particle was dependent on the pH of the solution and on the particle size. Larger particles could be easily removed and higher hydrodynamic forces were necessary to detach a small particle. Burdick et al. [17] considered the different modes of particle detachment as mentioned above and proposed a critical particle Reynolds number as a detachment criterion for each mode when the roughness of the surface is negligible. They also treated the detachment criteria analytically for rough surfaces based on the point of fulcrum about which a particle begins to roll. Among the sliding, lift off and the rolling modes, they found that the rolling mode was the primary one for particle detachment. In a similar study Zoetewij et al. [73] experimentally investigated particle detachment in a linear shear flow and established that the force necessary to roll a spherical particle was much less than other modes. Abd-Elhady et al. [2] implemented the model proposed by Zhang et al. [72] to describe the removal of particles due to shear forces which is valid for spherical non-charged particles. A critical flow velocity which causes a particle resting on a flat surface to roll was defined based on the ratio of the hydrodynamic rolling moment (HRM) and the adhesion resting moment (ARM). In the present work, a simple model for the removal of particles due to shear alone is

considered.

For a particle of radius r_p resting on an inclined surface which is exposed to a shear flow, d is the particle deformation diameter and δ is the deformation due to the surface adhesion force and the applied load L on the particle as shown in figure 6.5. The particle deformation is given by:

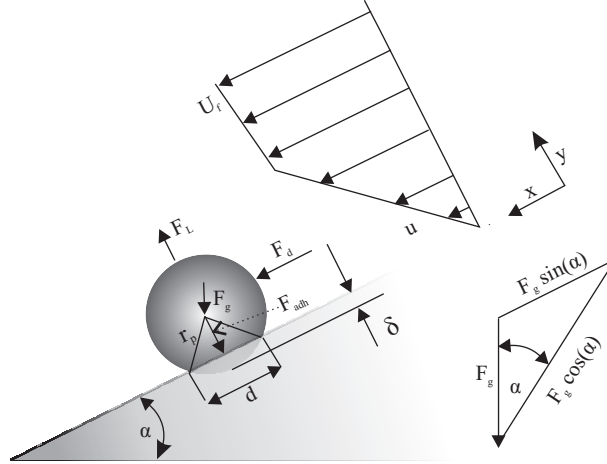


Figure 6.5: Schematic of a particle resting on an inclined flat surface and subjected to different forces. [30]

$$\delta = r_p - \left(r_p^2 - \frac{d^2}{4} \right)^{0.5} \quad (6.17)$$

The particle contact diameter is given by the standard JKR model as:

$$d^3 = \frac{6r_p}{E^*} (L + 3\pi\Gamma r_p + (3\pi\Gamma r_p L + (3\pi\Gamma r_p)^2)^{0.5}) \quad (6.18)$$

where E^* is the effective Young's modulus defined in chapter 2 (equation 2.11) and Γ is the surface adhesion energy. The load L acting on the particle is given by:

$$L = F_g \cos(\alpha) - F_L - F_b \quad (6.19)$$

α being the inclination angle of the surface to the horizontal, F_b and F_L are the buoyancy and lift forces acting on the particle, respectively.

The lift force is given by the relation:

$$F_L = 0.608 \frac{\rho^2}{\mu} (r_p U^*)^3 \quad (6.20)$$

where μ is the dynamic viscosity and ρ is the density of air. U^* is the wall friction velocity which is defined by:

$$U^{*2} = \frac{\mu}{\rho} \left. \frac{du}{dy} \right|_{(y=0)} \quad (6.21)$$

where du/dy is the velocity gradient normal to the surface. The velocity profile is assumed to be linear in the boundary layer thickness and the velocity gradient normal to the surface is derived from the linear relationship.

The gravitational force is given by:

$$F_g = \frac{4}{3} \pi r_p^3 \rho_p g \quad (6.22)$$

where ρ_p is the density of the particle and g is the gravitational acceleration.

The buoyancy force is defined as:

$$F_b = \frac{4}{3} \pi r_p^3 \rho g \quad (6.23)$$

The drag force is assumed to act at a distance $1.339 r_p$ and is given by the relation:

$$F_d = C_d \frac{\rho}{2} u_c^2 \pi r_p^2 \quad (6.24)$$

where u_c is the flow velocity at a distance from the surface equal to the radius of the particle, C_d is the drag coefficient and is given as

$$C_d = 24/Re_p \quad 0 < Re_p < 20 \quad (6.25)$$

$$C_d = 1.22 \quad 20 < Re_p < 400 \quad (6.26)$$

which depends on the particle's Reynolds number Re_p

$$Re_p = \frac{2r_p \rho u_c}{\mu} \quad (6.27)$$

The particle adheres to the surface with an adhesion force given by:

$$F_{adh} = \frac{3}{2} \pi \Gamma R^* \quad (6.28)$$

A particle rolls over the surface if the rolling moment overcomes the adhesion resting moment. Thus, if $RM > 1$, rolling occurs where RM is given by the relation [72]:

$$RM = \frac{HRM}{ARM} = \frac{F_d(1.399r_p - \delta)}{(F_a + F_g - F_b - F_L)0.5d} \quad (6.29)$$

In the present work, as only spherical particles are considered, the rolling moment model is implemented to evaluate particle removal. Figure 6.6 shows the implementation scheme for the combined deposition and removal model.

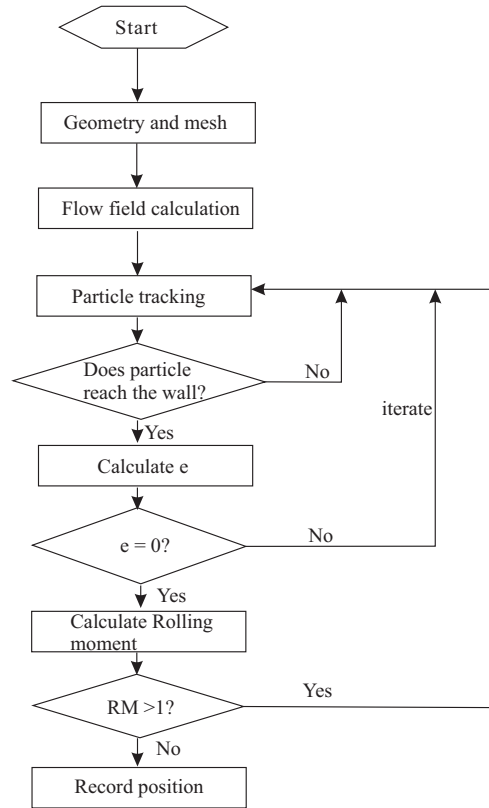


Figure 6.6: Flow chart for the implementation of dry deposition and removal model.

6.3 Particle deposition based on Roger and Reed model

The particle trajectories are evaluated based on the flow field, and when a particle reaches the wall of the cylinder, the Rogers and Reed model [44, 62] is invoked to evaluate whether the particle sticks to the wall or rebounds as described in chapter 2 [equation 2.6]. For particles that stick to the wall, the position where the particle deposits is recorded and the trajectory calculations are suspended. For particles which rebound, the trajectory calculations are progressed with an initial velocity equal to that of the predicted rebound velocity. Figure 6.7 shows the domain similar to the experimental conditions (chapter 5) which was chosen to study particle deposition and will be the reference domain for further discussions. The width of the channel was 0.2 m and based on a cylinder diameter of 25 mm, the inlet was located at 20 times the cylinder diameter and the outlet was positioned $40 \times D$.

The deposition of Sodium Chloride and Potassium Sulphate particles was studied at a Reynolds number of 2000 and 5000 respectively. The corresponding Stokes num-

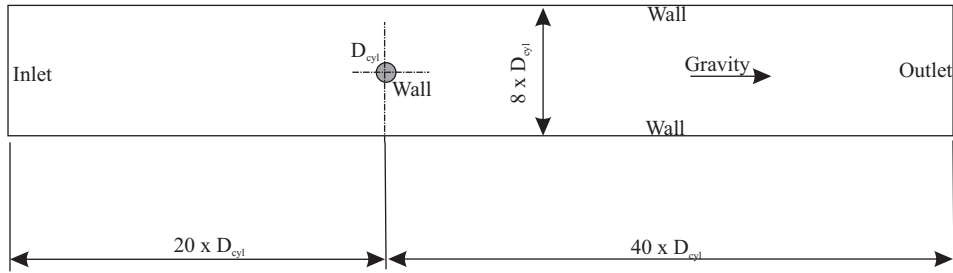


Figure 6.7: Domain used for deposition modeling which is similar to the experimental conditions for controlled fouling experiments. Note that the gravity is pointed towards the outlet which is same as the downwards motion of fluid and particles as in the experiments.

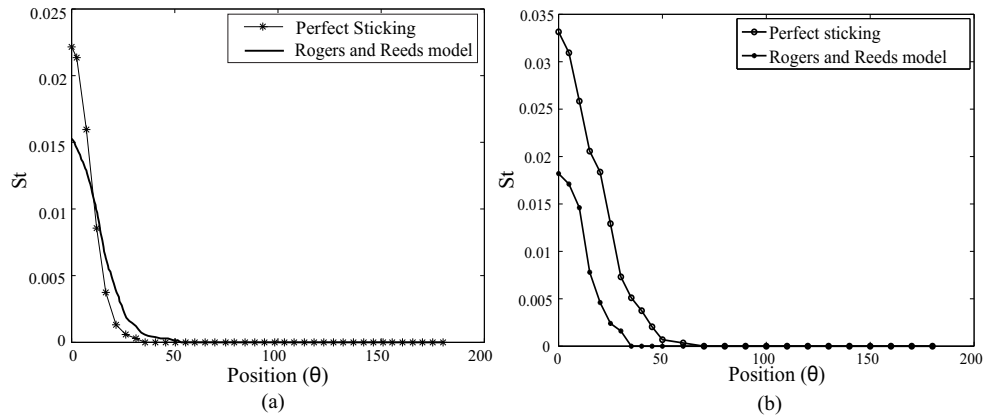


Figure 6.8: Comparison of perfect sticking and the prediction of Rogers and Reed model for: (a) NaCl particles depositing on stainless steel tube, $Re = 2000$, $Stk_f = 0.15$ and (b) K_2SO_4 particles depositing on stainless steel tube, $Re = 5000$, $Stk_f = 0.1$.

bers are 0.15 and 0.1 respectively. Figure 6.8 (a) shows the difference in particle deposition for a perfect sticking case and the implemented model for Sodium Chloride particles. The gravitational term is taken into account in the simulations and it is observed that there is no particle deposition on the leeward side of the cylinder. It can be observed that the sticking probability for the particles is reduced due to the rebound behavior as compared to the perfect sticking case. Further, the angular position of the deposit formation using the sticking model is found to be greater than the perfect sticking case. This is attributed to the secondary and tertiary rebounds of the particles and its subsequent sticking. The deposition behavior of Potassium Sulphate particles at $Re = 5000$ is shown in figure 6.8 (b). The difference between perfect sticking and the implemented model is quite evident and, in this case, the angular

position of particle deposition is less than for the perfect sticking case. However in both cases, the shape of the fouled layer is preserved as in the perfect sticking case.

6.3.1 Influence of gas phase velocity

In chapter 5, the experimental observations indicated a strong influence of gas phase velocity on the dry particle deposition behavior of particles over a circular cylinder. To qualitatively evaluate the numerical model, 60000 particles were injected in the flow field which was solved under steady state conditions for the domain shown in figure 6.7. Glass and $CaCO_3$ particles with a diameter of 20 μm and 40 μm respectively were used. The relevant material properties are listed in table 6.1. The number of particles (N_p) that deposit on the cylinder and the angular position (θ) of the deposit location are evaluated. Figure 6.9 shows the deposition behavior for Calcium Carbonate particles for various free stream gas velocities. The corresponding Reynolds number based on cylinder diameter and the Stokes numbers for the particles in the flow is shown in the figures which indicate the first layer of deposit formation.

Table 6.1: Material properties for different particles and tube.

Material	ρ (kg/m^3)	$E \times 10^9$ N/m^2	ν	$Y \times 10^8$ N/m^2	γ (J/m^2)
Steel	7800	215	0.28	20	0.09
Glass	2470	50	0.27	20	0.07
NaCl	2163	24.8	0.25	2.6	0.32
$CaCO_3$	2710	70	0.3	4	0.23
K_2SO_4	2665	30	0.3	4.1	0.25

It is seen that the model predicts maximum deposit formation for the lowest velocity of 0.5 m/s. The angular position of the deposit is between 0° to 80° and is approximately symmetric on both sides of the stagnation point (0°). The maximum deposit is at the stagnation point for all cases. For increasing velocity, the surface over which the particles deposit reduces along with the number of particles that deposit. At certain angles beyond the stagnation point, spikes are observed for some cases and the trajectories indicate secondary or sometimes even tertiary impacts of a particle. At a first instant a particle that rebounds is taken back to the cylinder but with a lower velocity and hence has a higher probability to stick in the second collision.

The deposit formation for glass particles is shown in figure 6.10. A similar trend of reduction in the number of particles and the surface area over which the particles deposit with increasing velocity is observed. As discussed in chapter 5, the experiments indicated that calcium carbonate particles formed a thin layer of deposit at

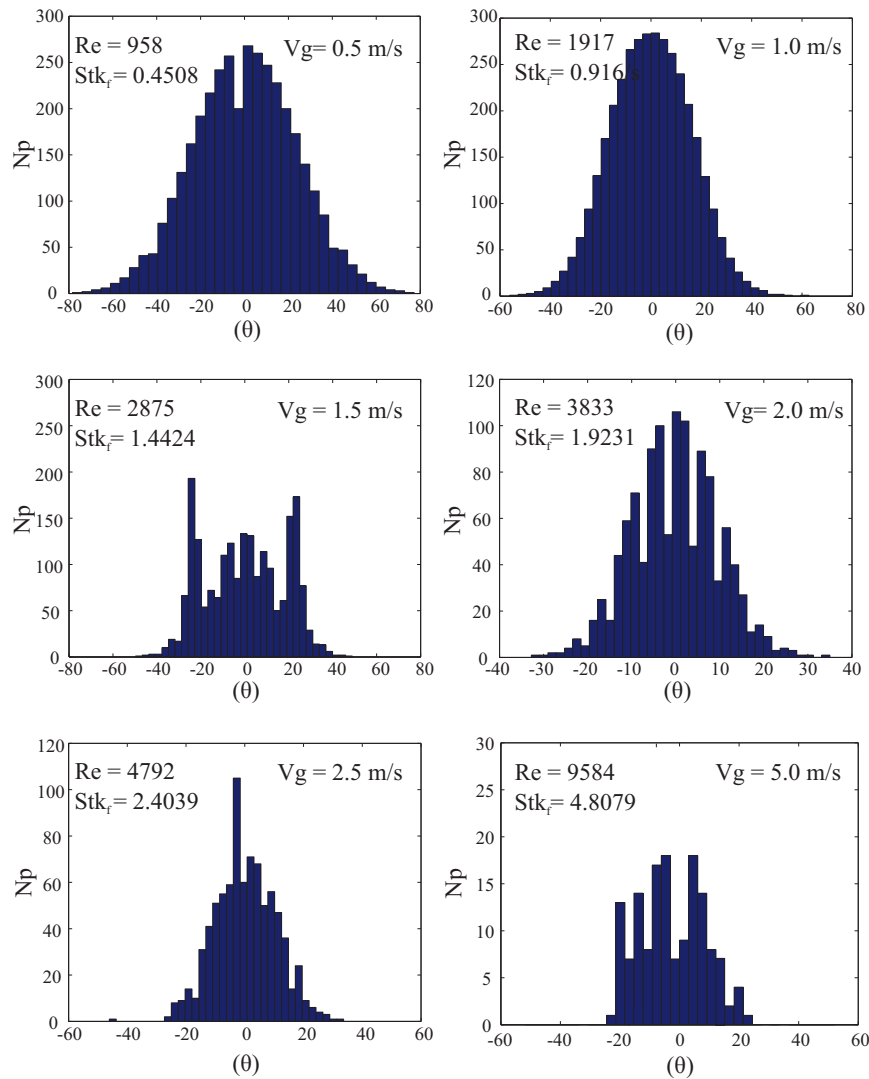


Figure 6.9: Deposition of calcium carbonate particles at different gas phase velocities [$d_p = 40 \mu\text{m}$].

5 m/s and the glass particles ceased to form any deposit at velocities beyond 2.5 m/s (see figures 5.2 (a) and (b)). It is interesting to note that a very similar behavior is seen in the numerical calculations. The particles used in the experiments had a mean diameter of $20 \mu\text{m}$ but with a distribution ranging from 5 to $70 \mu\text{m}$. Thus, in principle smaller particles must be able to stick to the surface, even at 5 m/s, but due to the presence of larger particles, the smaller particles are probably removed.

However, it is noteworthy that the selection of mean particle diameter qualitatively captures the experimental observations. To further investigate the effect of veloc-

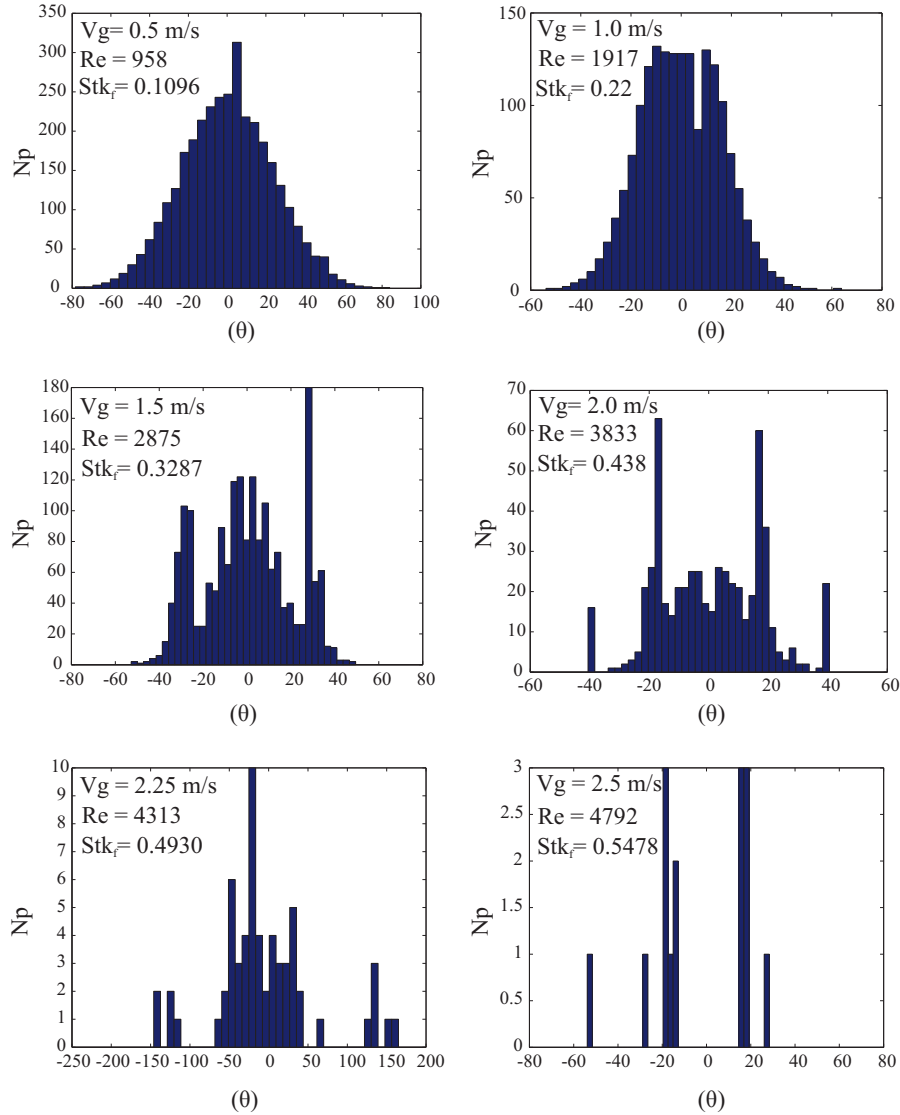


Figure 6.10: Deposition of glass particles at different gas phase velocities [$d_p = 20 \mu m$].

ity, 5000 glass particles were tracked in the domain. A range of inlet velocity and particle size was chosen which provides different Reynolds numbers based on the cylinder size and Stokes numbers for the particles. For the perfect sticking case, the deposition efficiency is directly related to the number of particles that reaches (and

deposits) on the surface. However, with the implementation of the Rogers and Reed model, only a fraction of the particles that reach the surface will eventually stick. In this case, a new deposition efficiency can be described as the ratio of the number of particles that stick to the surface to the number of particles that reach the surface. Figure 6.11 shows the relation between the Stokes number and the newly defined deposition efficiency. It can be observed that almost all of the particles that reach the surface will eventually stick when the Stokes number is less than 0.14 and for increasing Stokes number, the number of particles that stick to the surface drastically reduces. For a Stokes number of about 0.5, almost 90% of the particles that reach the wall will rebound and for increasing Stokes number ($Stk_f > 2$), almost all particles will rebound. A simple curve fit to the numerical data indicates a power law relationship with the deposition efficiency inversely proportional to the Stokes number squared. This tendency was also observed for the relationship between asymptotic layer thickness and Stokes number for the deposition of glass particles.

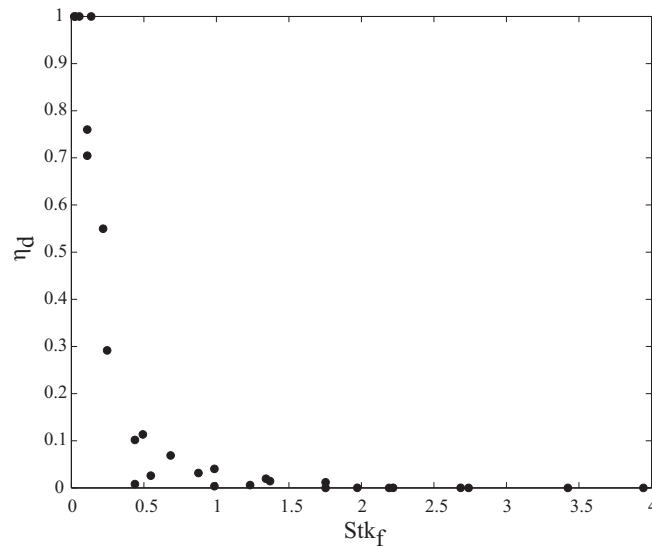


Figure 6.11: Deposition efficiency evaluated with the sticking model of Rogers and Reed as a function of Stokes number for glass particles.

6.3.2 Dry deposition over a square cylinder

In order to qualitatively evaluate the deposition model, square tubes oriented at different angles to the flow direction were studied. Figure 6.12 (a) shows the deposition of glass particles ($dp_{mean} = 20 \mu m$) in a downward flowing gas at 1.5 m/s. The numerical calculations shown correspond to the initial layer build up and 10000 parti-

cles were seeded in the flow. The raw experimental image corresponds to a snapshot taken for a much higher time to show the fouling layer. It is seen that the numerically calculated particle deposition is more on the outward sides than at the stagnation region. However, it should be noted that the numerical results are for the initial layer. The secondary collisions away from the stagnation region can result in higher particle deposition on the sides initially, but at the later stage, more particles are expected to deposit at the stagnation region. However, the interesting region is towards the edges of the cylinder. It can be observed in the experimental image that particles do not deposit towards the edges which spans approximately 5-6 mm from both sides. The numerical prediction agrees quite well with the experimental observations. The particle Stokes number based on the width of the square tube (40 mm) is about 0.38 and the critical Stokes number for a flat plate (as discussed in chapter 2) is about 0.25. Thus, particles impact the surface of the tube but if a particle rebounds, the rebound velocity is reduced and the higher velocities prevailing at the edges cause the particles to get carried away by the flow. Further, due to the implementation of the rolling moment model, particle that might stick to the surface will eventually be detached if the drag on the particles are sufficient enough for the rolling to occur.

Figure 6.12 (b) shows the deposit prediction for the square tube inclined at 15° to the flow direction and the experimental image. It is seen that the particles do not deposit on the left side and a similar observation is seen in the experiments. The maximum particle deposition occurs at the stagnation point and gradually reduces towards the right side. Figures 6.13 (a) shows the prediction of the numerical model for the square tube inclined at 30° to the flow direction. It is seen that the particle deposition ceases for a distance greater than 10 mm from the center. In the experimental image, it can be observed that the particle deposition occurs to half the width of the square tube from the left side and the right half remains almost clean. Particles impact the surface at different angles based on the flow field properties and the Stokes numbers. If the particles impact the surface at an angle (w.r.t normal vector to the surface), the sticking probability is low. For particles that might impact and stick to the surface, the flow induced shear carries away the particles. It can be observed from the vector plot of the velocity magnitudes that the velocity increases along the surface and has higher magnitude towards the right end. Figure 6.13 (b) shows the deposition for 45° inclination and the number of particles that deposit is found to be negligible. During experiments with the same configuration, it was also observed that the tube surfaces remain clean.

6.3.3 Tubes in a row

The flow characteristics and particle deposition were studied for three tubes ($D_{cyl} = 25$ mm) in a row positioned one below the other at a distance of 85 mm from each other. The gas phase velocity was 1.5 m/s and 5000 particles ($CaCO_3$, $d_p = 40$ μm) were injected into the domain. A stationary flow field was calculated and the parti-

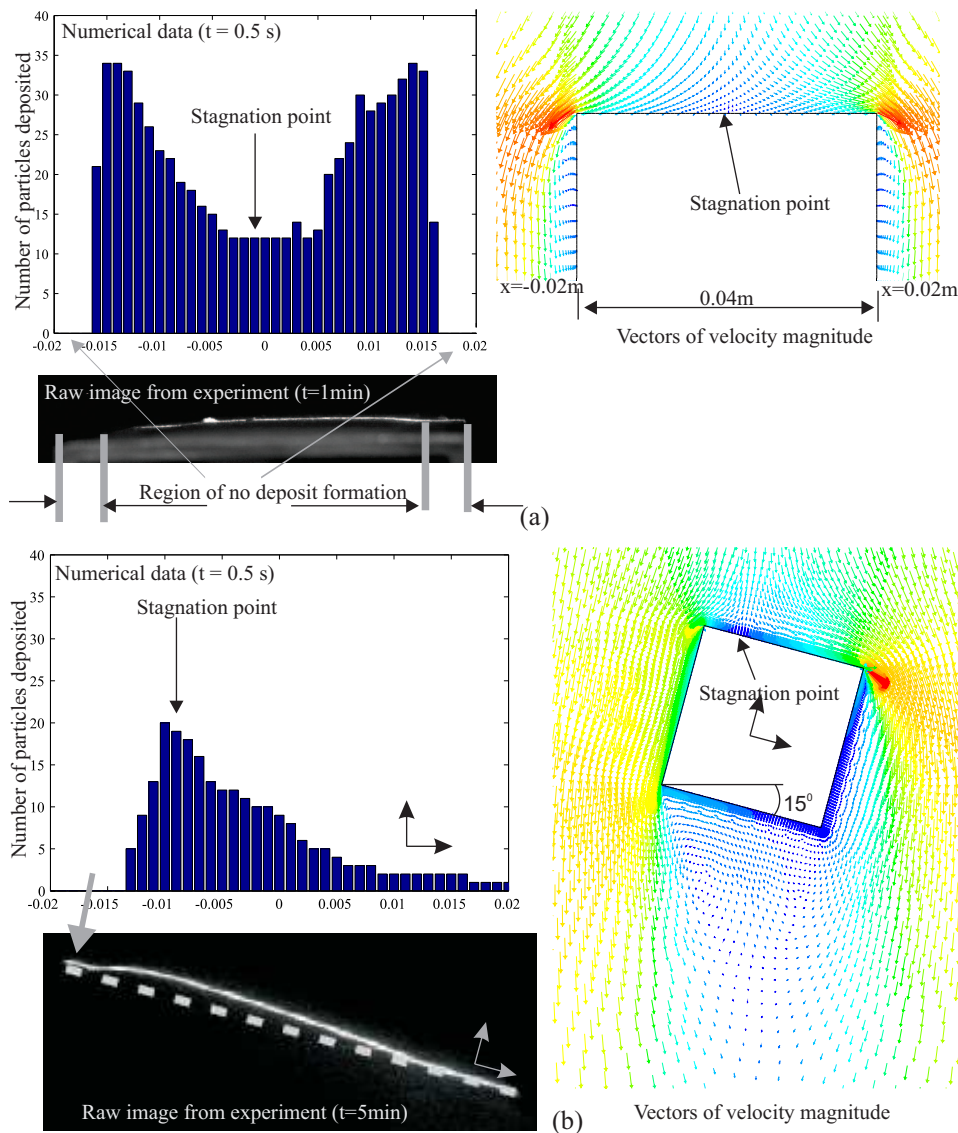


Figure 6.12: Flow field calculations and initial layer deposition prediction of the numerical model along with raw experimental images for a square tube. The velocity vectors in blue color indicate a magnitude of almost zero and the vectors in red color correspond to the highest magnitude. (a) Square tube at 0° ; (b) Square tube rotated at 15° to the flow direction. The x-axis of the histogram plot corresponds to the width of the square tube.

cles tracks are shown in figure 6.14 (d). Figure 6.14 (a) shows the deposition pattern over the first tube from the top. It is observed that the deposition is similar to the

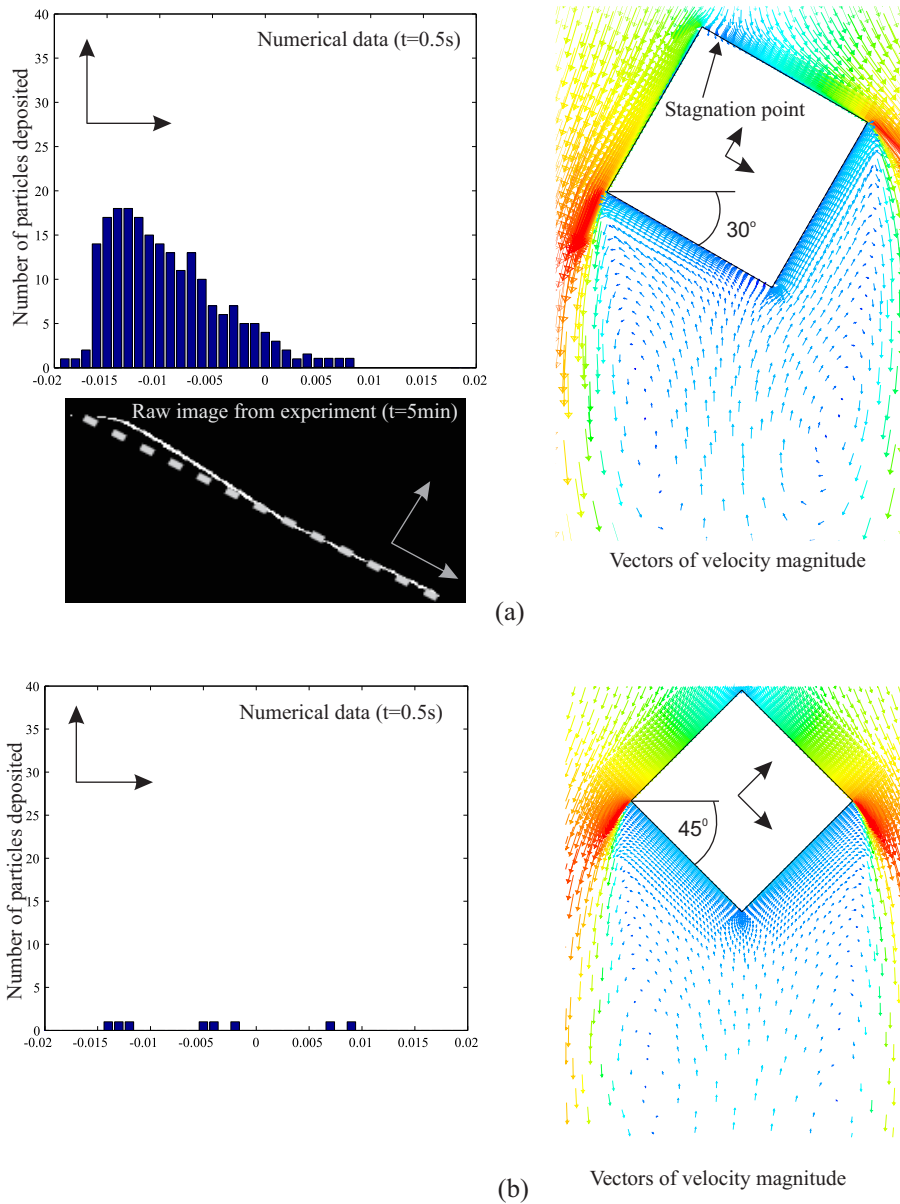


Figure 6.13: Flow field calculations and initial layer deposition prediction of the numerical model along with raw experimental images for a square tube rotated at: (a) 30° and (b) 45° to the flow direction. The velocity vectors in blue color indicate a magnitude of almost zero and the vectors in red color correspond to the highest magnitude.

single cylinder up to about 80° on each side of the stagnation point. However, a leeward side deposition is also found (which was not observed in the case of single cylinder). The presence of the downstream tube(s) drastically affects the flow field in the wake region of the preceding cylinder. Particles can get into the strained vortex behind the cylinder and arrive on the leeward side of the cylinder where it can deposit as seen in figure 6.14 (a).

Figure 6.14 (b) shows the deposition pattern for the second tube in the row. Compared to the top most tube (a), the deposition on the second tube at about $40\text{--}50^\circ$ is higher and this region corresponds to the stagnation region of the vortices of the first cylinder.

The deposition pattern for the bottom tube is shown in figure 6.14 (c). Compared to the other two cylinders on the top, the third cylinder is subjected to maximum deposition. Particles are found to deposit all around the cylinder. In the present study, the calculated flow field is stationary and transient simulations were not performed. In case of transient calculations, the vortices which are shed on each side of the upstream cylinders would create a complex flow field and calls for detailed study. As the primary focus of the present study is to evaluate the applicability of the model, detailed analysis regarding flow field and particle deposition in terms of cylinder pitch and arrangements have not been performed.

6.3.4 Evolution of fouling layer

The numerical model can be extended to capture the fouling layer growth dynamics by relating the rate of particle deposition to the changes in the geometry. Figure 6.15 shows the modified flowchart to capture the layer growth. By obtaining the initial deposition of the particles over the surface, if the amount of deposition reaches a stage where a significant change in the deposit geometry occurs, then the geometry of the tube can be changed by assuming the previously deposited particles to be a new layer. By using an effective mass for the powdery layer as suggested by Van Beek [62], the deposition over the new layer can be found. However, due to the change in the geometry, a flow field corresponding to the new geometry has to be solved. A test case was setup to capture the growth dynamics of glass particles over a stainless steel tube. The free stream gas velocity was 1.5 m/s and 20000 glass particles were seeded in the flow. The Reynolds number was 2020 and the Stokes number for the particles was 0.26.

It was observed in the experiments and in the previous numerical cases that, the particles do not deposit on the leeward side of the cylinder for the single cylinder case. Although it is necessary to solve a transient flow field, as a demonstration case, steady state flow calculations were used to evaluate the fouling layer growth discussed in this section. As shown in the flowchart, the simulations are started with a clean tube and after obtaining the flow field, particles were injected at the inlet which is 0.5 m upstream over the entire inlet. The number of particles and the location for

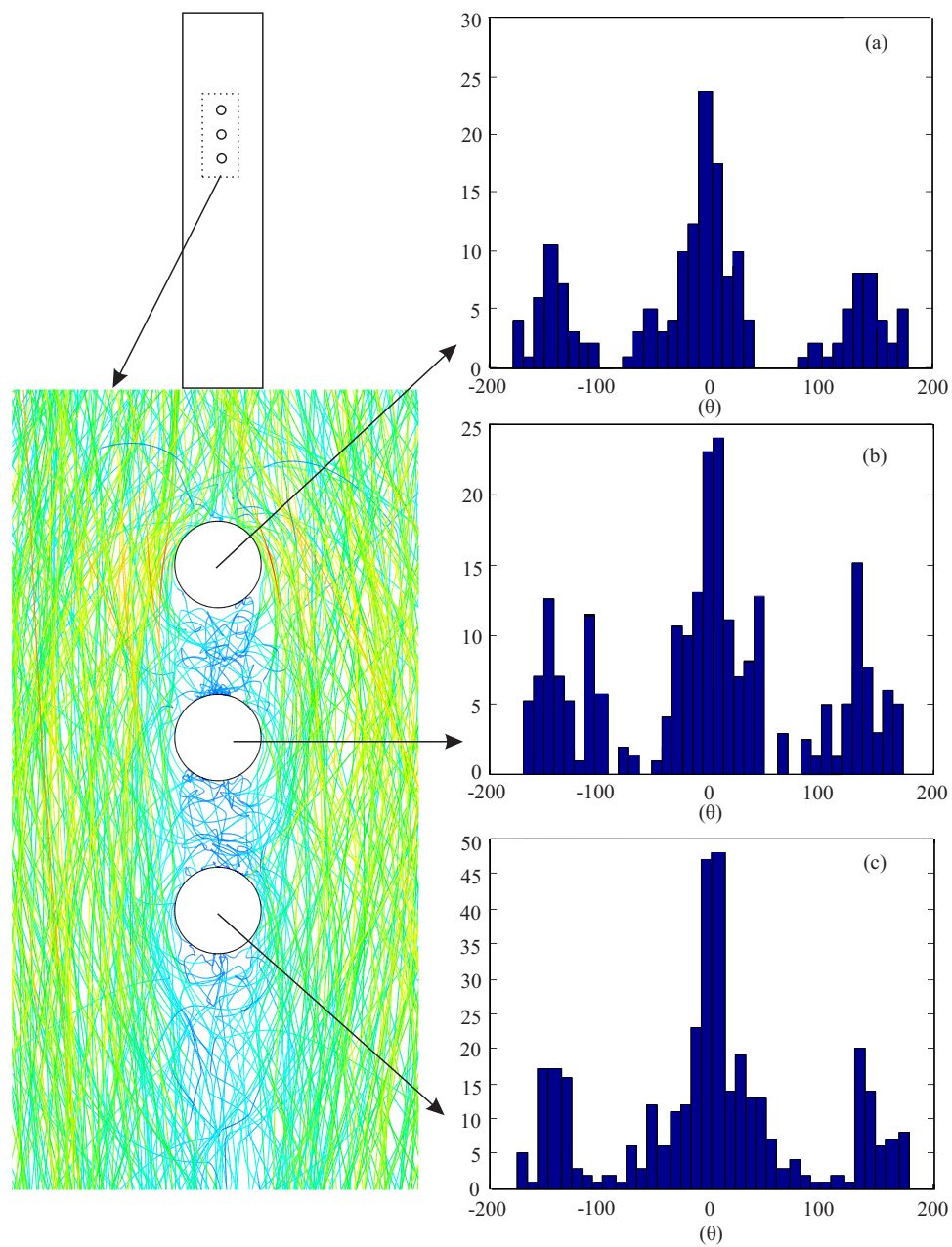


Figure 6.14: Particle deposition pattern over three circular cylinders arranged in line with the flow.

the particles deposited on the cylinder are recorded. Based on the number of particles located at each 5° interval on the cylinder, a new mesh is generated manually and the flow field is solved for the new geometry. The process of particle injection and meshing is carried out successively until the particle deposition becomes negligible. The results are shown in figure 6.16. It is seen that with changing geometry, the number of particles that deposit over the cylinder gradually reduces and the layer reaches a geometric configuration where the number of particles that deposit becomes negligible. However, during experiments (using a high speed camera), it was observed that a continuous deposition and erosion of particles occurs on the cylinder.

6.3.5 Particle deposition on a liquid layer

In chapter 2 and 3, the impaction of a particle over a liquid coated surface was studied in considerable detail. In order to have a simple and viable numerical model for the wet impaction process, the energy dissipated in the viscous layer of the liquid as a function of Stokes number was evaluated by fitting curves for the elastic and elastic-plastic case. The curve fit for the elastic case with a confidence level of 95% yields a relation with a RMSE value of 0.021 as:

$$Q_{liq} = ae^{b.Stk} + ce^{d.Stk} \quad (6.30)$$

where the constants are $a = 0.3155$, $b = -1.008$, $c = 0.3155$ and $d = 0.1153$. Similarly, a curve fit for the elastic-plastic case yields a relation with an RMSE value of 0.033 as:

$$Q_{liq} = AStk^B + C \quad (6.31)$$

with the constants $A = 1.021$, $B = -0.9687$ and $C = 0.4768$. The equations are valid for Stokes numbers up to 150. Figure 6.17 and 6.18 show the curve fits to the experimental data. If the energy lost in the rebound phase due to viscous drag on the particle is considered negligible, the rebound behavior of the particle can be evaluated with the empirical formulations. If the particle and substrate properties are known before hand, one can estimate whether the collision would result in an elastic or elastic plastic impact. Based on this, the energy dissipated in the viscous layer can be evaluated (provided the liquid layer thickness is less than 50% of the particle radius). Based on the remaining energy associated with the particle, the rebound velocity can be evaluated based on dry impaction model discussed earlier.

The models for wet impaction were implemented along with the dry deposition model and the results of particle deposition for varying particle size and liquid film viscosities are listed in table 6.2. The numbers in the first row of the table indicate the diameter of the particles and the values in the columns under each particle diameter indicate the number of particles that eventually stick to the surface under different conditions. The table shows a comparison between perfect sticking, dry deposition

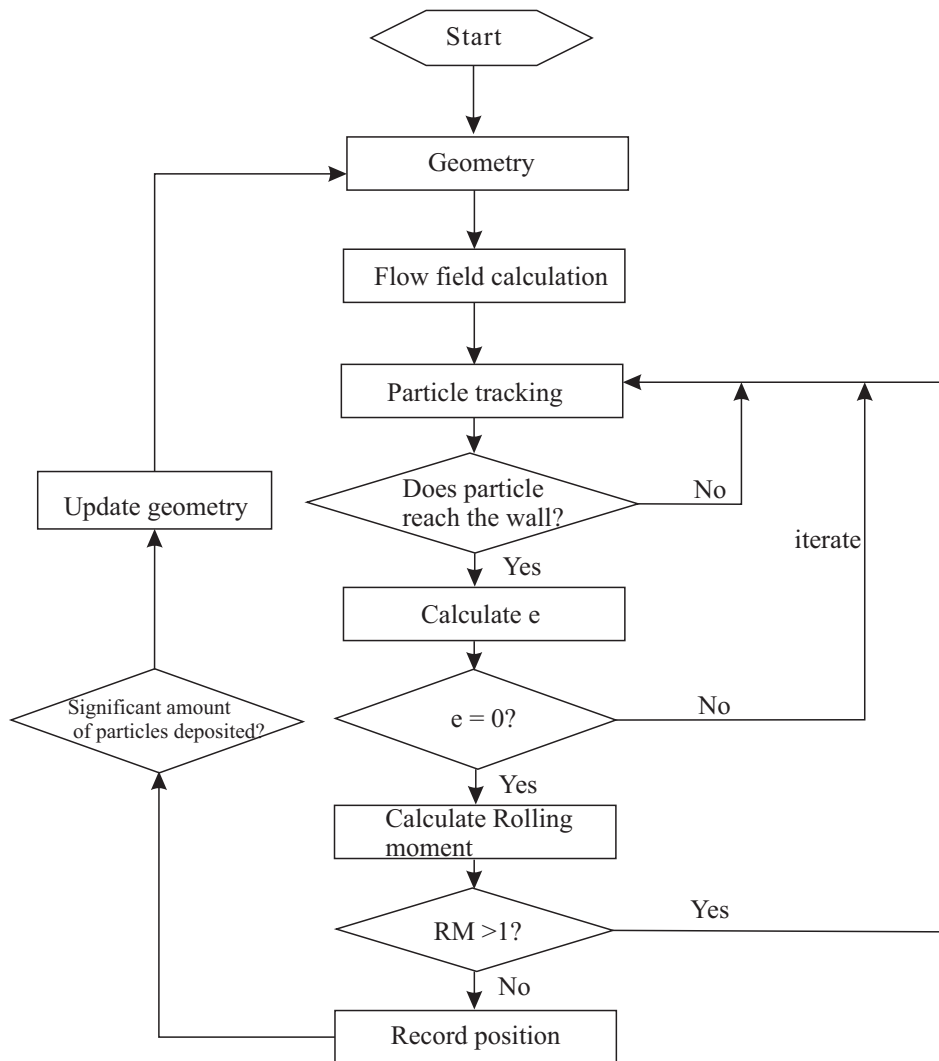


Figure 6.15: Flow chart indicating the modeling approach to capture fouling layer growth.

and wet deposition assuming a thin liquid layer on a tube for different liquid viscosities.

As discussed earlier, a drastic difference between perfect sticking and Roger and Reed model can be observed for the dry deposition case. The Roger and Reed model predicts that deposition of glass particles under dry condition ceases for particles greater than $60 \mu\text{m}$ but the presence of the liquid film enhances deposition of particles. This is however dependent on the Stokes number when the particle impacts

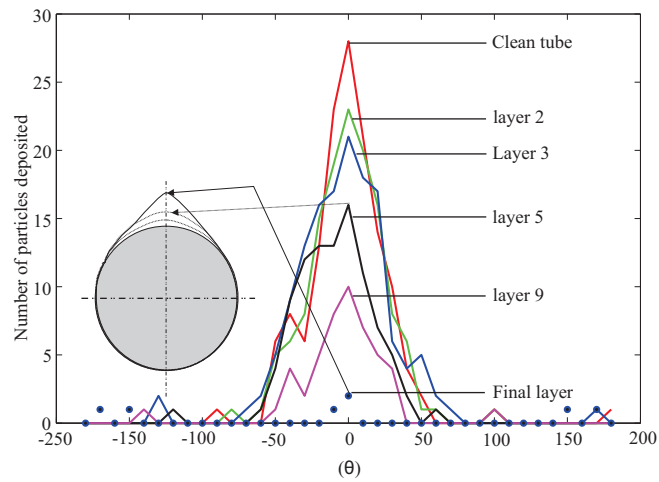


Figure 6.16: Numerical results capturing the evolution of fouling layer.

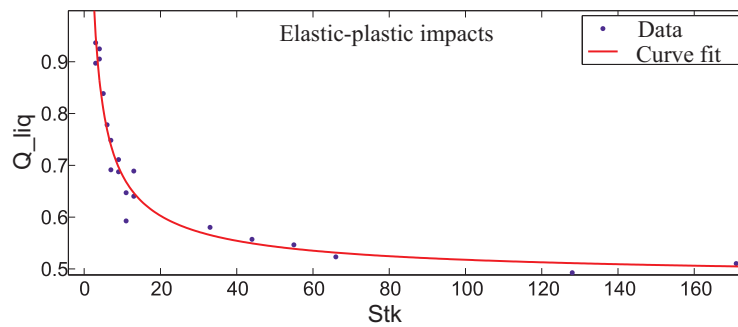


Figure 6.17: Experimental data and curve fit for the energy dissipated by a particle in the liquid layer for an elastic-plastic impact over a liquid coated substrate.

the surface. For a low viscosity liquid, the deposition ceases for a particle size of about $140 \mu\text{m}$ and for increasing viscosity, the deposition correspondingly increases. However the number of particles that deposit is far less than the number for the perfect sticking case. Hence the implementation of the model leads to more realistic predictions for particle deposition.

6.4 Conclusions

The deposition model for dry particles was implemented along with a model to describe wet impaction of a particle over liquid coated tube. The preliminary results for

Table 6.2: Comparison of the influence of different liquid films on the deposition of glass particles. The free stream velocity was 1.5 m/s and $Re = 1922$. 20,000 particles were injected into the flow and the integer numbers listed in the table correspond to the number of particles that deposit over the cylinder.

d_p (μm)	20	30	40	60	80	100	140	250
Np deposited								
Stk_f	0.2371	0.5334	0.9482	2.133	3.7928	5.9263	11.6155	37.03
Dry	46	37	23	2	0	0	0	0
Perfect sticking	97	538	597	940	1113	1360	1462	2140
Wet ($\mu=0.1Pa.s$)	-	-	597	940	1113	1360	1462	143
Stk	-	-	0.003-0.065	0.008-0.155	0.006-0.265	0.025-0.392	0.034-0.664	0.176-3.096
Wet ($\mu=0.01Pa.s$)	-	-	597	940	1113	464	208	17
Stk	-	-	0.05-0.65	0.08-1.6	0.25-2.75	0.4-3.8	0.6-6.5	2-11
Wet ($\mu=0.001Pa.s$)	97	293	188	151	49	3	0	
Stk	0.06-0.374	0.08-2.675	0.22-6.142	1.18-14.96	1.38-25.8	4.3-38.2	4.9-66.5	-

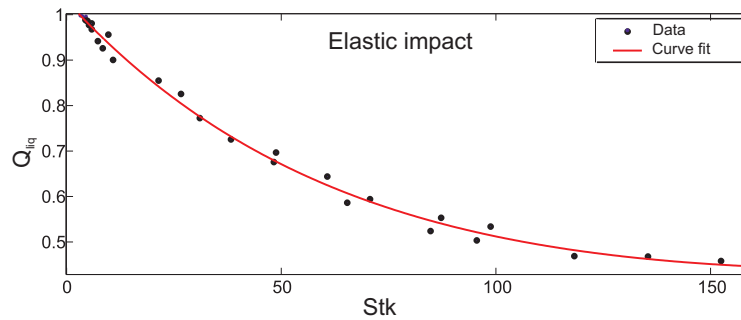


Figure 6.18: Experimental data and curve fit for the energy dissipated by a particle in the liquid layer for an elastic impact over a liquid coated substrate.

collection efficiency using the RSM model showed lower deposition rates at lower Stokes number as compared to the modified $k-\epsilon$ model. However, it has been reported that the $k-\epsilon$ model tends to over-predict particle deposition. The implementation of a sticking model based on a particle undergoing elastic-plastic deformation yields lower deposition rates than for the perfect sticking case.

The model for particle removal due to shear flow of the fluid over the particle through the rolling moment model was coupled to the deposition model and simulations were run for various cases to qualitatively compare the results with the experimental observations. The numerical model well predicted negligible particle deposition of glass particles at 2.5 m/s as also observed in the experiments. The model is also able to predict the deposition behavior on an inclined plane. Further, for particles impacting a liquid coated surface, an empirical model was incorporated into the numerical simulations. Based on the energy dissipated in the viscous layer, the model predicts deposition of particles more reasonably than the perfect sticking case. As a test case, the evolution of fouling layer was captured under dry deposition condition. It was observed that the model predicts the layer growth reasonable well with the layer shaped and profile consistent with the experimental observations. The numerical approach serves as a good tool to evaluate the deposition behavior in tube bundles and to optimize the design of heat exchanger systems.

Conclusions and recommendations for future work

Conclusions

The present work was directed towards gaining information in three main areas: a) particle deposition in the presence of a liquid medium between two interacting bodies, b) influence of process conditions on fouling and c) preliminary numerical modeling. The main conclusions that can be drawn are:

- Particle deposition is enhanced in the presence of a liquid film. However, all particles that reach a liquid coated surface do not stick to the surface. To understand sticking and rebound on a liquid coated surface, a detailed literature review was conducted and two approaches to the modeling were encountered. The modeling approaches were evaluated numerically and experimentally. It was observed that the models were limited in their applicability and the problem at hand was basically the quantification of the energy dissipated in the liquid film. In the present work, this was achieved by drop experiments where the particle-surface undergoes elastic and elastic-plastic deformation. Wet impaction with elastic-plastic deformation was hitherto not reported. The energy lost in the viscous layer is quantified for varying Stokes number. The experimental results indicated that a particle will stick to a surface if its Stokes number is less than a critical value, which in the present case, was found to be in the range of 2 to 5. For higher Stokes numbers, by assuming the viscous losses

during the rebound phase of the particles to be negligible, the particle rebound can be evaluated based on the dry impaction model.

- In order to understand the influence of global parameters on fouling layer growth, an experimental facility was conceptualized and built. The experimental setup can be used to perform experiments under a wide range of parameters and under controlled conditions. Experiments indicated a strong influence of gas velocity and tube geometry on particle deposition. The asymptotic layer thickness formed in dry deposition experiments was found to be inversely proportional to the particle Stokes number in the mean flow. By varying the geometry and the inclination angle of the tube axis to the flow direction, a sharp reduction in fouling tendency was observed. The reduction in fouling was due to the lower critical sticking velocity below which a particle sticks to the surface. Experiments with liquid coated tubes indicated enhanced particle deposition, but the effect of the presence of an initial liquid layer is limited.
- A commercial CFD package was used to solve the flow field and track the particles in the domain. However, when a particle reaches a surface of interest, user defined functions need to be defined which incorporates the deposition and shear removal model for dry deposition. A numerical analysis with the implemented dry deposition model captures the overall dynamics of dry particle deposition. The influence of gas velocity was evaluated along with the varying geometric conditions. The experimental data of wet impaction was used to obtain a curve fit equation for the energy losses in the liquid film and was implemented in conjunction with the dry deposition model to predict particle deposition on a liquid coated surface. The model predicts the deposition pattern in consistence with experimental observations. Further, the numerical model can be used to evaluate the evolution of fouling layer growth over time which can be an important tool to design optimal systems.

Recommendations for future work

- In the present work on impaction experiments over liquid films, the exact height of the liquid layer over which most of the particle kinetic energy is dissipated could not be quantified. Given that, in most of the practical applications, the information on the liquid layer thickness present on a surface is difficult to obtain, the results presented here provides a means to evaluate the sticking criteria based on Stokes number. However, for systems where such information is available, evaluating the sticking criteria based on the liquid layer thickness will be important. Future experiments with varying gap Reynolds numbers for constant Stokes numbers and vice versa can be beneficial to quantify energy losses under different conditions.

- Oblique impact of a particle over liquid coated substrates was not studied in the present work. Experiments involving elastic and elastic-plastic impacts at other angles apart from normal incidence will provide more realistic information which can improve the numerical model. The energy dissipated in the liquid bridge formation and rupture was considered negligible in the present study. However, for high viscosity liquids, it will be necessary to quantify this effect. The present work was limited to study the impaction of a dry particle over a liquid coated surface. Future work involving impaction of liquid coated particles over dry surfaces and over liquid coated substrates should be considered. Based on a literature study, it can be mentioned that the studies involving particle impacts at elevated temperatures are very meager. However, studies based on high temperature impacts are vital to understand the dependence of particle adhesion at elevated temperatures.
- An initial effort was made to implement condensation effects in the controlled fouling facility. By implementing a vapor phase in the gas flow and allowing it to condense on the deposition tube along with the particles would provide more information on the overall deposition dynamics. Future work on controlled experiments with this aspect taken into consideration would be beneficial. Further, detailed deposition measurements in the controlled fouling rig which can provide validation data for the numerical model would be highly valuable. Finally, the experimental facility has been made modular which facilitates studies on the influence of various tube geometries and arrangements on fouling under various process conditions.
- The present numerical model was evaluated qualitatively on its performance abilities. Further development of the model would require more detailed validation of the model. The history of a particle sticking to the surface at a given location and its removal in the following time step(s) has not been implemented in the present work and needs attention to describe the removal process in a complete way. It would prove beneficial to divert the attention towards numerical modeling using DEM simulations coupled to the fluid flow to achieve a comprehensive model.

Bibliography

- [1] Abd-Elhady, M. S. (2005). *Gas-side particulate fouling in biomass gasifiers*. PhD thesis, Eindhoven University of Technology, The Netherlands.
- [2] Abd-Elhady, M. S., Abd-Elhady, S., Rindt, C. C. M., and van Steenhoven, A. A. (2009a). Removal of gas-side particulate fouling layers by foreign particles as a function of flow direction. *Applied Thermal Engineering*, 29:2335–2343.
- [3] Abd-Elhady, M. S., Rindt, C. C. M., and van Steenhoven, A. A. (2009b). Optimization of flow direction to minimize particulate fouling of heat exchangers. *Heat Transfer Engineering*, 30(10-11):895–902.
- [4] Abd-Elhady, M. S., Rindt, C. C. M., and van Steenhoven, A. A. (2011). Influence of the apex angle of cone shaped tubes on particulate fouling on heat exchangers. *Heat Transfer Engineering*, 32(3-4):272–281.
- [5] Abd-Elhady, M. S., Rindt, C. C. M., Wijers, J. G., van Steenhoven, A. A., Bramer, E. A., and van der Meer, T. H. (2004). Minimum gas speed in heat exchangers to avoid particulate fouling. *Intl. J. Heat and Mass transfer*, 47:3943–3955.
- [6] ANSYS (2009). *Fluent 12.0 Users guide and theory guide*. ANSYS.
- [7] Antonyuk, S., Heinrich, S., Deen, N., and Kuipers, H. (2009). Influence of liquid layers on energy absorption during particle impact. *Particuology*, 7:245–259.
- [8] Bailer, F. (1998). *Etude des differents mecanismes de depot conduisant a l'encrassement particulaire en phase gazeuse des tubes d'exchangeurs de chaleur*. PhD thesis, l'Institut National Polytechnique de Grenoble.
- [9] Barnocky, G. and Davis, R. H. (1987). Elastohydrodynamic collision and rebound of spheres: Experimental verification. *Physics of Fluids*, 31(06):1324–1329.
- [10] Baxter, L. L. (1993). A mechanistic description of ash deposition during pulverized coal combustion: prediction compared with observations. *Fuel*, 72(10):1411–1418.

- [11] Beek, M. C., Rindt, C. C. M., Wijers, J. G., and van Steenhoven, A. A. (2001). Analysis of fouling in refuse waste incinerators. *Heat Transfer Engineering*, 22:22–31.
- [12] Bejan, A. (1993). *Heat Transfer*. John Wiley & sons.
- [13] Bohnet (1995). Influence of the gas temperature on the separation efficiency of aerocyclones. *Chemical Engineering and Processing*, 34:151–156.
- [14] Bott, T. R. (1995). *Fouling of heat exchangers*. Elsevier.
- [15] Briscoe, B. J. and Adams, M. J., editors (1987). *Tribology in particulate technology*. Adam Hilger.
- [16] Bryers, R. W. (1996). Fireside slagging, fouling and high temperature corrosion of heat transfer surface due to impurities in steam rising fuels. *Prog. Energy Combustion Sci*, 22:29–120.
- [17] Burdick, G. M., Berman, N. S., and Beaudoin, S. P. (2001). Describing hydrodynamic particle removal from surfaces using the particle reynolds number. *Journal of Nanoparticle research*, 3:455–467.
- [18] Clark, H. M. (1991). On the impact rate and impact energy of particles in a slurry pot erosion tester. *Wear*, 147(01):165–183.
- [19] Clark, H. M. (1995). A comparison of the particle impact in gas-solid and liquid-solid erosion. *Wear*, 186:465–472.
- [20] Clark, H. M. and Burmeister, L. C. (1992). The influence of the squeeze film on the particle impact velocities in erosion. *Int J Impact Energy*, 12(3):415–426.
- [21] Davis, R. H., Rager, D. A., and Good, B. T. (1987). Elastohydrodynamic collision and rebound of spheres: Experimental verification. *Phy. Fluids*, 31(06):1324–1329.
- [22] Davis, R. H., Rager, D. A., and Good, B. T. (2002). Elastohydrodynamic rebound of spheres from coated surfaces. *Journal of Fluid Mechanics*, 468:107–119.
- [23] Davis, R. H., Serayssol, J. M., and Hinch, E. J. (1986). The elastohydrodynamic collision of two spheres. *Journal of Fluid Mechanics*, 163:479–497.
- [24] Dhebi, A. (2008). Assessment of a new fluent model for particle dispersion in turbulent flows. *Nuclear Engineering and Design*, 238(3):707–715.
- [25] Drift, A. v. d. (2004). Product gas cooling and ash removal in biomass gasifier. Technical Report ECN-C-04-077, ECN.
- [26] Eirich, F. R. and Tabor, D. (1947). Collisions through liquid films. *Proc. Cambridge Philosophical Society*, 4(04):566–580.

-
- [27] Evans, R. J. and Milne, T. A. (2001). Biomass gasifier "tars": Their nature, formation, and conversion. Technical report, National Renewable Energy Laboratory, U.S.A.
- [28] Friedlander, K. S. (2000). *Smoke, Dust, and Haze. Fundamentals of Aerosol Dynamics*. Oxford University Press, 2nd edition.
- [29] Gee, M. L., McGuiggan, P. M., Israelachvili, J. N., and Homola, A. M. (1990). Liquid to solidlike transitions of molecularly thin films under shear. *The Journal of Chemical Physics*, 93(3):1895–1906.
- [30] Halow, J. S. (1973). Incipient rolling, sliding and suspension of particles in horizontal and inclined turbulent flow. *Chemical Engineering Science*, 28(1):1–12.
- [31] Hansen, L. (1998). *Melting and sintering of ashes*. PhD thesis, Technical University of Denmark.
- [32] Ingham, D. B., Hildyard, L. T., and Hildyard, M. L. (1990). On the critical stokes number for particle transport in potential and viscous flows near bluff bodies. *J. Aerosol Science*, 21(7):935–946.
- [33] Isaak, P., Tran, H., Barham, D., and Reeve, D. (1986). Stickyness of fireside deposits in kraft recovery units. *Journal of Pulp and Paper Science*, 12(3):J84–J92.
- [34] Jia, X., Caulkin, R., Williams, R. A., and Zhou, Z. (2010). The role of geometric constraints in random packing of non-spherical particles. *EuroPhysics Letters (EPL)*, 92(68005).
- [35] Kær, S. K. (2001). *Numerical investigation of deposit formation in straw-fired boilers, using CFD as the framework for slagging and fouling predictions*. PhD thesis, Aalborg University.
- [36] Kaiser, S., Antonijevic, D., and Tsotsas, E. (2001). Formation of fouling layers on a heat exchanger element exposed to warm, humid and solid loaded air streams. *Experimental Thermal and Fluid Science*, 26:291–297.
- [37] Kalisz, S. and Pronobis, M. (2005). Investigations on fouling rate in convective bundles of coal-fired boilers in relation to optimization of sootblower operation. *Fuel*, 84:927–937.
- [38] Kern, D. and Seaton, R. E. (1959). A theoretical analysis of thermal surface fouling. *Chem. Eng. Prog.*, 4:258–262.
- [39] Lian, G., Adams, M. J., and Thornton, C. (1996). Elastohydrodynamic collisions of solid spheres. *J. Fluid Mech.*, 311:141–152.

- [40] McLaughlin, M. (1968). *Experimental study of particle wall collisions relating to flow of solid particles in a fluid*. PhD thesis, California Institute of Technology.
- [41] Moza, A. K. and Austin, L. G. (1981). Studies on slag deposit formation in pulverized coal combustors.1.results on the wetting and adherence of synthetic coal ash drops on steel. *Fuel*, 60:1057–1064.
- [42] Obernberger, I. and Brunner, T. (2005). Fly ash and seosol formation in biomass combustion processes-an introduction. In *Aerosols in biomass combustion*, pages 1–12.
- [43] Robinson, A. L., Junker, H., and Baxter, L. L. (2002). Pilot-scale investigation of the influence of coal-biomass co-firing on ash deposition. *Energy and Fuels*, 16:343–355.
- [44] Rogers, D. E. and Reed, J. (1984). The adhesion of particles undergoing an elastic-plastic impact with a surface. *Journal of Physics D: Applied Physics*, 17:677–689.
- [45] Rosner, D. E. and Nagarajan, R. (1992). *Inorganic transformations and ash deposition during combustion*, chapter Deposition dynamics of combustion-generated particles: Summary of recent studies of particle transport mechanisms, capture rates and resulting deposit microstructure/properties, pages 585–693. Engineering Foundation/ASME,New York.
- [46] Ruge, J. (1991). *Belagbildung auf quer angestromten warmeustruscherrrohrbun-deln*. PhD thesis, Technische Universität Braunschweig.
- [47] Senior, C. L. and Srinivasachar, S. (1995). Viscosity of ash particles in combustion systems for prediction of particle sticking. *Energy and Fuels*, 9:277–283.
- [48] Sippula, O. (2010). *Fine particle formation and emissions in biomass combustion*. PhD thesis, University of Eastern Finland.
- [49] Somerscales, E. F. C. (1990). Fouling of heat transfer surfaces: An historical review. *Heat Transfer Engineering*, 11(1):19–36.
- [50] Son, J. S. and Hanratty, T. J. (1969). Velocity gradient at the wall for flow around a cylinder at reynolds number from 5×10^3 to 5×10^5 . *Journal of Fluid Mechanics*, 35(2):353–368.
- [51] Steinhagen, H. M. M. and Middis, J. (1989). Particulate fouling in plate heat exchangers. *Heat Transfer Engineering*, 10(4):30–36.
- [52] Stevan, D. J. (2001). Hot gas conditioning: Recent progress with larger-scale biomass gasification systems. Technical report, National Renewable Energy Laboratory, U.S.A.

-
- [53] Stevens, D. J. (2001). Hot gas conditioning: Recent progress with large scale biomass gasification systems. Technical Report NREL/SR-510-29952, National Renewable Energy Laboratory, Colorado.
- [54] Theis, M., Skrifvars, B.-J., Hupa, M., and Tran, H. (2006a). Fouling tendency of ash resulting from burning mixtures of biofuels. part 1: Deposition rates. *Fuel*, 85:1125–1130.
- [55] Theis, M., Skrifvars, B.-J., Zevenhoven, M., Hupa, M., and Tran, H. (2006b). Fouling tendency of ash resulting from burning mixtures of biofuels. part 2: Deposit chemistry. *Fuel*, 85:1992–2001.
- [56] Theis, M., Skrifvars, B.-J., Zevenhoven, M., Hupa, M., and Tran, H. (2006c). Fouling tendency of ash resulting from burning mixtures of biofuels. part 3: Influence of probe surface temperature. *Fuel*, 85:2002–2011.
- [57] Thirupataiah, Y. and Sundararajan, G. (1990). The volume of crater formed by the impact of a ball against flat target materials - The effect of ball hardness and density. *Int. J. Impact Engineering*, 9(02):237 – 246.
- [58] Thonon, B., Grandgeorge, S., and Jallut, C. (1999). Effect of geometry and flow conditions on particulate fouling in plate heat exchangers. *Heat Transfer Engineering*, 20(3):12–24.
- [59] Tian, L. and Ahmadi, G. (2007). Particle deposition in turbulent duct flows - comparison of different model predictions. *Aerosol Science*, 38:377–397.
- [60] Tran, H., Mao, X., Kuhn, D., Backman, R., and Hupa, M. (2002). The sticky temperature for recovery boiler fireside deposits. *Pulp and Paper Canada*, 103(9):29–33.
- [61] Urbain, G., Cambier, G., Deletter, M., and Anseau, M. R. (1981). Viscosity of silicate melts. *Transactions and journal of the British ceramic society*, 80:139–141.
- [62] Van Beek, M. C. (2001). *Gas-side fouling in heat recovery boilers*. PhD thesis, Eindhoven University of Technology, The Netherlands.
- [63] Vargas, S., Frandsen, F. J., and Dam-Johansen, K. (2001). Rheological properties of high-temperature melts of coal ashes and other silicates. *Progress in Energy and Combustion Science*, 27:237–429.
- [64] Walsh, P. M., Sayre, A. N., Loehden, D., Monroe, L. S., Beer, J. M., and Sarofim, A. F. (1990). Deposition of bituminous coal ash on an isolated heat exchanger tube: effects of coal properties on deposit growth. *Progress in Energy and Combustion Science*, 16:327–346.

- [65] Wang, H. and Harb, N. (1996). Modeling of ash deposition in large scale combustion facilities. *Progress in Energy and Combustion Science*, 23:267–282.
- [66] Werner, B. T. (1987). *A physical model of wind-blown sand transport*. PhD thesis, California Institute of Technology.
- [67] White, F. M. (2002). *Fluid Mechanics*. McGraw Hill, 5th edition.
- [68] Wibberley, L. J. (1982). Alkali-ash reactions and deposit formation in pulverized-coal-fired boiler: experimental aspects of sodium silicate formation and the formation of deposits. *FUEL*, 61:93–99.
- [69] Yeong, M., Lee, D. R., Ahn, S. P., and Park, H. D. (1998). An experimental study on fouling over a single tube. *KSME International Journal*, 12(6):1162–1173.
- [70] Yiantsios, S. G. and Karabelas, A. J. (1995a). Detachment of spherical microparticles adhering on flat surfaces by hydrodynamic forces. *Journal of Colloid and Interface Science*, 176:74–85.
- [71] Yiantsios, S. G. and Karabelas, A. J. (1995b). Detachment of spherical microparticles adhering on flat surfaces by hydrodynamic forces. *Journal of colloid and interface science*, 176:74–85.
- [72] Zhang, F., Busnaina, A. A., Fury, M. A., and Wang, S. Q. (2000). The removal of deformed submicron particles from silicon wafers by spin rinse and megasonics. *J. Electron mater*, 29:199–204.
- [73] Zoetewij, M. L., Donck, v. d. J. C. J., and Versluis, R. (2009). Particle removal in linear shear flow: Model prediction and experimental validation. *Journal of Adhesion Science and Technology*, 23:899–911.
- [74] Zou, R. P. and Yu, A. B. (1996). Evaluation of the packing characteristics of mono-sized non-spherical particles. *Powder Technology*, 88:71–79.

Gasification and gas phase contaminants in biomass gasifiers

A.1 Biomass gasification

The culmination of the effects of ever decreasing fossil fuel reserves, limitations posed to the use to natural renewable energy resources, and the ever increasing drastic effects of nuclear and fossil fuels on the environment have made biomass an attractive alternative energy resource. Biomass can be burnt directly or can be converted to liquid or gaseous form. The latter option is better, because liquids and gases react and burn more efficiently than in solid form. Energy from biomass is derived using a thermochemical process in which biomass is heated with limited oxygen to gasify it to synthesis gas (mainly a mixture of nitrogen, carbon monoxide and hydrogen) or liquefy it to pyrolysis oil. Gasification is defined as a process by which either a solid or liquid carbonaceous material, containing mostly chemically bound carbon, hydrogen, oxygen, and a variety of inorganic and organic constituents, reacts with air, oxygen, and/or steam. During these reactions, sufficient exothermic energy is produced which sustains the generation of primary gaseous products containing mostly CO , H_2 , CO_2 , H_2O , and light hydrocarbons combined with volatile and condensable organic and inorganic compounds. Most of the inorganic constituents in the feedstock are chemically altered and either discharged as bottom ash or entrained with the raw product gas as fly-ash. Unless the raw gas is combusted immediately, it is cooled, filtered, and scrubbed with water or a process-

derived liquid to reduce condensible species and any carry-over particles [52]. The details on this subject matter can be found in many articles and is not covered here.

A.2 Gas phase contaminants

It is reported that the products of gasification will vary according to the feedstock used, reactor configuration and oxidant used. Owing to several reasons like incomplete gasification, incomplete oxidation and reactor geometry, the product gas is usually contaminated with particulates, alkali compounds, tars etc [53]. The detailed ash formation mechanisms and pathways have been studied by various researchers [42] [48] and the following description is mainly derived from Stevan [52].

- **Particulates:** Particulates are generally defined as solid-phase materials entrained in the raw product gas stream. Particulates typically include the inorganic "ash" derived from mineral matter in the biomass feedstock, unconverted biomass in the form of char, or material from the gasifier bed. A primary source of fly ash particles is the mineral matter in the biomass feedstock. As the feedstock is gasified, the inorganic matter from the feedstock may be either retained in the gasifier bed or entrained in the product gas and swept from the reactor. The concentrations of ash in the product gas are therefore dependent both on reactor design and on the mineral content of the biomass feedstock. In gasification systems with moving beds, inorganic particulates may include fine material from the attrition of the bed material such as sand. Another source of particulates is the char formed when the biomass feedstock is incompletely gasified. Aerosols are also generated in biomass combustion process which are of smaller size than the fly ash particles. A typical particle size distribution (PSD) curve for grate fired combustion system is shown in figure A.1. The data is adopted from Obernberger and Brunner [42] and shows a typical bimodal size distribution. The particle size distribution of fly ashes at boiler outlets are typically in the range of sub micrometer to about few hundred micrometers with a distribution peak at about 30 to 70 μm .
- **Alkali compounds:** The chemical composition of the ash determines the physical properties of the material such as softening, melting point, or vaporization point. Biomass feedstock may contain significant amounts of alkali salts, particularly potassium and sodium. Potassium is an element required for plant growth, and concentrations are particularly high in rapid growth biomass such as grasses or related energy crops. During combustion or gasification, alkali salts in the biomass vaporize to form products such as KOH and KCl , which in turn react with chlorine and sulfur. Although most biomass feedstock have naturally low levels of sulfur, even the naturally occurring concentrations can

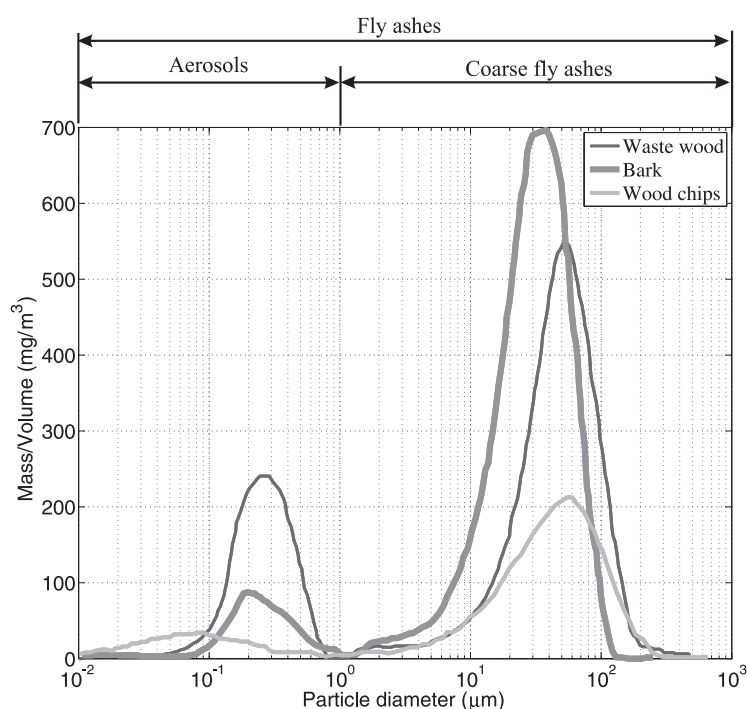


Figure A.1: Typical bimodal particle size distribution observed in biomass combustion [42].

lead to alkali vapor formation. The high alkali content of some biomass feedstock can create significant gas cleanup challenges. Sodium and potassium salts in the ash material can vaporize even at moderate temperatures of about 650 – 700 °C . Unlike the solid particulates that can be separated by physical means such as barrier filters, the vaporized alkali compounds will remain in the product gas at high temperature. As a result, the alkali vapors cannot readily be removed from the hot gas stream by simple filtration. Condensation of the vaporized alkali typically begins at low temperature on particles in the gas stream, with subsequent deposition on cooler surfaces in the system such as heat exchangers, turbine expansion blades, or similar areas. Vaporized alkali salts can readily pass from the combustor through clean-up systems such as cyclones, and finally deposit on cooler down-stream components. Cooling the gas will result in condensation of the vapors into fine solids.

- Tars: 'Tar' is a generic term describing a complex range of oxygenated organic constituents that are produced by the partial reaction of the biomass feedstock. Such materials reside in the hot gas stream as vaporized materials or as persistent aerosols, but typically condense at cooler temperatures. These tars include a variety of oxygenated aromatics formed in the pyrolysis step of the gasifi-

cation process. The composition of tar is complex and highly dependent on the reaction conditions encountered, including gasification temperature and residence time in the reactor. The mechanisms of tar formation have been reviewed in detail by Evans and Milne [27]. As biomass is heated, it dehydrates and then volatilizes while it thermally decomposes. The volatilized material can either undergo further decomposition to form permanent gases, or it can undergo dehydration, condensation, and polymerization reactions that result in tar formation. In most applications, tars in the raw product gases, even at low concentrations, can create major handling and disposal problems. Tars readily condense on cool components downstream from the gasifier, resulting in plugging and fouling of pipes, tubes, and other equipment. In temperature regions above about 400 °C, the tars can undergo subsequent dehydration reactions to form solid char and coke that further plugs the system. The tars represent a cleanup problem and may be classified as hazardous wastes for disposal purposes.

- Nitrogen containing contaminants: The primary nitrogen-containing contaminant in the raw gas from biomass gasifiers is ammonia (NH_3). Ammonia is formed from proteins and other nitrogen-containing components in the biomass.
- Sulphur: Sulphur in the biomass feedstock can be converted to hydrogen sulfide or sulfur oxides during gasification, depending on the gasification approach. Most biomass feedstock contains low percentages of sulfur and is often not a major concern.

Although the contaminant formation mechanism varies from that of biomass gasification, the gas phase contaminants in coal fired, co-fired boilers and waste incinerators are comparable. In the following discussions, a generalized approach to describe fouling is adopted unless stated otherwise.

Cyclone design and pressure drop in the system

The experimental setup involves several equipments and the parts needs to be designed in a optimized way. The experiment is intended to be carried out for different flow rates and at different temperatures. Under these conditions of a closed loop flow in a duct with different parts, it is learnt that the pressure drop across the whole system is a vital design parameter. Further, since the blower is the equipment that keeps the momentum of the flow going on, it becomes necessary to operate the blower under a higher static pressure head than the sum of pressure drops across various regions. The following section covers the basic design factors for a cyclone and the pressure drop across each equipment.

B.1 Cyclone and its design

Cyclones are a class of separating devices in which the inlet gas is brought tangentially into a cylindrical section and a strong vortex is created inside the cyclone body. Particles in the flow are subjected to centrifugal forces which move them radially outwards, towards the inside cyclone surface on which the particles separate. In a typical reverse flow cyclone, the gas inlet maybe tangential, spiral, helical, or axial. The outer vortex created by the tangential entry is helical, moving downwards - particles in the flow settle in to a dust layer on the wall and this is pushed down in to

the apex. Hence the removal of the dust from the collection surface is due to the gas flow and not due to gravity which has a minor role on efficiency of cyclones. The outer vortex reverses its axial direction in the apex and creates the inner vortex going upwards, which carries the gas into the outlet pipe. The tangential velocity is the largest component of the gas velocity in the cyclone and this leads to large centrifugal forces on the particles in the flow. The main flow in a cyclone is axial, downward on the larger radii and upward near the center. There is also a small radially inward velocity which transfers some of the gas from the outer vortex into the inner vortex, throughout the length of the cyclone.

Like all other flow devices, a cyclone offers resistance to flow and this is a function of flow rate Q . The resistance to flow is expressed as static pressure drop ΔP . The most reliable way of establishing the pressure drop and flow rate relationship is by tests; in the absence of any test data and if the cyclone under consideration is not standard, then one of the available empirical correlations proposed by various authors may be used. The following section gives a comprehensive method to determine the pressure drop [13].

symbols:

a	entrance height	
b	entrance width	
r_{cyl}	cylinder radius	
r_{vortex}	vortex finder radius	
r_{out}	outlet radius	
D_{cyl}	cylinder diameter	
D_{vortex}	vortex finder diameter	
D_{out}	outlet diameter	
h_{tot}	total height	
h_{cyl}	cylinder height	
h_{vortex}	vortex finder height	
h_{sep}	separation height under vortex finder	
A_{in}	inlet area	
A_{out}	outlet area	
ϕ_v	volumetric flow rate	
Inlet area		$A_{in} = ab$
Outlet area		$A_{out} = \pi(r_{vortex})^2$
Separation height		$h_{sep} = h_{tot} - h_{vortex}$

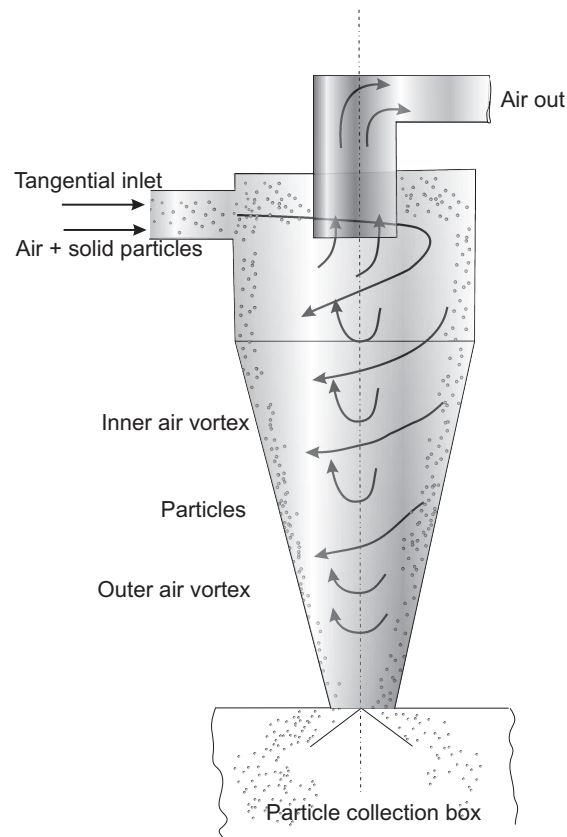


Figure B.1: Schematic representation of a particle cyclone separator.

Entrance velocity:

$$V_{in} = \frac{\phi_v}{A_{out}}$$

Separation height under vortex finder

$$h_{sep} = h_{tot} - h_{vortex}$$

Entrance velocity

$$v_{in} = \frac{\phi_v}{A_{in}}$$

Axial velocity at outlet:

$$v_{a.vortex} = \frac{\phi_v}{A_{out}}$$

Total cyclone surface area:

$$A_{cyl} + A_{vortex} + A_{cone} + A_{plate} - A_{in}$$

where

$$A_{cyl} = 2\pi r_{cyl} h_{cyl}$$

$$A_{vortex} = (2\pi r_{vortex} h_{vortex})$$

$$A_{plate} = \pi r_{cyl}^2 - \pi r_{vortex}^2$$

$$A_{cone} = \pi(r_{cyl} + r_{out})\sqrt{(h_{tot} - h_{cyl})^2 + (r_{cyl} - r_{out})^2} - \pi(r_{cyl}^2 + r_{out}^2)$$

$$\text{Frictionless tangential velocity at wall} \quad V_{t.cyl} = \frac{v_{in}}{0.889 - 0.204 \frac{b}{r_{cyl}}} \quad (B.1)$$

$$\text{Wall friction factor} \quad \lambda_o = 0.005 + \frac{287.4}{Re_w} \quad (B.2)$$

$$\text{where} \quad Re_w = \frac{v_{t.cyl} * 2 * r_{cyl} * \rho g}{\mu} \quad (B.3)$$

Tangential velocity on the vortex outlet region

Constants to calculate the influence of inlet region:

$$\alpha = 1 - \left[0.54 - \frac{0.153}{\frac{A_{in}}{A_{out}}} \right] \left(\frac{b}{r_{cyl}} \right)^{\frac{1}{3}} \quad (B.4)$$

$$r_\alpha = r_{cyl} - \frac{b}{2} \quad (B.5)$$

equivalent friction height:

$$h_{eq} = \frac{A_{tot}}{2\pi\sqrt{r_{cyl}r_{vortex}}} \quad (B.6)$$

Tangential velocity at vortex radius

$$v_{t.vortex} = \left[\frac{1}{\frac{A_{in}}{A_{out}} \frac{\alpha}{r_{vortex}} + \lambda_o \left(\frac{h_{eq}}{r_{vortex}} \right)} \right] v_{a.vortex} \quad (B.7)$$

Pressure drop

Pressure drop coefficients are given by:

$$\zeta_{in} = \frac{r_{vortex}}{r_{cyl}} \left[\frac{1}{\left(1 - \frac{v_{t.vortex}}{v_{a.vortex}} \frac{h_{tot}}{r_{vortex}} \lambda_o \right)^2} - 1 \right] \left(\frac{v_{t.vortex}}{v_{a.vortex}} \right)^2 \quad (B.8)$$

$$\zeta_{out} = \left[2 + 3 \left(\frac{v_{t.vortex}}{v_{a.vortex}} \right)^{\frac{4}{3}} + \left(\frac{v_{t.vortex}}{v_{a.vortex}} \right)^2 \right] * 0.8 \quad (B.9)$$

Inlet pressure drop

$$\Delta P_{in} = \zeta_{in} \frac{\rho_g}{2} (v_{a.vortex}^2) \quad (\text{B.10})$$

Outlet pressure drop:

$$\Delta P_{out} = \zeta_{out} \frac{\rho_g}{2} (v_{a.vortex}^2) \quad (\text{B.11})$$

$$\Delta P_{total} = \Delta P_{in} + \Delta P_{out} \quad (\text{B.12})$$

Collection efficiency according to Clift's improved Dietz model:

$$C(d) = \frac{\pi \rho_p d_p^2 v_{in} h_{sep}}{9 \mu a b} \quad (\text{B.13})$$

$$\eta = 1 - \frac{1}{a + C(d)} \exp\left(-C(d) \frac{h_{vortex} - \frac{a}{2}}{h_{sep}}\right) \quad (\text{B.14})$$

Alexander's natural length: In the optimal design Alexander's natural length coincides with the separation height. If the separation height is larger than Alexander's length, then the cyclone size is large. This results in higher costs and higher pressure drops are generated. If the separation height is too small, some particles will not be separated and will re-entrain into the flow and causes reduced collection efficiency.

$$L_{alex} = 2.3(2r_{vortex}) \left(\frac{(2r_{cyl})^2}{ab}\right)^{\frac{1}{3}} \quad (\text{B.15})$$

The choice of the dimensions is a bit ambiguous in the sense that there are several design ratios proposed. However, one of the widely used is proportions is as follows:

$$D_{cyl} = D$$

$$D_{vortex} = 0.62D$$

$$D_{out} = 0.4D$$

$$e = 0.5D$$

$$a = 0.65D$$

$$H_{cyl} = 1.3D$$

$$H_{vortex} = 0.83D$$

$$H_{cone} = 2D$$

$$H_{tot} = 4.5D$$

$$b = 0.35D$$

B.2 Pressure drop due to different parts of the system

To maintain the flow of air across different sections of the experimental facility, the pressure head that the blower can handle must be larger than the pressure drop (flow resistance) offered by the different parts of the system. The straight channels and the bends along with the heater, cyclone, turbulence grids offers major resistance to the flow. The pressure drop across the cyclone can be evaluated based on the discussion in the previous section. The pressure drop offered by the turbulence grids were obtained from the manufacturer and the resistance to flow due to other factors are covered in the following sections.

B.2.1 Pressure drop for flow through duct

Between two sections considered, the one dimensional continuity equation reduces to $Q_1 = Q_2 = \text{constant}$ or $v_1 = v_2 = V$

The steady flow energy equation gives [67]:

$$\left(\frac{P}{\rho g} + \alpha \frac{V^2}{2g} + z \right)_1 = \left(\frac{P}{\rho g} + \alpha \frac{V^2}{2g} + z \right)_2 + h_f \quad (\text{B.16})$$

where α is the kinetic energy correction factor with a value of 2 for laminar flow and from 1.04 to 1.11 for turbulent flow. h_f is the frictional head loss.

Assuming a fully developed flow between two sections, the velocity profile will be the same and hence, $\alpha_1 = \alpha_2$ and as $V_1 = V_2$, the equation reduces to head loss versus pressure drop and elevation change:

$$h_f = (z_1 - z_2) + \left(\frac{P_1}{\rho g} - \frac{P_2}{\rho g} \right) = \Delta z + \frac{\Delta P}{\rho g} \quad (\text{B.17})$$

The head loss is related to the wall shear stress as:

$$h_f = \Delta z + \frac{\Delta P}{\rho g} = \frac{2\tau_w L}{\rho g R} = \frac{4\tau_w L}{\rho g d} \quad (\text{B.18})$$

From Hagen's correlation,

$$h_f = f \frac{L V^2}{d 2g} \quad (\text{B.19})$$

where f is the Darcy's friction factor and the wall shear can be calculated from the log law of turbulent shear flow or approximations can be used to find f as a function of Reynolds number.

B.2.2 Pressure drop for bends

A bend or curve in a duct induces a loss larger than the simple straight pipe Moody friction loss, due to flow separation on the curved walls and a swirling secondary flow arising from the centripetal acceleration. For a turbulent flow with a 90° bend, the loss coefficient is given by [67]:

$$K \approx 0.388 \alpha \frac{R^{0.84}}{d} Re_D^{-0.17} \quad \text{where } \alpha = 0.95 + 4.42 \frac{R^{-1.96}}{d} \quad (\text{B.20})$$

One can calculate the pressure drop using the relation for minor losses of pipes:

$$K = \frac{\Delta P}{\frac{1}{2}\rho V^2} \quad (\text{B.21})$$

B.2.3 Pressure drop across heat exchanger/test section

The designed heat exchanger consists of 9 cylindrical tubes in a cross flow and accounts for a corresponding pressure drop across the tube bundle. The pressure drop can be calculated as a function of number of tube rows, tube pitch in streamwise crosswise direction, tube arrangement and flow velocity [12].

The pressure drop experienced by the cross flow is proportional to the number of tube rows counted in the flow direction is given by:

$$\Delta P = nf\chi\frac{1}{2}\rho V^2 \quad (\text{B.22})$$

The dimensionless factors f and χ are given as charts which uses values of longitudinal and transverse pitch.

B.2.4 Pressure drop across heater

The heater is in simple terms again cylinder tube bundle in cross flow. However, the physics involved here is much more complex due to heat transfer mechanisms. Since the heater will be procured from an external company to meet the special requirements, the pressure drop data for different flow conditions have been acquired from the manufacturer and is shown in figure B.2.

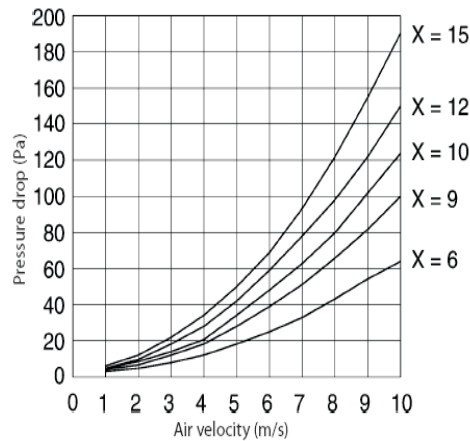


Figure B.2: Variation of pressure drop with velocity in heater, X =number of heating tubes

Summary

Particulate Fouling of Dry and Liquid Coated Surfaces

Particulate fouling is the process of deposition of extraneous particulate matter on other surfaces. In particular, particulate fouling is a major cause of concern in energy-intensive heat recovery systems like biomass gasifiers, coal fired boiler and waste incinerators. The thermal energy is extracted from the flue gas using a system of heat exchangers. The flue gas is however contaminated with particulate matter, tar, nitrogen, sulphur and alkali compounds. The contaminants are transported by the flue gas and interact with the heat exchanger surface eventually forming a deposit layer. The deposit layers have very low thermal conductivity and leads to drastic loss in thermal efficiency apart from maintenance problems and capital losses. The focus of this research is to understand the process of particulate fouling from a fundamental view point based on particle surface interactions and the global effects associated with process conditions by experiments. A numerical model to capture the deposition and removal of particles over heat exchanger surfaces is aimed at.

Particles which arrive at the heat exchanger surface and undergo inertial impaction can stick to the surface, rebound and might remove other previously deposited particles. In order to model the process, a sticking criterion is necessary. The interaction of a particle with other particles on the heat exchanger surface can be either in a dry state or in the presence of a thin liquid film due to condensation of alkali compounds. Detailed experiments were performed to evaluate the sticking criterion for particle impaction over a liquid coated surface under elastic and elastic-plastic deformation conditions. An empirical relation in terms of Stokes number was evaluated to determine the energy loss in the thin interstitial liquid film. A critical Stokes number range between 2 and 5 was observed below which particles do not rebound from the surface. In the Stokes number range of 5 to 20, the particles were observed to rebound but do not overcome the viscous effects of the liquid layer.

A high-temperature closed-loop vertical wind tunnel was designed and constructed to perform fouling experiments under controlled conditions. The effect of gas velocity, particle concentration, particle size distribution, gas temperature, heat exchanger tube orientation and geometry was studied. A measurement technique

that allowed the evaluation of temporal evolution of the fouling layer thickness was used. The experimental investigations revealed that the shear induced by the gas flowing around the tube has a major effect on the overall deposit growth dynamics. The geometry and orientation of the tube indicated that deposition and removal of particles is strongly coupled to the flow dynamics and particle surface interactions.

A numerical model was implemented in a commercial software package to capture the deposition and removal of particles. The deposition model was based on particle-surface interactions including elastic-plastic deformations and the removal model was based on the rolling moment induced by the flow and on the energy transferred by other impacting particles. The fundamental impaction experiments along with the controlled experiments have provided better insight into the process of particulate fouling and resulted in the development of a numerical model which can be used to devise mitigation strategies for particulate fouling.

Samenvatting

Het ongewenst neerslaan van deeltjes op een warmtewisselend oppervlak, oftewel particulate fouling, vermindert de prestaties van energieconversie systemen zoals bijvoorbeeld biomassavergassers, kolengestookte boilers en afvalverbrandingsinstallaties. In deze installaties wordt de thermische energie aan de rookgassen onttrokken door een warmtewisselaar. De rookgassen bevatten echter deeltjes die bestaan uit teer, stikstof-, zwavel- en alkaliverbindingen die kunnen neerslaan en een isolerende laag kunnen vormen. Deze isolerende laag veroorzaakt een verminderd thermisch rendement, en verhoogt de onderhoudskosten.

Het doel van dit onderzoek is tweeledig. Enerzijds wordt door middel van experimenten het effect van procescondities op het ongewenst neerslaan van deeltjes onderzocht. Anderzijds worden de plak- en verwijderingsmechanismen van deeltjes op droge en natte oppervlakken in detail bestudeerd.

Deeltjes die tegen een warmtewisselend oppervlak botsen, kunnen zich hechten aan het oppervlak, kunnen terugkaatsen of kunnen eerder gedeponeerde deeltjes verwijderen. Om dit proces te modelleren is een hecht criterium gedefinieerd. De interactie van een deeltje met andere deeltjes op het warmtewisselend oppervlak vindt plaats in droge toestand of in de aanwezigheid van een dunne vloeibare film als gevolg van bijvoorbeeld de condensatie van alkali-verbindingen. Gedetailleerde experimenten werden uitgevoerd om het hecht criterium te evalueren voor een met een vloeistof gecoat oppervlak onder elastische en elastisch-plastische vervormingsomstandigheden. Een empirische relatie op basis van het Stokesgetal is opgesteld om het energieverlies te bepalen in de dunne interstitiële vloeistoffilm. Een kritisch Stokesgetal tussen 2 en 5 werd waargenomen waaronder deeltjes niet terugstuiten van het oppervlak. Voor Stokes getallen van 5 tot 20 werd waargenomen dat de deeltjes in eerste instantie terugstuiten, maar niet de viskeuze effecten van de vloeistoflaag kunnen overwinnen.

Een hoge temperatuur closed loop verticale windtunnel is ontworpen en gebouwd om vervuilingsexperimenten uit te voeren onder gecontroleerde omstandigheden. Het effect van gassnelheid, deeltjesconcentratie, deeltjesgrootteverdeling, gastemperatuur, warmtewisselaar oriëntatie en geometrie is bestudeerd. Hierbij werd een

meetmethode toegepast waarmee de ontwikkeling in de tijd van de aangroei van de vervuilingslaag gemeten kon worden. Uit de experimenten is gebleken dat de afschuiving veroorzaakt door het rookgas dat rondom de buis stroomt, een grote invloed heeft op de dynamiek van de depositie aangroei. Uit de experimenten met een verschillende geometrie en oriëntatie van de buis bleek dat het neerslaan en verwijderen van deeltjes sterk gekoppeld is aan de stromingsconfiguratie en de interactie van de deeltjes met het oppervlak.

Het neerslaan en verwijderen van deeltjes is in een commercieel softwarepakket gemodelleerd. In het model zijn de relaties voor het neerslaan van deeltjes gebaseerd op deeltjes-oppervlakte interacties en elastisch-plastische vervormingen. De relaties voor het verwijderen van deeltjes zijn gebaseerd op het rolmoment dat veroorzaakt wordt door de kracht van de stroming uitgeoefend op de deeltjes.

Zowel de fundamentele als de gecontroleerde deeltjes depositie experimenten hebben beter inzicht gegeven in het proces van deeltjes vervuiling. De resultaten zijn geïmplementeerd in een numeriek model dat gebruikt kan worden om strategieën te ontwikkelen om de nadelige effecten van depositie van deeltjes te verminderen.

Curriculum Vitae

Kiran Kumar Sathyanarayanarao Subbarao was born on the 17th of January 1981 in Bengaluru, India. He attended MES Kishora Kendra for secondary school and later joined a three year full term apprenticeship training at MICO-Bosch. During his industrial training as a machinist, he learnt several aspects of a mechanical engineering company and specialized in operating precision machine tools. After his apprenticeship, he completed his pre-university education in science from SYA College. From 2001 to 2005 he studied at S. J. C. Institute of Technology and pursued Bachelor degree in mechanical engineering from Visvesvaraya Technological University and earned a degree with distinction. In 2005 he moved from Bengaluru to Sweden to pursue his Masters degree in Computational and Experimental Turbulence at Chalmers University of Technology, Gothenburg. His master thesis was entitled 'Numerical investigation of fiber sedimentation and compaction' which was funded by Metso paper and was done under the guidance of Prof. Alf-Erik Almstedt. After obtaining his Master degree in 2007, he briefly worked for Mechartes researchers in New Delhi as a CFD engineer. In September 2007, he joined the Energy Technology group at the Eindhoven University of Technology as a PhD researcher. The research was carried out under the supervision of Prof. dr. ir. Anton van Steenhoven and dr. ir. Camilo Rindt. The project was funded by the Dutch Ministry of Economic Affairs, Agriculture and Innovation to study gas side particulate fouling in biomass gasifiers.

Acknowledgements

After this interesting journey of four years, it gives me immense pleasure in thanking everyone who has extended their help, support, and guidance. This would probably be the best opportunity to extend my utmost gratitude to my professor Anton van Steenhoven. I am grateful for his patience, insight and timely suggestions which helped me to understand things more clearly. On the same note, I am greatly indebted to my supervisor, Camilo Rindt. He has been an outstanding supervisor and guide. There were occasions where I felt his confidence in me and that in itself was like a reward. At times, I used to feel low and confused, but after a sitting with Anton and Camilo, I would be rejuvenated and would start off with my work again with full enthusiasm. They have always been very supportive and encouraging; needless to say, their able guidance has helped me reach this point.

The project started off by designing and constructing an experimental facility which was truly an interesting experience. This would have been almost impossible without the help from the workshop experts: Geert-Jan and Henri. A lot of welding, cutting and machining work was involved and Geert-Jan pulled it off perfectly. Henri's precision work helped me to put other things in place and to build another setup for the small scale experiments. They always understood the importance of time and provided me their complete support. I owe my thanks to Henk for helping me in the overall design and construction process of the fouling setup, and also for the Dutch summary. I sincerely appreciate all the other technical staff of Thermo Fluids Engineering lab for their constant support which made my work in the lab seem easy. I am also grateful to Mohammed, Rick de Lange and Erik van Kemenade for their practical inputs during the design phase and Agentschap NL for the funding. Several bachelor and master students have worked with me on this project and I truly acknowledge their support and timely inputs.

Natascha was my first office roommate and I am thankful to her for helping me out in the initial stages and for the nice discussions we used to have at office. Zhipeng followed as my second roommate with whom I had a good time at the office. I would also like to extend my regards to my other past and present colleagues: Arjan, Boris, Daniel, Eldhose, Erik, Esubalew, Ilhan, Joy, Junghan, Kon-

stantin, Lakhdar, Linda, Petra, Pieter, Rudi and Silvia in the Energy Technology group for the wonderful time we had. I will surely miss all the coffee break discussions and our famous ET events. I hope the tradition continues! Eldhose helped me to quickly understand and write the Fluent user defined functions which saved me precious time and I would like to thank him for his time and support.

I would like to extend my gratitude to all my friends in making my stay in Eindhoven a very pleasant one, especially Srinidhi and Ujwal for the wonderful time we spent together. I had a splendid time with Sridhar, Mayuri, Rahul, Mannu and Nidhi. Thank you guys!

Finally, this acknowledgement would be complete, only if I thank my family. I feel very lucky to have such a loving and supportive family. Be it my digress from the conventional educational route, or my crazy adventures, the trust and support of my parents never wavered in me. They have strived hard to provide me with everything I ever needed and good education, for which I am short of words to thank them. Savitha, my sister, has helped me a lot in all my endeavors and I will always be indebted to her for her love and support. I would also like to thank my brother Sudhakar, for being very supportive and constantly encouraging me to do well in my education. I would like to thank Shyam, Roopa, Subhash and Suhas for their love and affection.

A translation of an ancient Sanskrit quote reads:

"Contentment is the highest gain, good company is priceless, enquiry leads to wisdom, and peace is the highest enjoyment"

I am glad to have come across people who have helped me to live mostly according to the above statement.